Multiwavelength Observations of Tanami sources

Masterarbeit aus der Physik
Vorgelegt von

Felicia Krauß

06.03.2013

Dr. Karl Remeis-Sternwarte Bamberg
Friedrich-Alexander-Universität Erlangen-Nürnberg

Betreuer: Prof. Dr. Jörn Wilms
Prof. Dr. Matthias Kadler

The cover picture is an artist's impression of an active galactic nucleus. The material, which is gravitationally drawn to the supermassive black hole at the center of the active galactic nucleus, forms an accretion disk. Jets, which are highly collimated outflows of matter, are produced and ejected perpendicular to the accretion disc.

Contents

Zusammenfassung

In meiner Masterarbeit stelle ich die Analyse der Multiwellenlängenbeobachtungen von Blazaren vor. Blazare sind eine Unterklasse der radiolauten aktiven Galaxien (active galactic nucleus; AGN). Aktive Galaxien gehören zu den leuchtkräftigsten Objekten im Universum. Sie emittieren Strahlung in den meisten Bereichen des elektromagnetischen Spektrums, von Radioemission bis hin zur hochenergetischen Gammastrahlung. Radiolaute AGNs weisen einen kollimierten Materieausfluss auf, den Jet. Diese sind meist in allen Wellenlängen sichtbar und bis heute nicht genau verstanden. Das vereinheitlichte Modell für AGN sagt aus, dass wir vermeintlich verschiedene Quellen sehen, je nachdem aus welchem Blickwinkel wir ein AGN beobachten. Blazare sind radiolaute AGN bei denen der Winkel zwischen der Sichtline und dem Jet sehr gering ist, deshalb können in diesen Quellen die Emissionsmechanismen der Jets untersucht werden.

Das TANAMI (*Tracking Active Galactic Nuclei with Austral Milliarcsecond Interferometry*) Projekt beobachtet ein Sample aus 84 radiolauten AGNs. Jede dieser Quellen wird alle 3-4 Monate mit Radioteleskopen beobachtet. Dazu wird ein Array aus Teleskopen auf der Südhalbkugel verwendet. Von vielen dieser Quellen ist nur sehr wenig bekannt, da sich die meisten Radioteleskope auf der Nordhalbkugeln befinden. In meiner Arbeit verwende ich die Quellliste des TANAMI Projektes. Um Spektren dieses Samples in verschiedenen Wellenlängenbereichen zu analysieren, wurden Daten verwendet, die simultan oder nahezu simulaten aufgenommen wurden. Zusätzlich zu den Radiodaten des TANAMI Array werden Daten des *Swift* Satelliten verwendet, der im optischen, ultravioleten und im Röntgenbereich misst. Die Röntgenanalyse wird detailiert vorgestellt, da sie verwendet wird um die Absorption im Röntgenbereich und die Extinktion bei optischen Wellenlängen zu bestimmen. Da diese sehr genau bestimmt werden müssen sind die Anforderungen an die Qualität der Röntgendaten hoch.

Der *Fermi* Satellit, der 2008 gestartet wurde, scannt kontinuierlich den Himmel im Gammabereich ab. Folglich können Lichtkurven und zeitaufgelöste Spektren extrahiert werden. Bei Blazaren stellt man fest, dass sie starke Flussvariabilität aufweisen. Deshalb ist es notwendig bei der Erstellung von Breitbandspektren (spectral energy distriution; SED) darauf zu achten, dass in der Zeitspanne in der die Beobachtungen aufgenommen wurden der Quellfluss kaum variiert hat. Dabei reduzierten die Anforderung an die Datenqualität und die Gleichtzeitigkeit die Anzahl der Quellen, die verwendet werden konnten auf sieben.

Die SEDs von Blazaren zeigen eine doppelhöckrige Struktur. Der erste Peak bei niedrigeren Energien lässt sich durch Synchrotronemission erklären. Der Ursprung des zweiten Peaks ist noch nicht geklärt. Mit einfachen Modellen, wie logarithmischen Parabeln, ist es möglich das Spektrum zu beschreiben. Dies funktioniert gut für den Synchrotronpeak, aber der zweite Peak lässt sich in einigen Quellen nur schlecht beschreiben. Dies liegt vor allem an den fehlenden Daten im Gammabereich. Mit den Modellen des Synchrotronpeaks lassen sich weitere Analysen durchführen. Die Blazar-Sequenz gibt eine Korrelation zwischen der Leuchtkraft des Synchrotronpeaks und dessen Frequenz an. Der Synchrotronpeak ist gut durch die *Swift* Daten und die Daten im Radiobereich abgedeckt, dadurch lässt sich die Peakfrequenz und die entsprechende Leuchtkraft zuverlässig bestimmen und die Blazar-Sequenz untersuchen. Obwohl dies nur für wenige Quellen untersucht werden konnte, sprechen die Ergebnisse eher für einen sogenannten Blazar Envelope. Anhand der Leuchtkraftinformation lassen sich weitere Korrelationen untersuchen.

Bei verschiedenen Arten von Quellen, wie beispielsweise galaktische schwarze Löcher, wird eine Korrelation zwischen der Radio- und der Röntgenleuchtkraft beobachtet. Trägt man diese für aktive Galaxien gegeneinander auf, erkennt man ebenfalls einen Zusammenhang. Auch bei den Quellen des TANAMI Samples lässt sich dies beobachten. Diese Ergebnisse geben genaueren Aufschluss über Jets in aktiven Galaxien und ihr Emissionsmechanismen.

Abstract

In this master thesis I present my analysis of multiwavelength observations of blazars. Blazars are a subclass of active galactic nuclei (AGN), which are among the most luminous sources in our universe. They emit radiation across the electromagnetic spectrum from radio frequencies up to γ-ray energies. Radio-loud AGN usually feature a collimated outflow of matter, the jet. These are usually visible in all wavelengths and are not fully understood yet. The unified model of AGN states that we observe different phenomena depending on the angle at which we observe an AGN. Blazars are radio-loud AGN, where the angle between the line of sight and the jet axis is small. We can therefore study jet emission mechanisms using these sources.

The TANAMI (*Tracking Active Galactic Nuclei with Austral Milliarcsecond Interferometry*) project is monitoring a sample of 84 radio-loud AGN. Each of the sources is observed every 3-4 months at radio frequencies with VLBI techniques. The telescopes used are located on the Southern Hemisphere. For many of the sources only very few information is available, because most radio telescopes are on the Northern Hemisphere. In my work I use the TANAMI source sample, analyzing simultaneous or quasi-simultaneous data to study radio-loud AGN. For this purpose I used data by the *Swift* and the *Fermi* satellites, in addition to the radio data of the TANAMI array. *Swift* observes in the optical, ultraviolet and X-ray regime. The analysis of X-ray data will be presented in detail, as they were used to determine the photoelectric absorption and the extinction at optical wavelengths. They have to be measured very accurately, thus the requirements to the quality of the X-ray data were high.

The *Fermi* satellite, which was launched in 2008, is monitoring the whole sky at γ-ray energies. This allows the study of long-term light curves and time-resolved spectra. Blazars show strong variability in flux. For the construction of broadband spectra it is therefore necessary to obtain observations where the flux of the sources varied little or not at all. The simultaneity and the high quality of the data limited the number of sources that could be used to seven.

SEDs of blazars generally show two humps. The peak at lower energies can be explained by synchrotron emission. The origin of the second peak at higher energies has not been found yet, but it is usually attributed to inverse Compton emission. Simple models, such as logarithmic parabolas can describe the observed spectra. This works very well for the synchrotron peak in my sample, but the second peak cannot be described very well for some of the sources, primarily due to the lack of high energy data. Using the results of the synchrotron peak models allows to test the blazar sequence. It states the existence of an anti-correlation between the synchrotron peak luminosity and its frequency. The synchrotron peak is described well due to the data coverage of the TANAMI and *Swift* data. Although only a small number of sources contributes to the results, they indicate that a blazar envelope matches the data better than the blazar sequence.

Furthermore, the correlation between radio and X-ray luminosity is addressed. A correlation between the radio and X-ray luminosity is observed in various type of sources, such as Galactic black holes. It has been found that this correlation is also true for AGN. This is also observed for the TANAMI sources, which have been analyzed. These results of a sample of sources will help to better understand jets and the underlying emission mechanisms.

1. Active Galactic Nuclei

Active galactic nuclei (AGN) are among the most fascinating astronomical objects. They are located at the very center of a galaxy and allegedly harbor supermassive black holes. Their high luminosities (up to 10^4 times those of a galaxy) originate from tiny volumes within the very few central parsecs (Krolik, 1999). These high luminosities allow astronomers to probe the early universe, up to redshifts of $z = 10$. In addition, AGN usually emit across the whole electromagnetic spectrum and show strong variability in all wavebands. Active galaxies have been studied for over 100 years, however, many questions about their evolution and emission mechanisms remain to be answered. In this Chapter I give a brief description of the history and the major properties of AGN following Kembhavi & Narlika (1999), Krolik (1999), Wilms & Kadler (2010) and Bradt (2004).

1.1. History

In 1909 Edward A. Fath was the first to remark on the properties of AGN in optical spectra. He found the emission lines in NGC 1068 to be similar to those found in planetary nebulae (Fath, 1909). A decade later Heber D. Curtis discovered an optical jet in M87. *"M87 exhibits a curious straight ray...apparently connected with the nucleus by a thin line of matter"* (Curtis, 1918, Fig. 1.1). This was the first time where an optical jet, connected to a galaxy, was observed. Many years later, these were found to be visible in several wavebands (Fig. 1.2).
In 1943 Carl Seyfert identified a class of spiral galaxies with optical emission lines (Seyfert, 1943). This type of galaxy is a subclass of active galaxies and was later named after Seyfert.
In 1954 Walter Baade and Rudolph Minkowski discovered the optical counterparts to the radio sources Cygnus A, Virgo A, and Puppis A (Baade & Minkowski, 1954). The X-ray image of Cygnus A shows hot gas in a cavity, which illustrates how AGN and their jets influence their environment.

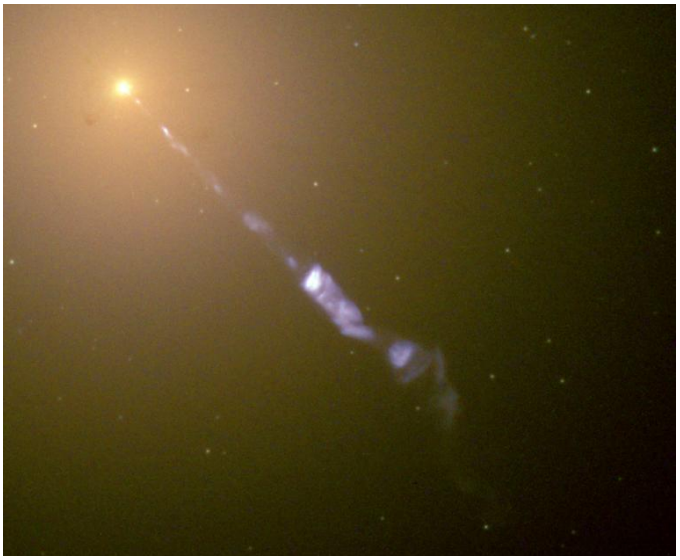

Figure 1.1.: M87 in the optical (NASA and The Hubble Heritage Team (STScI/AURA)).

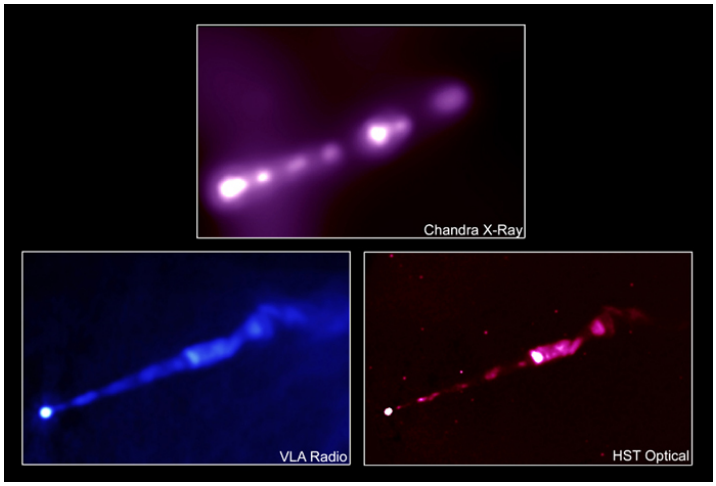

Figure 1.2.: M87 at radio frequencies (VLA), X-rays (Chandra) and in optical (HST); (X-ray: H. Marshall (MIT), et al., CXC, NASA; Radio: F. Zhou, F. Owen (NRAO), J. Biretta (STScI); Optical: E. Perlman (UMBC), et al., STScI, NASA).

Only a few year later Lodewijk Woltjer estimated the mass of the nucleus of an active galaxy. He assumed a size of 100 parsecs and combined this with the width of the emission lines. The resulting masses for the nucleus of the Milky Way, as well as other galaxies, was found to be of the order of $10^8\,M_\odot$ (Woltjer, 1959). In the 1960s radio surveys discovered many unknown sources. The most important surveys were the Cambridge (Edge et al., 1959, Bennett, 1962) and the Parkes surveys (Bolton et al., 1964, Price & Milne, 1965). One of the radio sources that is listed in the third revised Cambridge catalog is 3C 273. Cyril Hazard determined its position more accurately in 1963 by using the method of lunar occultation (Hazard et al., 1963). This position was accurate enough to find an optical counterpart, which appeared star-like. The optical spectrum, taken by Maarten Schmidt, was unusual (Schmidt, 1963). He identified the emission lines and found the corresponding redshift to be $z = 0.158$. Instead of being a peculiar star in our Galaxy, 3C273 was thus discovered to be extragalactic. In 1963 a new name was given to AGN that are bright at radio wavelengths: Quasars or Quasi-Stellar Objects (QSO). In the same year Fred Hoyle and Willy Fowler proposed gravity as the origin of the energy of the source. They assumed the existence of a very massive object, which would lead to a gravitational collapse (Hoyle & Fowler, 1963). In the 1980s it became clear that quasars are usually bright in the X-rays but not all are visible in the radio (Zamorani et al., 1981). The galaxy M87 (see Fig. 1.1) was studied in detail in the late 1970s, when the first charge coupled devices (see Sect. 3.2.3) were used instead of photographic plates. The increase in angular resolution was sufficient to observe a rise in luminosity towards the center of the galaxy. The measured velocity dispersion was also found to increase towards the center. These information led to an estimate of a central attractor with a mass of $\sim 5 \times 10^9\,M_\odot$ (Young et al., 1978). These studies showed that the central attractor could only be a supermassive black hole.

"There is thus a similarity between the nucleus of M87 and a quasar-like 3C 273, in that both are seats of intense energy production, both require a collapsed massive object, both are X-ray sources and, in this particular case both have jets issuing from the central region. As has become clearer over the years, there is a whole class of galactic nuclei of this kind that show signs of energetic activity. These are collectively referred to as active galactic nuclei (AGN)."(Kembhavi & Narlika, 1999)

1.2. The Unified Model

The idea of a unification model arose when it was realized that projection effects have to be important for several types of sources. Scheuer & Readhead (1979)'s study of quasars was the first attempt at a unification of radio-quiet and radio-loud quasars. Only a few years later polarization studies of Seyfert galaxies showed many similarities in broad emission leading to the belief that they are the same objects as quasars, but seen from different angles (Antonucci & Miller, 1985).
Peter Barthel was one of the first to suggest a unification of radio galaxies and quasars (Barthel, 1989a,b). Antonucci (1984) discovered 3C 234, a radio galaxy, whose polarization, which closely resembles a quasar, also features broad Balmer lines. Similar to Seyfert galaxies, broad lines are found in the polarized spectra of radio galaxies and quasars. These lines however, are not found in the total spectrum. This result suggests the presence of toroidal obscuration and thus reflection of polarized light. Several years later the progress on unification models was summarized and discussed by Urry & Padovani (1995). Figure 1.3 shows the unification scheme for AGN. The upper half of the figure shows the unification model for radio-loud AGN and the lower half for radio-quiet AGN. The central supermassive black hole and the accretion disk (see Sect. 2.1) are surrounded by a torus that obscures the

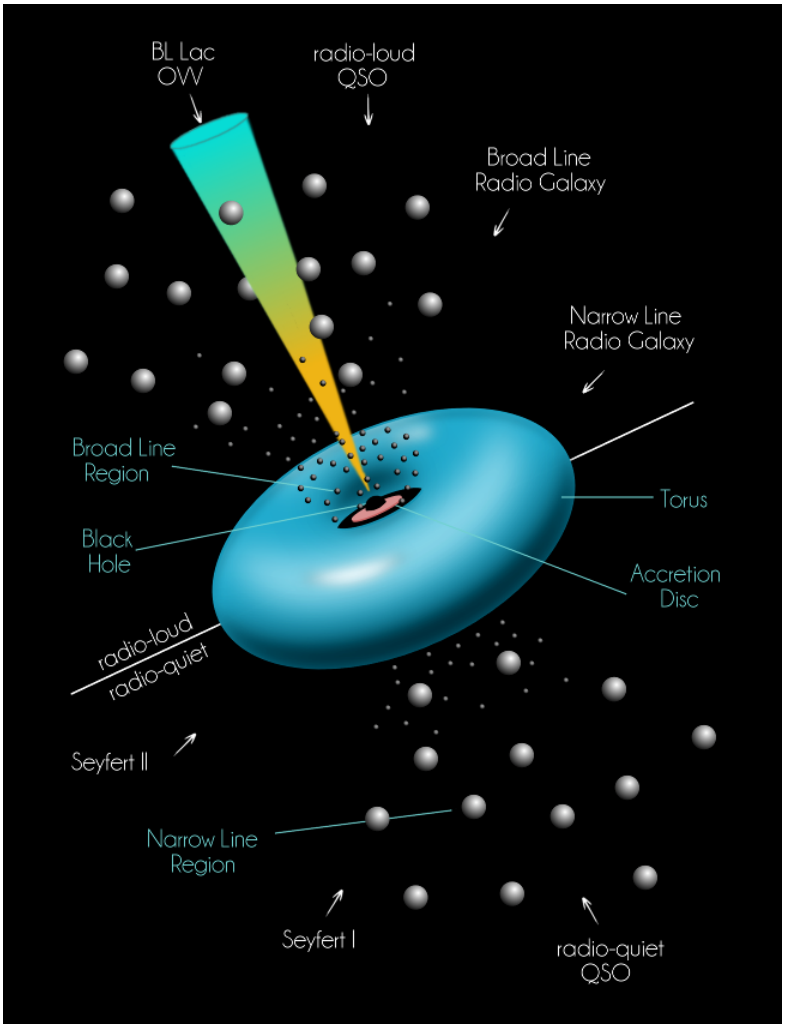

Figure 1.3.: Unified Model of AGN, the arrows represent the viewing angle and the corresponding subclass of AGN, blue labels show the individual components.

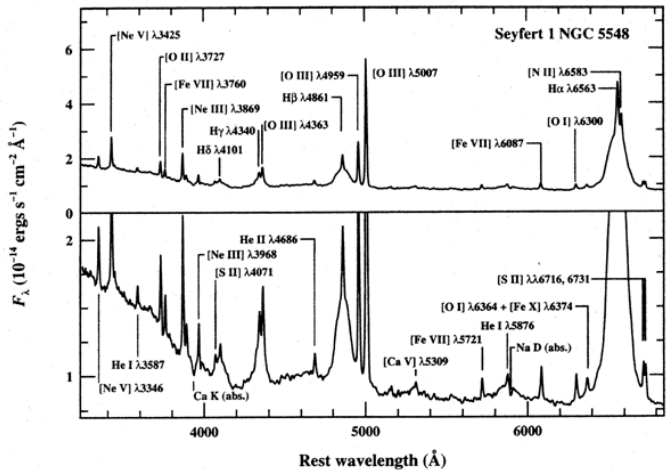

Figure 1.4.: Optical Spectrum of Seyfert I NGC 5548 showing broad and narrow emission lines (Peterson, 1997).

broad line emission. If the absorber was a cloud along the line of sight, line emission would be reflected in all directions, averaging the polarization to zero (Bianchi et al., 2012, and references therein). The difference between radio-loud and radio-quiet AGN is the strength of radio emission, compared to the X-ray emission and the presence of a jet. Radio-loud AGN possess two jets, the jet and the counter-jet, which is not depicted in Fig. 1.3. Radio-loud AGN are discussed in Sect. 1.3.

Table 1.1.: Summary of unification scheme

inclination angle ↓	radio-quiet	radio-loud
Type I	Seyfert I radio-quiet quasar(QSO)	BLRG, BL Lac, OVV radio-loud quasar (FSRQ)
Type II	Seyfert II	NLRG (FR I & II)

Active galaxies and their subclasses can be separated into two groups, type I and type II (see Table 1.1) according to their of optical spectra. Type I AGN have broad and narrow emission lines in their optical spectra, whereas type II only exhibit narrow emission lines. This is represented in the unification scheme through the Broad and Narrow Line Regions. Broad emission lines, which originate in the Broad Line region, are from allowed transitions and can have widths of up to 10^4 km s^{-1}. This suggest the presence of a dense (particle density $n \sim 10^9$ cm^{-3}) medium with high velocities. The narrow emission lines are due to forbidden transitions. Forbidden transitions are only possible in a low density medium ($n \sim 10^3$ cm^{-3} – 10^6 cm^{-3}). An example of an optical spectrum of a Seyfert I galaxy is shown in Fig. 1.4.

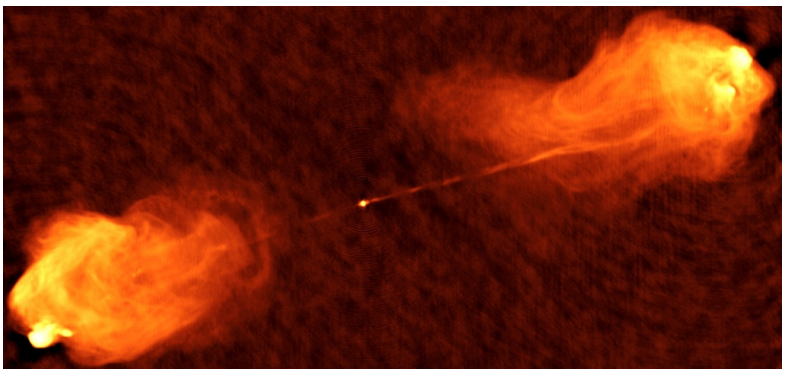

Figure 1.5.: Fanaroff-Riley type II radio galaxy, VLA image of Cygnus A (5 GHz, 0.5″ resolution; Carilli & Barthel, 1996).

1.3. Radio-loud AGN and blazars

Radio galaxies and quasars are usually grouped into two subclasses. Due to the large angle between the jet and the line of sight, the jet structures can be studied in detail. Fanaroff and Riley divided a sample of radio galaxies into two groups, now called Fanaroff-Riley type I and II (Fanaroff, 1974). The brighter objects are in class II. These are characterized by one-sided jets, hot spots, powerful lobes, and very collimated jets. Type I objects show a very bright core, asymmetric jets with wide opening angles, and large plumes (see Figs. 1.5 and 1.6).
Blazars ("blazing quasi-stellar object") are a subclass of radio-loud AGN, where the angle between the line of sight and the jet axis is small. Blazars comprise optically violent variable (OVV) quasars, flat spectrum radio quasars (FSRQ), and BL Lac type objects (Brinkmann et al., 1996, Scarpa & Falomo, 1997).
The word blazar was coined by E. Spiegel as a joke in 1978 at the first conference about BL Lac objects. The name stuck, as it is a combination of the words "BL Lac" and "quasar" and emphasizes the "blazing" characteristics of AGN.

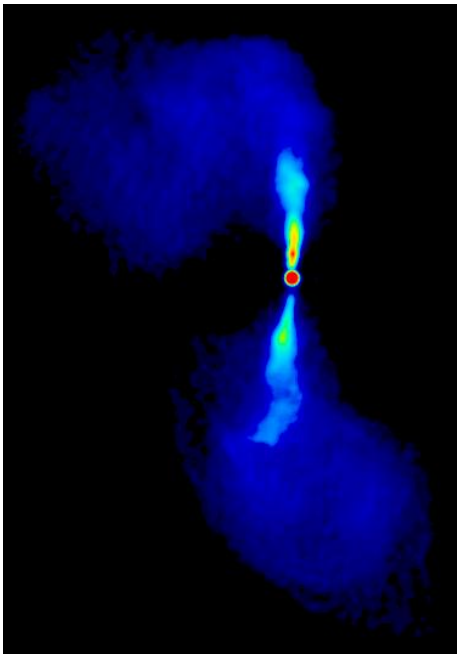

Figure 1.6.: Fanaroff-Riley type I radio galaxy, VLA image of M84 (5 GHz; Laing & Bridle, 1987, http://www.jb.man.ac.uk/atlas/other/3C272P1.html).

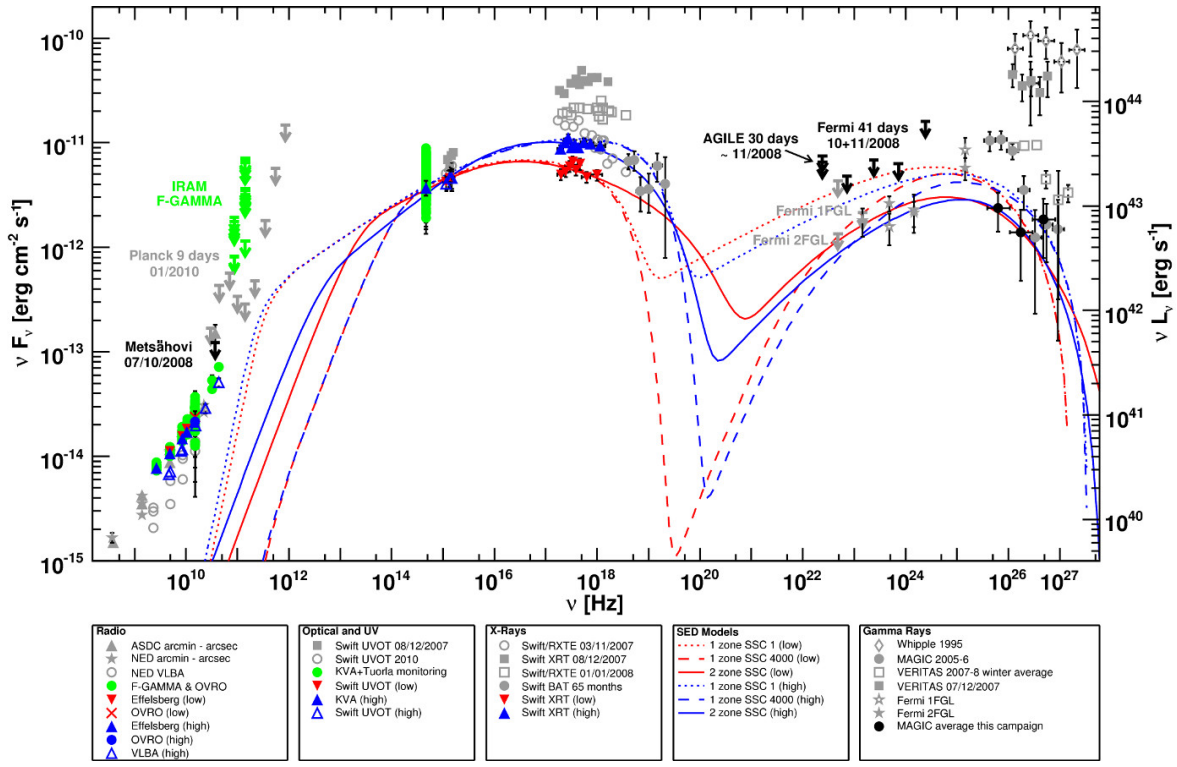

Figure 1.7.: Broadband spectral energy distribution of 1ES 2344+514 in a low state, including archival data (gray) and 1 and 2 zone Synchrotron Self-Compton models (Aleksić et al., 2013a).

Blazars show strong variability on time scales of minutes to years (Ulrich et al., 1997). The first blazar that was discovered was BL Lacertae ("BL Lac", Hoffmeister, 1929), which was later used to classify similar sources as BL Lac type objects. The continuum emission of blazars is non-thermal and thought to be relativistically beamed. Radio observations show apparent superluminal motion in blazars. This is a projection effect due to the small angle of the line of sight to the jet (Cheung et al., 2007, Kellermann et al., 2003). The spectra of blazars are described in detail in Sect. 2.4.

1.4. This thesis

In this thesis I study multiwavelength observations of TANAMI sources. These are radio-loud AGN in the Southern Sky. In Chapter 2 I will first introduce the basic physical processes responsible for emission mechanisms in jets in greater detail, then I will discuss blazars and their broadband spectra. An example of a broadband spectra of a blazar is shown in Fig. 1.7. Chapter 3 will summarize the observational techniques used to study AGN. Data of various satellites, telescopes and instruments were used in this thesis. This is followed by Chapter 4, which is devoted to the results of the analysis. The X-ray data analysis will be presented in detail, as well as the analysis of broadband spectra. In the last Chapter I give a brief summary and an outlook to future work.

2. Theoretical Background

The theoretical description of active galaxies began with the study of black hole physics. Since then, many of the processes in AGN have been described in detail, although they cannot fully explain the observed phenomena yet. In this Chapter I will give a short overview of the process of accretion of matter, as well as the processes of synchrotron radiation and Inverse Compton scattering. In the last part I will discuss broadband spectra and cosmological distances. This Chapter is mainly based on Wilms & Kadler (2010), Kembhavi & Narlika (1999) and Longair (2011).

2.1. Accretion

The generally accepted theory posits that the high luminosity in active galaxies is fueled by a supermassive black hole at the center of the AGN.

"If we put a particle in a circular orbit around a central gravitating body, it will stay in that orbit. If we then extract energy and angular momentum from the particle we may allow it to spiral slowly inwards." (Pringle, 1981)

Conservation of energy and momentum results in the formation of an accretion disk around black holes. Accretion disks were first described concerning star systems, in particular close binary systems (Shakura, 1973). Pringle (1981) describes accretion in astrophysical systems and argues that viscosity is the greatest uncertainty in the theoretical description of accretion disks. Viscosity originates in magnetorotational instabilities (MRI), which increase inhomogeneities in the magnetic field (Balbus & Hawley, 1991, Meier, 2011, Wilms & Kadler, 2010). The upper limit to the accretion process is the Eddington limit.

$$L < L_{\mathrm{Edd}} = \frac{4\pi G M m_{\mathrm{p}} c}{\sigma_T} = 1.3 \cdot 10^{38} \mathrm{erg\ s^{-1}} \frac{M}{M_\odot} \tag{2.1}$$

It is derived by assuming that the gravitational force has to be greater than the radiation pressure to accrete material. The resulting Eq. 2.1 is dependent on the source luminosity, L, the mass of the black hole, M, the proton mass, m_{p}, and the Thomson cross-section, σ_{T}. Accretion can be characterized by its dependency of the efficiency η:

$$L = \eta \cdot \dot{M} c^2 \tag{2.2}$$

with the mass accretion rate $\dot{M}$. Using the Eddington limit, this results in an upper limit of the mass accretion rate.

$$\dot{M}_{\mathrm{max}} = \frac{L_{\mathrm{Edd}}}{\eta \cdot c^2} \tag{2.3}$$

Accretion is approximately 14 times more efficient in producing energy than fusion. An accretion rate of $1 \ldots 2\ M_\odot\ \mathrm{yr}^{-1}$ is sufficient to power a supermassive black hole and explain the observed luminosities (Trump et al., 2011, Lasota et al., 1996).

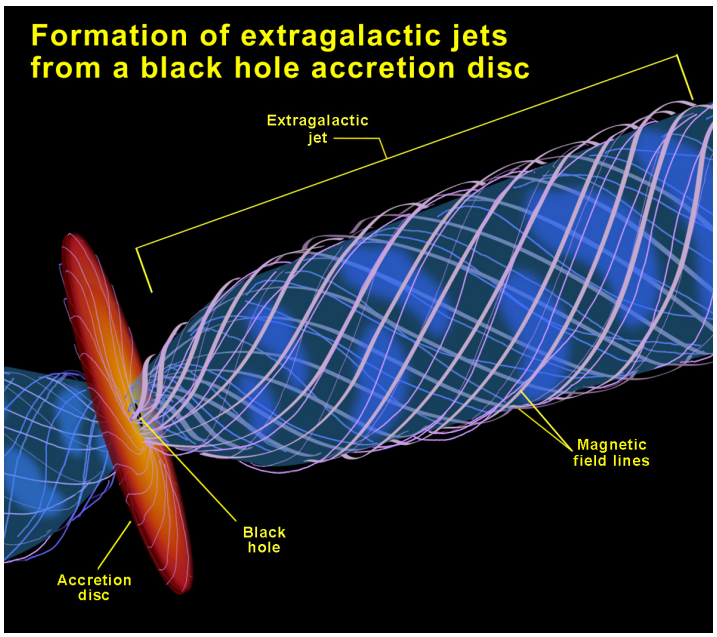

Figure 2.1.: Formation of extragalactic jets (NASA and Ann Feild; Space Telescope Science Institute).

2.2. Jets

After black holes had been established as the central object in active galactic nuclei, jets and their origins were studied in detail. They are observed at various wavelengths from radio up to γ-rays. Penrose (1969) describes the process of extracting energy from black holes by "frame-dragging". This effect occurs near rotating massive objects and distorts the space-time metric. Blandford & Znajek (1977) describe the launching of jets. A black hole with high angular momentum can accelerate charged particles in a magnetic field. Due to the frame-dragging effects these magnetic field lines are twisted helically and particles are accelerated perpendicular to the accretion disk (Fig. 2.1). This results in the formation of a jet and a counter-jet, which are observed in radio-loud AGN. Simulations of the formation and structure of jets have been done by several, including a three-dimensional magnetohydrodynamic simulation by Tchekhovskoy et al. (2011). These simulations show a loss in energy and angular momentum of the black hole. The efficiency of the jet is also dependent on the spin of the black hole. The emission we see from jets are observed in many wavebands. Blandford & Königl (1979) describe the origin of radio emission in relativistic jets. Schwinger (1949) and Alfvén & Herlofson (1950) discuss synchrotron radiation as the origin of radio emission in quasars. High-resolution VLBI methods can be used to resolve jet structures on parsec or sub-parsec scales (Müller et al., 2011). Results often show very fast and highly collimated jets. Radiation processes in jets will be described in the following section.

2.3. Radiation processes

2.3.1. Synchrotron radiation

The low energy peak in spectral energy distributions (see Sect. 2.4) of radio-loud AGN is usually attributed to synchrotron radiation. Thus it is one of the fundamental processes in jets. I will briefly discuss Synchrotron radiation in this section, following Wilms (2012b), Ginzburg & Syrovatskii (1965), Reynolds (1982), Rybicki & Lightman (1979) and Blumenthal & Gould (1970). Synchrotron radiation is produced by relativistic charged particles in a magnetic

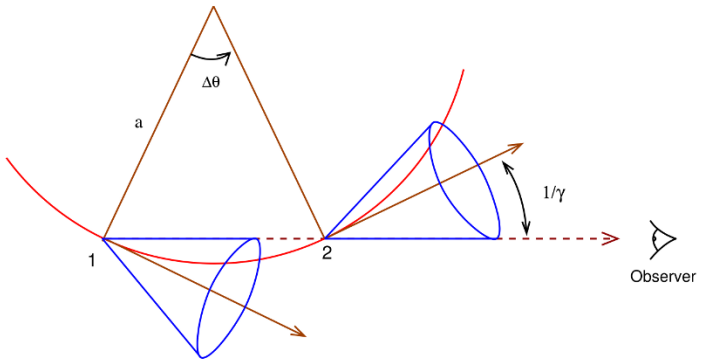

Figure 2.2.: Helical path of an electron emitting synchrotron radiation cones (Rybicki & Lightman, 1979, Wilms, 2012b).

field. In astrophysical processes relativistic electrons are gyrating in a magnetic field. This is a very common process and is not only found in AGN but also in pulsar wind nebulae (Fleishman & Bietenholz, 2007). The continuum in AGN is non-thermal, as it spans many orders of frequency, which cannot be described by thermal models, such as bremsstrahlung or blackbody emission.
The relativistic motion of a particle with charge q and velocity v in a magnetic field B is described by

$$\gamma m\dot{\mathbf{v}} = \frac{q}{c}(\mathbf{v}\times\mathbf{B}) \tag{2.4}$$

and Fig. 2.2 (Wilms & Kadler, 2010). This synchrotron emission has a dipole characteristic in the electron rest frame. The energy loss of the electron can be described by

$$\left(\frac{\mathrm{d}E}{\mathrm{d}t}\right) = -\frac{e^4B^2}{6\pi\epsilon_0 c m_\mathrm{e}^2}\frac{v^2}{c^2}\gamma^2\sin^2\alpha \tag{2.5}$$

The radiative power P of an electron moving in a magnetic field is

$$P = \frac{4}{3}\sigma_\mathrm{T}\, c\beta^2\left(\frac{E}{mc^2}\right)^2\frac{B^2}{8\pi} \tag{2.6}$$

where $\beta = \frac{v}{c}$ and σ_T is the Thomson cross-section. Non-thermal synchrotron radiation is emitted by electrons with energies that follow a power law distribution,

$$n(\lambda)\,\mathrm{d}\lambda = n_0\gamma^{-p}\,\mathrm{d}\lambda. \tag{2.7}$$

The total emitted power is obtained by integrating over the particle distribution n,

$$P_\nu = \int_1^\infty \langle P_\nu(\gamma)\rangle\, n(\gamma)\,\mathrm{d}\gamma. \tag{2.8}$$

It follows that the spectral energy distribution of an electron power law distribution is also a power law

$$P_\nu = \frac{2}{3}c\sigma_T n_0\frac{U_\mathrm{B}}{\nu_\mathrm{L}}\left(\frac{\nu}{\nu_\mathrm{L}}\right)^{-\frac{p-1}{2}}, \tag{2.9}$$

where the spectral index is defined as $\alpha = -(p-1)/2$ (Fig. 2.3).
At low energies synchrotron emission is self-absorbed resulting in a cutoff in the spectrum. Low energy photons emitted by electrons can be reabsorbed by the same electrons. This results in a different proportionality for low frequencies $P_\nu \propto B^{-1/2}\nu^{5/2}$.

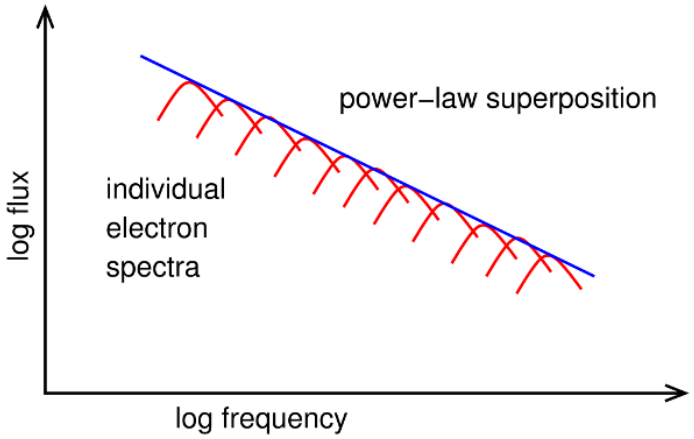

Figure 2.3.: Superposition of individual synchrotron spectra (Shu, 1991, Wilms, 2012b).

2.3.2. High energy emission: Inverse Compton scattering and hadronic models

The origin of the jet emission at high energies in the X-rays and above has not been completely understood yet. In leptonic models this is described by Inverse Compton-scattering, in which seed photons scatter off of relativistic electrons. These electrons are also responsible for producing the synchrotron emission. Seed photons could be the synchrotron photons, which would after being produced up-scatter off of the same electrons which produced them. This process is called Synchrotron Self-Compton (SSC; Ghisellini et al., 1985, Maraschi et al., 1992, Bloom & Marscher, 1993, Ghisellini & Madau, 1996, Celotti et al., 1997, Tavecchio et al., 1998). Generally homogeneous (one-zone) or two-zone SSC models can explain blazar spectra very well (Ghisellini et al., 1998, Finke et al., 2008).
Another possibility for the origin of the seed photons are external photon fields (External Compton; EC), such as photons from the accretion disk or the cosmic microwave background (Dermer et al., 1992, Sikora et al., 1994, Tavecchio et al., 2000).
The jet emission at high energies can also be explained by hadronic or lepto-hadronic models. In these models reactions involve hadron-hadron or photon-hadron collisions, pair production and cascades (Mannheim, 1993a,b). These models are able to explain and model the high energy data better for sources, where the second peak is very broad. Many sources, such as Mrk 421 and Mrk 501 can be modeled very well by SSC models.
However, in some cases both models have difficulties in describing the observed spectra (Sikora et al., 2009).

2.4. Spectral Energy Distributions

2.4.1. Broadband spectra of blazars

Blazars show two broad peaks in their spectral energy distribution (SED). The peak at lower energies can be explained by synchrotron radiation and the peak at higher energies is often attributed to radiation from inverse Compton processes. Alternative explanations are hadronic or lepto-hadronic models. Figure 2.4 shows the spectral energy distribution of 3C 273, one of the best studied quasars. The data in this SED have not been taken simultaneously (Türler et al., 1999). The upper panel shows the flux density spectrum and the lower panel the flux spectrum in the νF_ν representation. The AGN flux density continuum can be described by a power law with a spectral index α (Eq. 2.10).

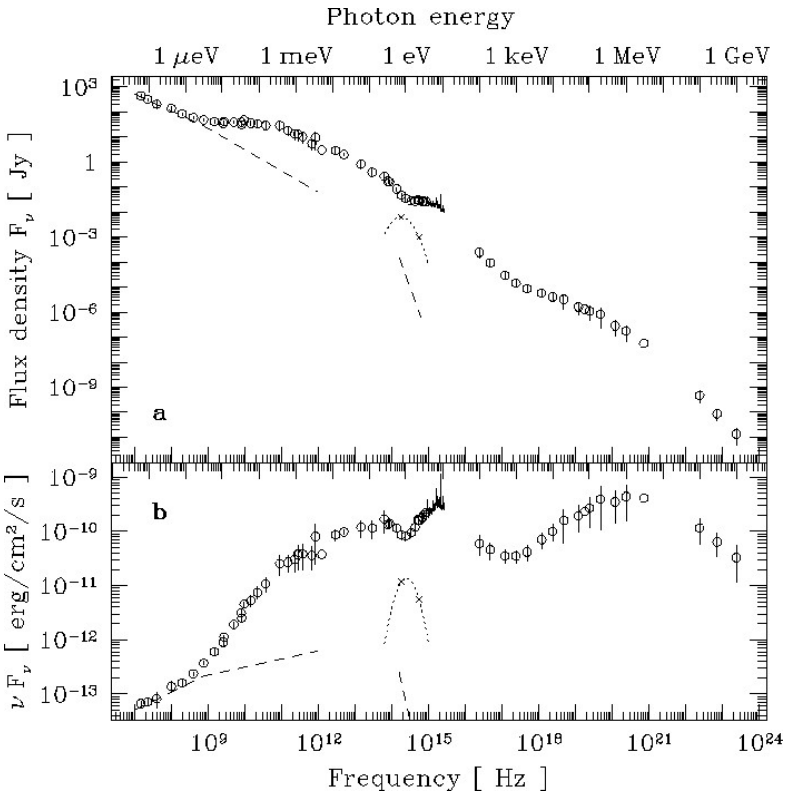

Figure 2.4.: Spectral Energy Distribution of 3C 273, showing the flux density (upper panel) and the flux spectrum (lower panel; Türler et al., 1999).

$$F_\nu = C\nu^{-\alpha} \tag{2.10}$$

The photon index Γ, which is used in X-ray astronomy, can be expressed as a function of the spectral index $\alpha = \Gamma - 1$, with $\alpha \sim 1$. If α is roughly 1, the flux continuum $\nu F_\nu = C \cdot \nu^{-\alpha+1} = C$ is flat. The power, which a blazar emits in a certain waveband, can be described by Eq. 2.11.

$$P = \int_{\nu_1}^{\nu_2} F_\nu \, \mathrm{d}\nu = C \, \ln\left(\frac{\nu_2}{\nu_1}\right) \qquad \text{for } \alpha = 1 \tag{2.11}$$

A flat νF_ν spectrum thus signifies that the same amount of energy is emitted per frequency decade. Only non-thermal emission can explain emission over a broad energy range. Blazars are further classified into two subclasses by their X-ray properties. At X-ray energies the slope in the νF_ν representation is usually either rising or falling and only in very few cases flat. The slope and the corresponding photon indices are described by

$$F_\nu \propto \nu^{-\alpha} = E^{-\alpha} \tag{2.12}$$

with $\alpha = \Gamma - 1$, therefore

$$\nu F_\nu \propto E^{2-\Gamma}. \tag{2.13}$$

Blazars with a rising slope in their X-ray flux spectra are called low-peaked BL Lac objects (LBL), because their synchrotron peak frequency is at low frequencies, usually below $10^{14.5}$ Hz. Blazars with a falling slope are called high-peaked BL Lac objects (HBL), because their synchrotron peak energy is located at higher energies of the order of $10^{16.5}$ Hz or higher.

LBLs and HBLs were originally defined by the ratio of the radio to the X-ray flux density (Eq. 2.14).

$$\alpha_{rx} = \frac{\log\left(\frac{F_{5GHz}}{F_{1keV}}\right)}{7.68} \tag{2.14}$$

LBLs and HBLs were then categorized for α_{rx} being greater or smaller than 0.75, respectively (Padovani & Giommi, 1995). It is believed that the angle between the line of sight and the jet axis is greater for HBLs than for LBLs (Jannuzi et al., 1994, Perlman & Stocke, 1994, Rector et al., 2003).

> *"Compared to LBLs, HBLs are more numerous, their cores are less radio luminous, and they are less optically variable [..]."* (Rector et al., 2003)

2.4.2. The blazar sequence

Figure 2.5 shows averaged blazar spectra of different luminosities. These spectra suggest an anti-correlation between the peak luminosity of the source and the peak energy (Fossati et al., 1998). Sources with a higher luminosity seem to have peak energies at lower values than low luminosity sources. This "blazar sequence" is heavily debated. Some authors find no correlation (Giommi et al., 2012). A possible explanation is that it might be affected by selection effects. Other authors propose enhanced blazar sequence models (Meyer et al., 2011, Maraschi et al., 2008). Giommi et al. (2012) found no evidence for a correlation in their analysis of a large sample and suggest that this correlation is only observed due to the selection of sources that are bright in one waveband (e.g., radio or γ-ray selected samples). Many sources have been found that lie in the lower left corner of the $\nu_{peak} - L_{peak}$ plane, below the expected correlation (Nieppola et al., 2006, Caccianiga & Marchã, 2004). Meyer et al. (2011) analyzed a large sample of blazars and suggest a blazar envelope, where highly aligned blazars are the upper limit of peak luminosity. They suggest that radio galaxies are to be found at lower peak luminosities and frequencies.

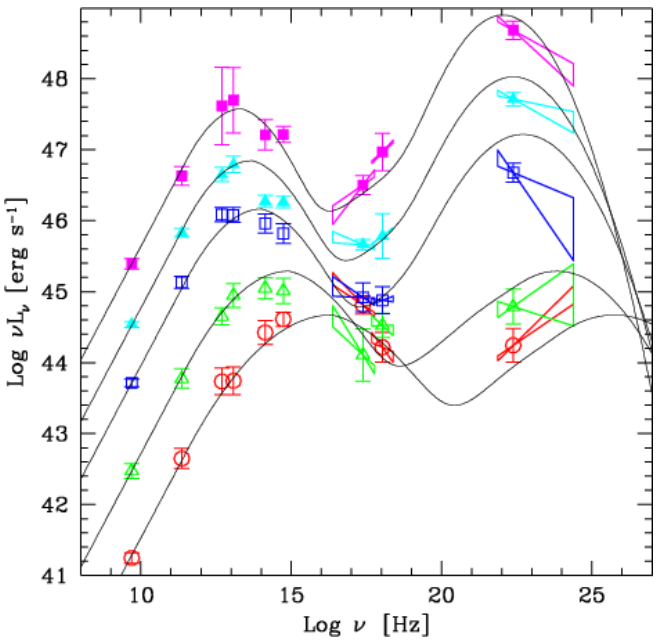

Figure 2.5.: Blazar Sequence: Averaged blazar spectra (Donato et al., 2001, Fossati et al., 1998).

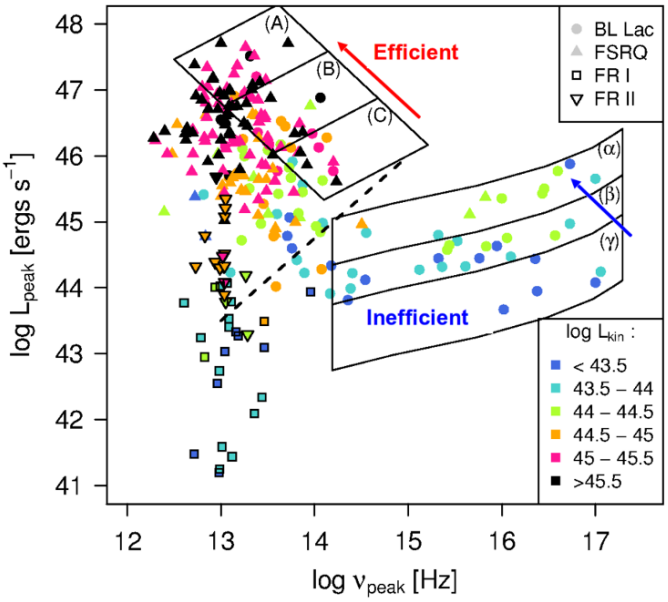

Figure 2.6.: Peak luminosities over peak frequencies for a large sample shows two branches with different behavior. The upper left branched comprises strong-jet sources (FSRQs) and the lower right branch comprises weak-jet sources (Meyer et al., 2012).

In further analysis they find two populations that behave differently. Strong jet sources, such as FSRQs, are found in a separate branch than weak jet sources (Fig. 2.6, Meyer et al., 2012).

2.4.3. Blazar Variability

Blazars show strong variability on time scales of minutes to years. Since the launch of the *Fermi* Gamma-ray Space Telescope γ-ray light curves are available for many sources (see Sect. 3.4). As an example, Fig. 2.7 shows the *Fermi*/LAT light curve of the BL Lac object

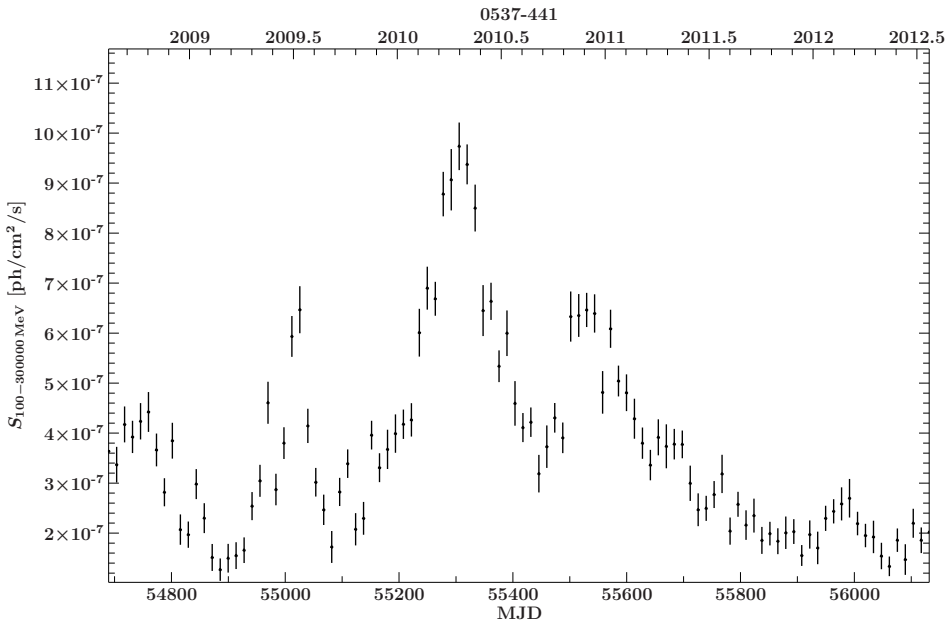

Figure 2.7.: Variability in the *Fermi* light curve of PKS 0537-441.

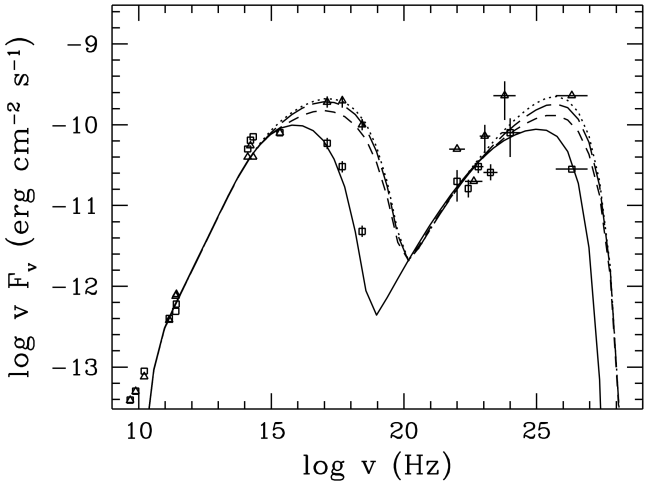

Figure 2.8.: Variability in the SED of Markarian 421 (Mastichiadis & Kirk, 1997).

PKS 0537−441, which shows strong variability. Variability is usually also seen in spectral energy distributions. This explains the need to observe simultaneous at all wavelengths for the physical interpretation of the corresponding spectra. However, broadband SEDs span many orders of frequency and thus require data from several different instruments covering various wavelengths. Strictly simultaneous multiwavelength coverage is therefore not available for many sources or even a large sample of sources.
One can nevertheless construct quasi-simultaneous SEDs by using information about source variability, which is obtained from light curves. This is done by selecting specific time ranges, during which a source varied little or not at all in flux. Multiwavelength data from within this time range are then used to create quasi-simultaneous SEDs. This makes the assumption that variability is similar at all wavelengths. However, this is generally not supported by observations. A high source flux is often first detected at very high or high energies and the emission peak then propagates through the spectrum to lower wavelengths. High source fluxes are thought to be caused by outbursts. In some cases high energetic flares have not been seen in other wavelengths. These are called "orphan flares" (Böttcher, 2005).
Milliarcsecond resolution VLBI images often reveal a central bright component and structures in the jet. These knots in the jet usually travel outwards at superluminal speeds, separate from the core component and diminish in brightness. A possible physical model is the shock-in-jet model (Marscher & Gear, 1985). In this model relativistic electrons are injected into the jet, through which a shock front is propagating. Electrons passing the shock front are accelerated and emit synchrotron radiation. Figure 2.9 shows the evolution of the emitted synchrotron spectrum. High fluxes are seen at higher frequencies first due to higher density near the base of the jet. The medium is not optically thin for low frequencies. During the propagation of the jet, the medium slowly becomes optically thin for lower frequencies. This model can explain the changes of flux observed in broadband spectra.
A difficulty of these models is the "Doppler factor crisis". Very rapid variability has been observed on time scales of minutes for PKS 2155−304 (Aharonian et al., 2007). This variability implies a very small region of emission close to the central black hole. This is a problem when considering the efficiency of energy conversion to synchrotron radiation. Furthermore the detection of γ-rays above the electron rest-mass implies the possibility of pair production. Bulk relativistic motion can explain this as the intrinsic luminosity would be overestimated, however, the necessary Doppler factor is $\delta \geq 100$. Doppler factors can be constrained by

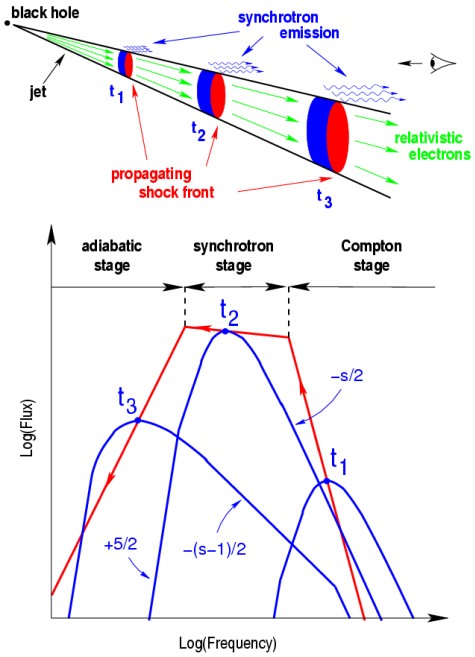

Figure 2.9.: Evolution of synchrotron emission during jet propagation (`http://isdc.unige.ch/~turler/jets/`).

VLBI measurements. MOJAVE results show that usual Doppler factors range between 10 and 50, which is not in agreement with the necessary Doppler factors for very rapid variability (Lister et al., 2009). A possible explanation for this mismatch are non-stationary magnetized outflows (Lyutikov & Lister, 2010) or a spine-sheath layer. In the latter a fast spine in the jet is surrounded by a slower layer, leading to different, but correlated Doppler factors (Ghisellini et al., 2005, Tavecchio & Ghisellini, 2008). An ideal broadband SED of a blazar would be a source simultaneous SED which takes time lags of variability into account. This is only possible if monitoring of a large sample of sources would be available for a time range of several years. The objective of this thesis is the construction and description of a sample of quasi-simultaneous broadband spectral energy distributions for blazars.

2.5. Luminosity and Distances

Source luminosities are an important quantity for describing the properties of AGN, as the luminosity is a distance-independent measurement of the intrinsic source power. The luminosity of a source is given through the flux-luminosity relationship

$$L = F \cdot 4\pi d_L^2. \tag{2.15}$$

This equation is dependent on the integrated flux of the source in a waveband and the luminosity distance d_L. Distance measures for high redshifts have to take the expansion of space into account. Distance functions are usually given as a function of the redshift. They depend on the Hubble parameter, H_0, the total matter density, Ω_m, the dark energy density, Ω_Λ, and the curvatures, Ω_k. The following values of the ΛCDM model were used: $H_0 = 74.3\,\mathrm{km\,s^{-1}\,Mpc^{-1}}$ (Freedman et al., 2012), $\Omega_m = 0.272$, $\Omega_\Lambda = 0.728$ and $\Omega_k = 0$ (Beringer et al., 2012).

For a flat universe, the luminosity distance is given by

$$d_L(z) = (1+z)\, d_C(z), \tag{2.16}$$

where d_C is the comoving distance

$$d_C(z) = d_H \int_0^z \frac{dz'}{E(z')}, \tag{2.17}$$

with the Hubble distance $d_\mathrm{H} = c/H_0$ and where

$$E(z) = \sqrt{\Omega_m (1+z)^3 + \Omega_k (1+z)^2 + \Omega_\Lambda} \tag{2.18}$$

is the Hubble parameter (Carroll et al., 1992).

2.6. X-ray - Radio connection

The luminosity information in different wavebands allows us to search for correlations. Observations of Galactic black holes and Low-Mass X-ray binaries (LMXB) have shown a correlation between their radio and X-ray luminosities $F_\mathrm{radio} \propto F^{0.7}_{X,2-30\,\mathrm{keV}}$ (Gallo et al., 2003, Corbel et al., 2003). In further studies it was found that this correlation might also be present for AGNs. It only depends on the mass, M_BH, the accretion rate, $\dot{M}$, and the spin, a of a black hole (Heinz & Sunyaev, 2003, Merloni et al., 2003, Falcke et al., 2004). The correlation between the radio and X-ray luminosities is given by the following equation.

$$\log L_\mathrm{radio} = (0.60 \pm 0.11) \log L_\mathrm{X} + (0.78^{+0.11}_{-0.09}) \log M_\mathrm{BH} + 7.33^{4.05}_{-4.07} \tag{2.19}$$

The normalization of this correlation might change between flaring and quiet states. This correlation is not valid for blazars, however, many studies suggest that AGN show a similar correlation (Kadler, 2005, Sambruna et al., 1996).

3. Multiwavelength Data

In the previous chapter it was shown that in order to understand AGN multiwavelength observations are needed. For such multiwavelength SEDs of blazars good data coverage across the electromagnetic spectrum (Fig. 3.1) is needed. Figure 3.2 shows the opaqueness of the atmosphere to electromagnetic waves of different wavelengths. Only telescopes that measure at radio, optical or infrared frequencies can successfully observe astronomical objects from the ground. An exception to this are Cherenkov telescopes, which detect very high energies indirectly. High energetic γ-ray photons produce cascades in the atmosphere, which emit optical Cherenkov light. For the detection of a source in the ultraviolet, X-ray or γ-ray regime one has to go to space. In this thesis radio data from the TANAMI array were used. Data by the *Swift* satellite in the Optical/UV and X-ray regime and γ-ray data from the *Fermi* satellite were used. In this Chapter I introduce the telescopes, satellites and instruments used for my analysis.

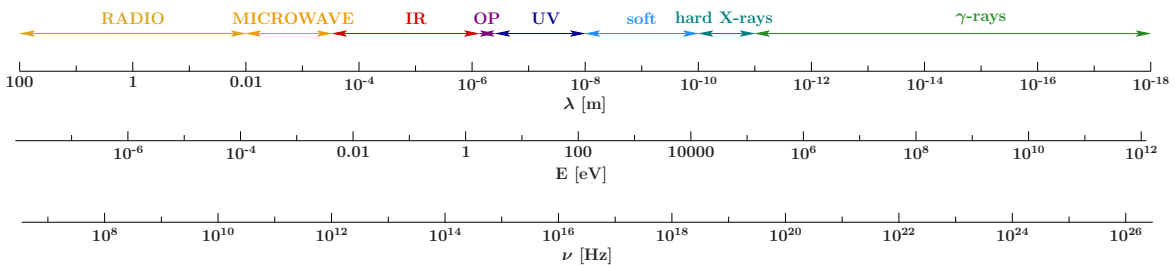

Figure 3.1.: The electromagnetic spectrum from radio to γ-rays, showing the wavelengths, energies and frequencies.

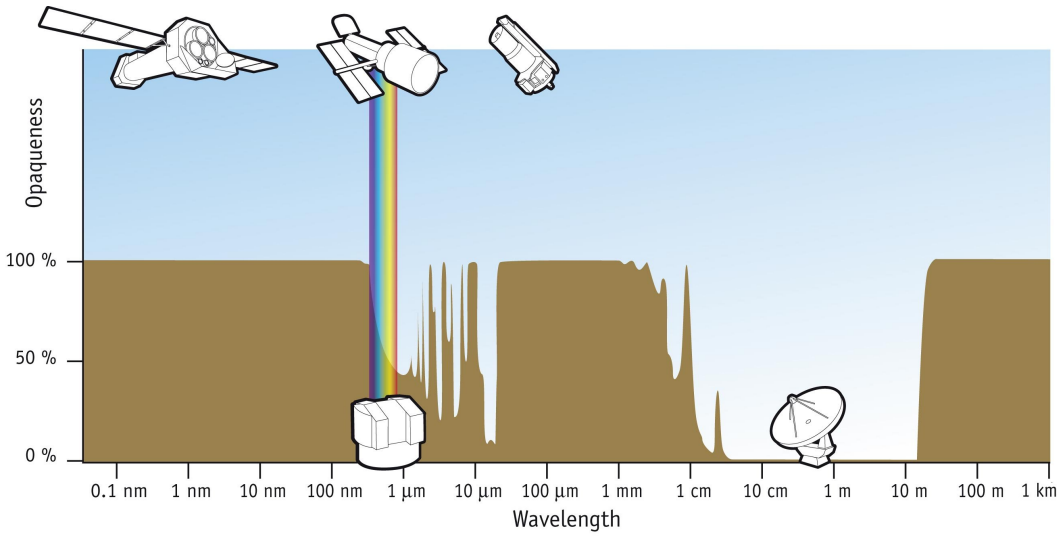

Figure 3.2.: Opaqueness of the Earth's atmosphere (ESA/Hubble/F. Granato).

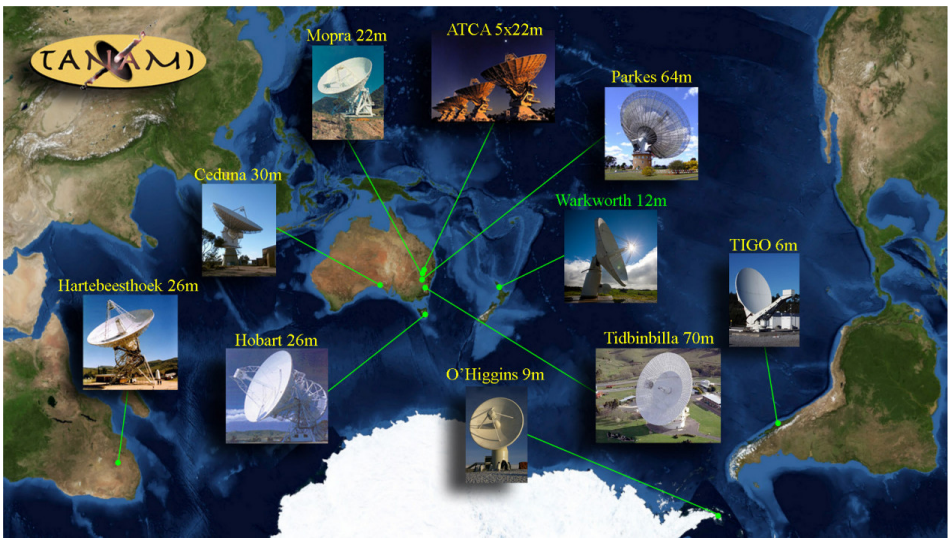

Figure 3.3.: Map of the Southern Hemisphere showing the locations of the radio telescopes in the TANAMI project. (J. Wilms, M. Kadler).

3.1. TANAMI

3.1.1. Introduction to the TANAMI Project

Tracking **A**ctive Galactic **N**uclei with **A**ustral **M**illiarcsecond **I**nterferometry (TANAMI) is a VLBI program monitoring a sample of extragalactic jets south of $-30°$ declination since 2007, complementary to the MOJAVE project on the Northern Hemisphere (Lister & Homan, 2005). The initial sample of 43 sources (Ojha et al., 2010a) has been expanded to 84 since the launch of *Fermi* in 2008. This sample, which consists of radio and γ-ray selected sources, is monitored every $\sim$4 months at 8.4 and 22.3 GHz. Figure 3.3 shows a map of the Southern Hemisphere with the location of the antennas of the TANAMI array. Table 3.1 shows an overview of the radio telescopes in the TANAMI array.

Table 3.1.: The TANAMI array

Telescope	Diameter [m]	Location
Parkes	64	Parkes, New South Wales
ATCA	5x22	Narrabri, New South Wales
Mopra	22	Coonabarabran, New South Wales
Hobart	26	Mt. Pleasant, Tasmania
Ceduna	30	Ceduna, South Australia
DSS43[a]	70	Tidbinbilla, ACT
DSS45[a]	34	Tidbinbilla, ACT
Hartebeesthoek[c]	26	Hartebeesthoek, South Africa
O'Higgins[b,*]	9	O'Higgins, Antarctica
TIGO[b,*]	6	Concepcion, Chile
Warkworth	12	New Zealand

* only operates at 8.4 GHz

[a]Operated by the Deep Space Network of the National Aeronautics and Space Administration

[b]Operated by the Bundesamt für Kartographie und Geodäsie (BKG)

[c]Due to a major failure not available between Sept. 2008 and Sept. 2010

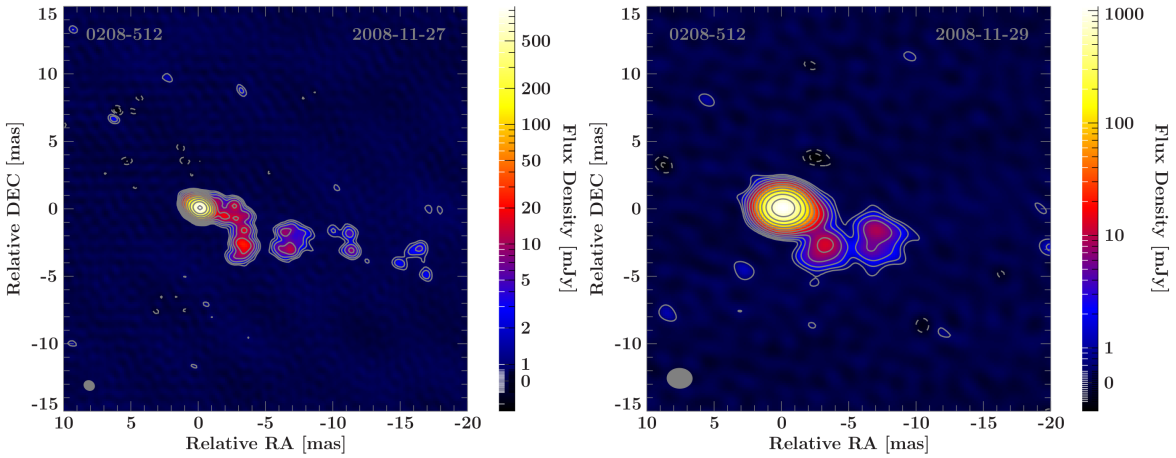

Figure 3.4.: 8.4 GHz (left) and 22.3 GHz (right) contour plot of 0208-512, the color scale indicates the flux density distribution (Kadler et al., in prep.).

3.1.2. Very Long Baseline Interferometry (VLBI)

The advantage of using an array of several radio telescopes is the significant improvement in angular resolution. The angular resolution of a radio telescope is defined by the Rayleigh criterion

$$\sin(\alpha) = 1.22\frac{\lambda}{d}, \tag{3.1}$$

with an angular resolution, α in radians, the wavelength, λ, and the diameter of the telescope, d, which, in case of VLBI, corresponds to the longest distance between two telescopes called baseline. For VLBI techniques all telescopes need to observe simultaneously. The data of each individual antenna are recorded on discs. These discs are accumulated and cross-correlated in a correlator. Data which have been correlated are calibrated in AIPS (van Moorsel et al., 1996). The first step is the a-priori amplitude calibration, which corrects for instrumental and atmospheric effects. The second step is the a-priori phase calibration, which corrects for time delays and changes in the visibility phases. Remaining effects are corrected for using fringe fitting, which allows to search for fringes and correct for remaining time delays. Calibration of TANAMI data is done by R. Ojha. TANAMI data are then read into the program DIFMAP for imaging and model fitting. Details of radio interferometry theory and analysis has been described by Müller (2010a). The TANAMI data analysis of sources used in this thesis was performed by C. Müller, M. Kadler and R. Ojha. Figure 3.4 shows an example of a TANAMI contour plot. At 8.4 GHz (X-Band) a higher resolution is achieved due to the longer baselines of O'Higgins and TIGO, which are not operating at 22.3 GHz (K-Band). The contours in the image represent the significance of the fitted model and are in logarithmic order. The outermost contour corresponds to 3σ. The colors give the flux density in mJy of the model. Both images show a central bright component of the jet, defined as the "VLBI core", as well as a bend in the jet. VLBI images such as these allow us to differentiate between the core flux of the source and the total flux which includes extended emission and the jet.

3.2. X-ray astronomy

3.2.1. Introduction

Earth's atmosphere is opaque to photons of X-ray energies or higher (Fig.3.2), as they are photoabsorbed by oxygen molecules in the atmosphere (Longair, 2011). The US Naval Research Laboratory (NRL) began the research of the ionosphere in the 1920s to explore the possibility of short wave communication (Butrica, 1997). In the 1940s the first X-ray photons from space were detected by Herbert Friedmann, who used a V2 rocket to measure solar X-rays using a Geiger counter.

"Data telemetered continuously from photon counters in a V-2 rocket, which rose to 150 km at 10:00 AM on September 29, 1949, showed solar 8 Å x-rays above 70 km and 95 km, and ultraviolet light around 1200 Å and 1500 Å above 70 km and 95 km, respectively. The results indicated that solar soft x-rays are important in E layer ionization, that Lyman α-radiation of hydrogen penetrates well below E layer, and that molecular oxygen is rapidly change to atomic form above 100 km. (Friedman et al., 1951)"

20 years later Riccardo Giacconi and Bruno Rossi searched for extrasolar X-rays, also using rockets. However, their search for fluorescent X-ray photons from the moon failed. Instead they detected a very bright X-ray source, Scorpius X-1 (Giacconi et al., 1962). The first X-ray satellite was launched in 1970. *UHURU* discovered many bright X-ray sources (Jagoda et al., 1972, Forman et al., 2012). Several satellite missions followed. The *ROSAT* satellite was launched in 1990 and was the first satellite to perform a survey of the whole sky. The ROSAT All Sky Survey (RASS) is still the largest source catalog with ∼120000 X-ray sources (Voges et al., 1999, 2000). Currently there are several X-ray and γ-ray missions, including *Swift*, the *X-ray Multi-Mirror Mission - Newton* (*XMM-Newton*), *Chandra*, the *International Gamma-Ray Laboratory (INTEGRAL)*, *Fermi*, *Suzaku*, and *AGILE*. In the following Section I give a brief description of X-ray astronomy, optics, and detectors following Bradt (2004), Aschenbach (1985) and Lutz (2001).

3.2.2. Wolter telescopes

Optical telescopes usually consist of two mirrors, which reflect the incoming light. X-ray photons however, are not reflected by those mirrors.
Snell's law describes the angles of incident in relation to the refractive index of two media (Aschenbach, 1985, Wolf & Krotzsch, 1995, Rashed, 1990),

$$\frac{\sin\alpha_1}{\sin\alpha_2} = \frac{n_2}{n_1} = n. \tag{3.2}$$

For total reflection ($\alpha_2 = 90°$) the refractive index n has to be greater than one. It can be described by the dielectricity constant, ε and the permeability of the material, μ,

$$n = \sqrt{\varepsilon\mu}. \tag{3.3}$$

Using the dielectricity constant for free electrons (Jackson, 1981) gives

$$\varepsilon = 1 - \left(\frac{\omega_p}{\omega}\right) = 1 - \frac{nZr_e}{\pi}\lambda^2 \text{ with } \omega_p = \frac{4\pi nZe^2}{m_e} \tag{3.4}$$

and

$$n = \sqrt{1 - \frac{nZr_e}{\pi}\lambda^2} = 1 - \frac{\rho}{(Z/A)m_u}\frac{r_e}{2\pi}\lambda^2 =: 1-\delta \quad \cos\Theta_c = n = 1-\delta. \tag{3.5}$$

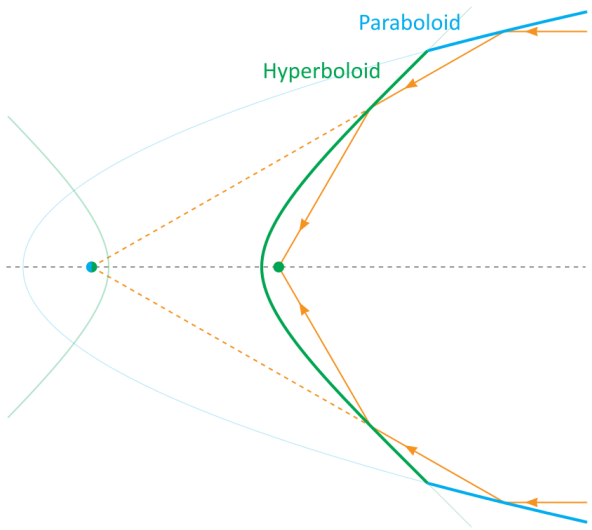

Figure 3.5.: Wolter type I schematic (https://lp.uni-goettingen.de/get/text/7272).

Using a Taylor series this can be approximated by

$$\Theta_c = \sqrt{2\delta}. \tag{3.6}$$

For X-ray wavelengths ($\lambda \sim 1\,\mathrm{nm}$) the reflection angle is $\Theta_c \sim 1°$. X-ray mirrors are also known as "grazing incidence telescopes", due to the reflection of photons at small angles. The reflection can further be increased by using materials with a high atomic number Z. In most cases gold or iridium are used for the surface of the mirror.
Paraboloids focus X-rays very well, but the focal lengths are not easily manageable due to limited rocket length. In a Wolter telescope, paraboloids are combined with hyperboloids to shorten the focal lengths. X-ray photons are thus reflected twice (Fig. 3.5). To increase the effective area of the mirrors, several mirror shells are nested (Fig. 3.6). The X-ray photons are then focused onto a CCD detector. CCD detectors in X-ray astronomy are described in the following Section.

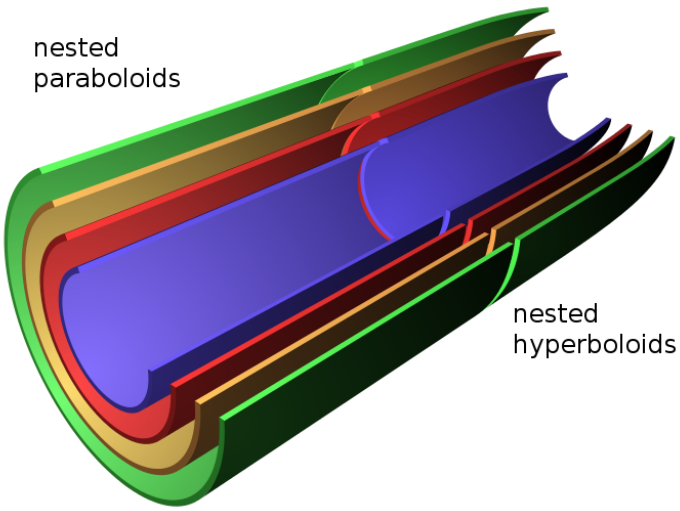

Figure 3.6.: Wolter type I schematic (https://lp.uni-goettingen.de/get/text/7272).

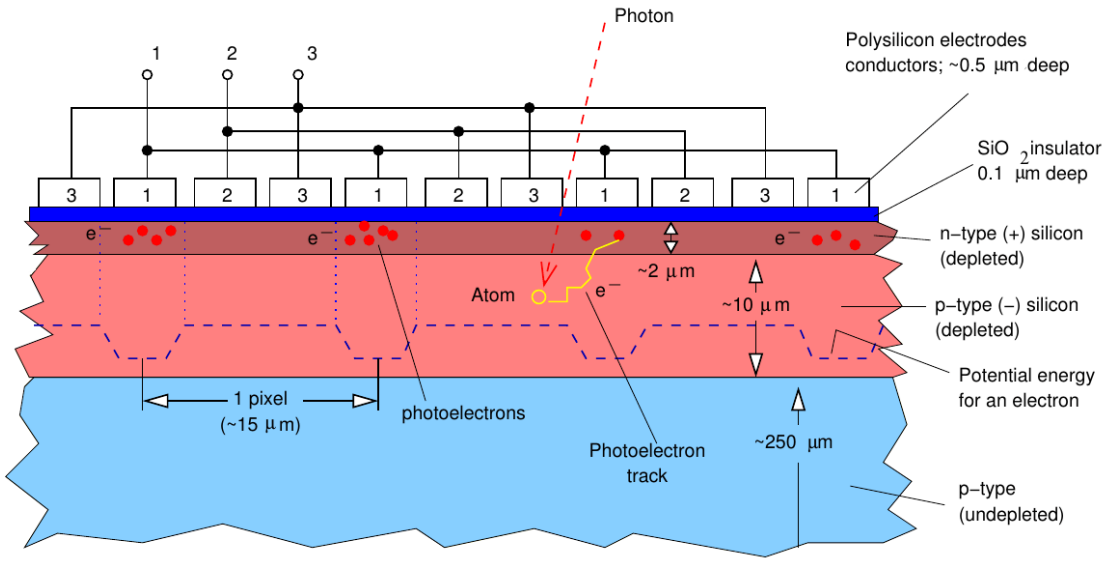

Figure 3.7.: Structure of a X-ray CCD during exposure, an incident X-ray photon (red) excites electrons, which are accumulated in potential wells (Wilms after Bradt, 2004).

3.2.3. Charge Coupled Device (CCD)

Charge Coupled Devices (CCD) in X-ray astronomy are similar to CCDs that are in use in optical astronomy. X-ray CCDs have to be modified, as the incident photons have higher energies than visible light and thus a larger penetration depth. The structure of a CCD is shown in Fig. 3.7. CCDs are solid state devices and consist of a semiconductor. This is usually silicon doped with impurities (Lutz, 2001). P-type and n-type semiconductors are joined in a CCD. These pn-junctions have depletion layers, where electrons and holes have recombined. When applying an electric field to the CCD, the size of the depletion region increases. The pn-junction in a CCD is usually fully depleted by applying a depletion voltage. This results in a large volume for the X-ray photons to interact with the material. Incident X-ray photons excite several thousand electron-hole pairs in the silicon. These electrons gain enough energy to contribute to the conduction. They are accumulated in a potential well (pixel). By changing the gate voltages the electrons in each pixel can be moved in one direction and read out. Some CCD detectors use frame stores, where the whole CCD image is stored shortly and then slowly read out. This improves the dead time of the detector. Background features and damage to the *Swift*/XRT CCD will be discussed in Section 3.3.3.

3.3. *Swift Gamma-Ray Burst mission*

The *Swift* satellite was launched on 20 November 2004 into a low Earth orbit. It is managed by the NASA Goddard Space Flight Center. *Swift's* main mission is to detect and observe γ-ray bursts (GRB) and perform follow-up observations at optical, ultraviolet and X-ray wavelengths (Gehrels et al., 2004). The main goals are to determine the origin of γ-ray bursts and to thus study the evolution of the early universe.
In between GRBs *Swift* has a Guest Investigator Program, a Target of Opportunity(ToO) program as well as a Fill-In program. *Swift's* Guest Investigator (GI) Program is a part of NASA Headquarters' Research Opportunities in Space and Earth Sciences (ROSES) Announcement, which allows astronomers to request time for observations of astronomical sources. The Target of Opportunity program has a limited amount of time for the observation of non-GRB

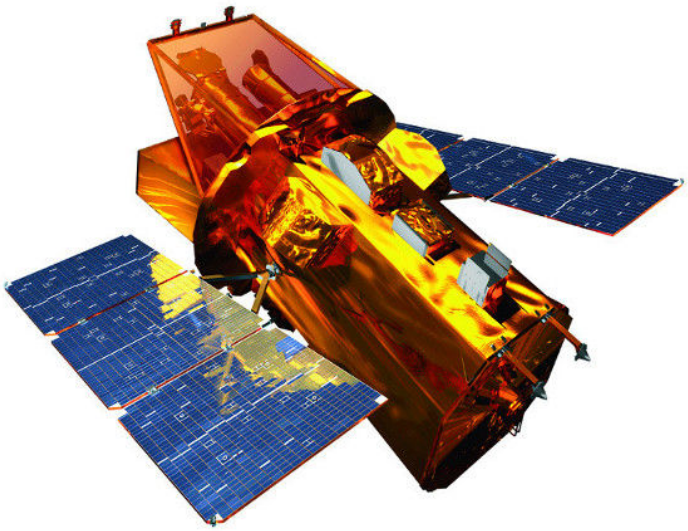

Figure 3.8.: The *Swift* satellite (NASA E/PO, Sonoma State University, Aurore Simonne).

events. This includes transient events such as supernovas, pulsar outburst and blazar flares. The Fill-In program allows to request time for a large number of sources, which are used to fill gaps between observations or between large slewing angles. The available time for each program is listed in Table 3.2. TANAMI sources are observed with *Swift* as a part of the Fill-In program.

Table 3.2.: Cycle 9 Time Availability for the *Swift* programs (`http://heasarc.gsfc.nasa.gov/docs/swift/proposals/swiftgi.html`).

Program	Time
Non-ToO Targets	2 Msec
Fill-in Targets	1 Msec
ToO Targets	1 Msec
Large Programs	1 Msec

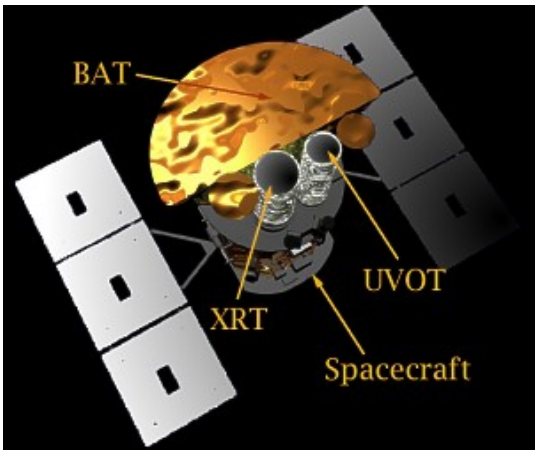

Figure 3.9.: Instruments on board *Swift* (`http://www.swift.psu.edu/`).

Swift's three instrument (as seen in Fig. 3.9) are the Ultraviolet and Optical Telescope (UVOT), the X-ray Telescope (XRT) and the Burst Alert Telescope (BAT)

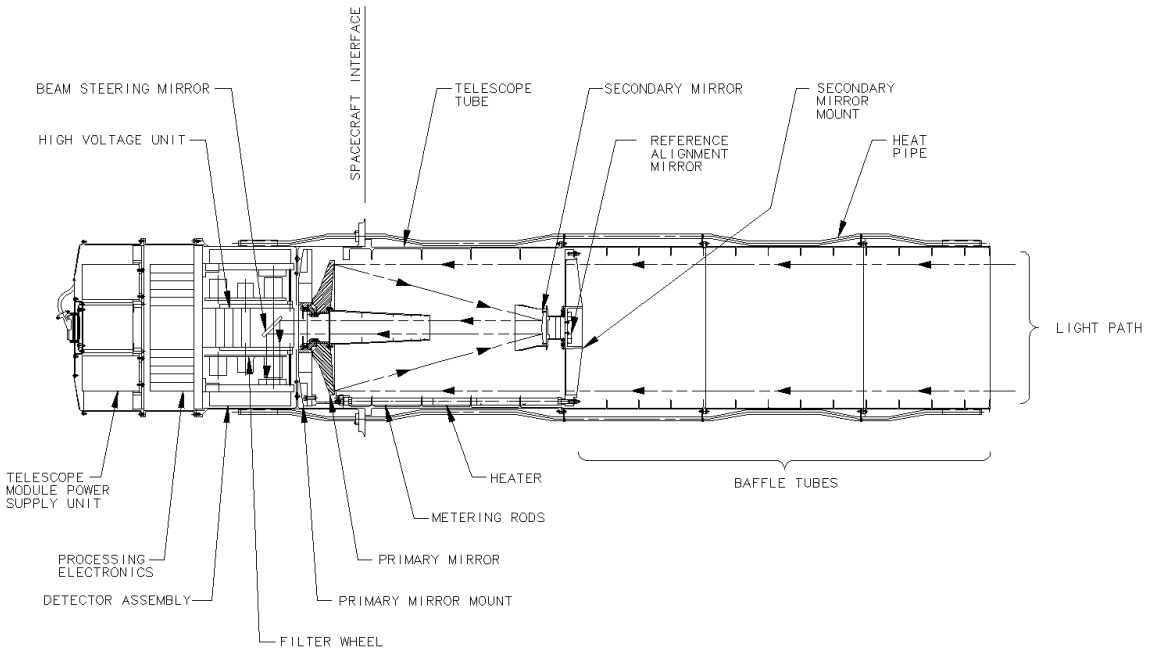

Figure 3.10.: Schematic design of the *Swift*/UVOT telescope (`http://www.mssl.ucl.ac.uk/general/projects/swift/assets/ea3sk1342b.gif`).

3.3.1. UltraViolet and Optical Telescope

The UltraViolet and Optical Telescope (UVOT) on board *Swift* is co-aligned to the X-Ray Telescope. It provides simultaneous coverage at optical and ultraviolet wavelengths (Gehrels et al., 2004, Roming et al., 2005).

Table 3.3.: UVOT Instrument Characteristics (Roming et al., 2005)

Telescope	Modified Ritchey-Chrétien
Mirror	Zerodur
Focal ratio	12.72
Telescope PSF	2.5 arcsec @ 3500 Å FWHM
Field of view	17 × 17 arcminutes
Detector	Intensified CCD
Detector operation	Photon counting
Detection element	256 × 256 pixels
Sampling elements	2048 × 2048 pixels after centroiding
Pixel scale	0.502 arcsec
Wavelength Range	1700-6500 Å
Filters	7/11
Sensitivity	B=22.3 @ 1ksec in white light
Brightness Limit	V=7.4mag
Timing resolution	11.0329 ms
Gain	1.0 count ADU^{-1}
Dark current	7×10^{-5} counts s^{-1} $pixel^{-1}$

The UVOT consists of the UV/optical telescope, the Beam Steering Mirror, two filter wheel mechanisms, two photon counting detectors, power supplies and electronics. This can be

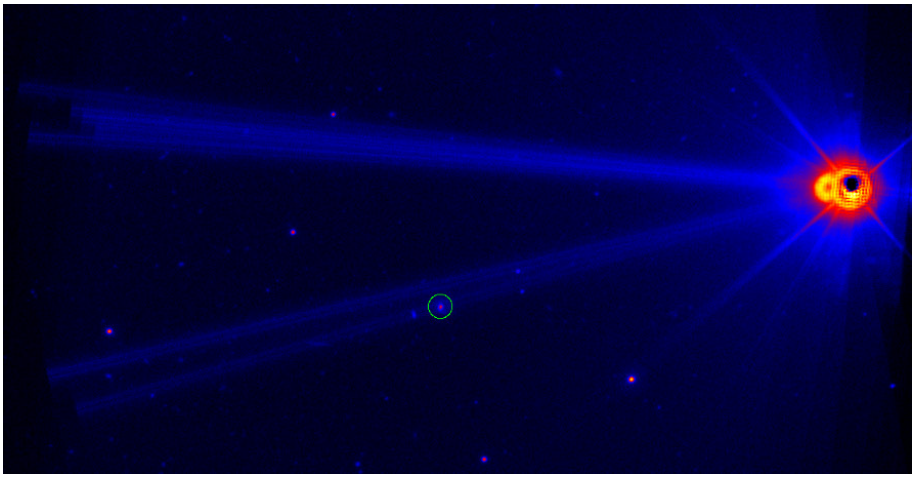

Figure 3.11.: Bright optical source in field of view, target source marked by green circle, observation 00037385001.

seen in detail in Fig. 3.10.
The *Swift*/UVOT optics are flight spares from the *XMM-Newton* Optical Monitor (OM). The analysis of UVOT data is described in Section 4.2.2.
There are several type of image artifacts in optical images. Artifacts are caused by internal reflections within the detector window and reflections of off-axis starlight and background light. Internal reflections causes out of focus ghost images, which have been named"smoke ring". The ghost image is an image of the star, radially displaced (Ehle et al., 2003).
Figure 3.11 shows the very bright star Izar (ϵ Boötis). A smoke ring is also visible. The bright spikes are due to diffraction off of the spider, which holds the secondary mirror in place.
Figure 3.12 shows three color images of Centaurus A that have been created with SAOImage DS9. The bright star in the lower left corner also shows a smoke ring in the left image. In both images the dust lane is clearly visible.

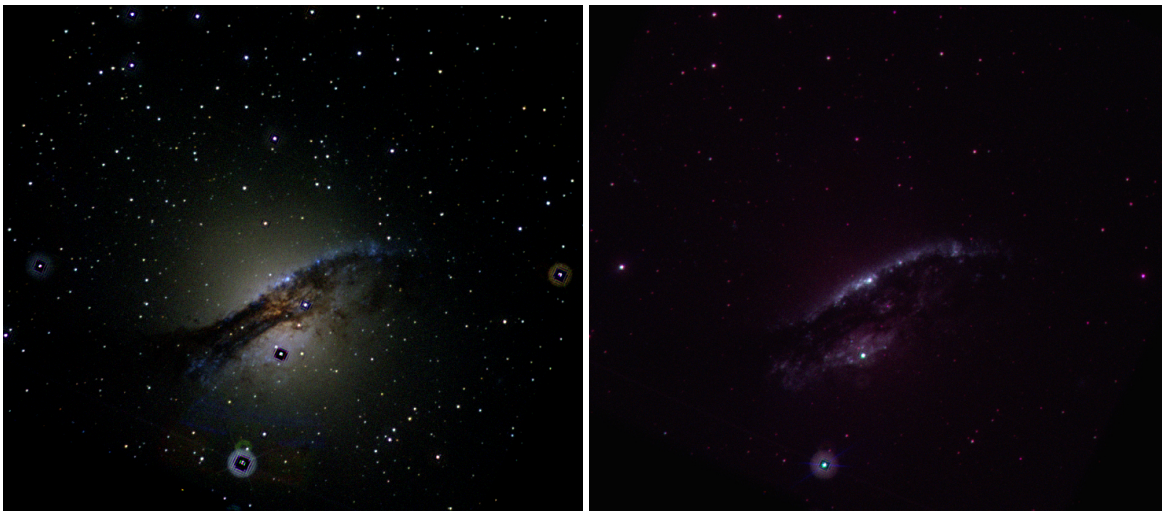

Figure 3.12.: Three color images of Centaurus A, using the V, B, and U filters (left) and the UVW1, UVM2, and UVW2 filters (right), observation 00050950005.

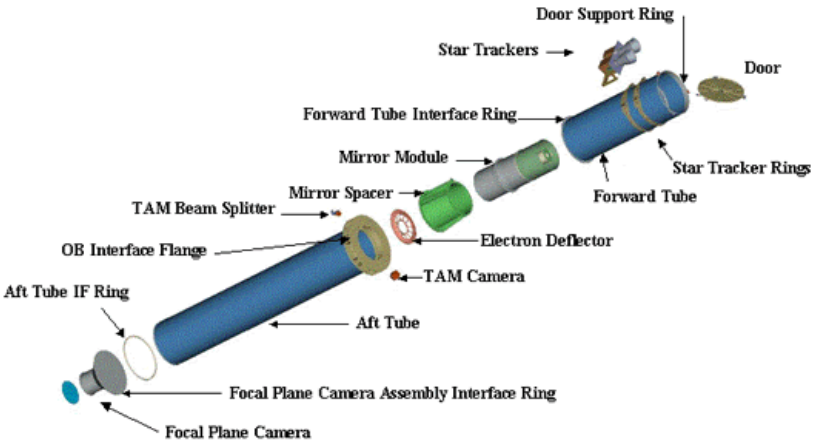

Figure 3.13.: The design of the XRT (`http://www.swift.psu.edu/xrt/images/XRT_exploded1a.gif`).

3.3.1.1. *Swift*/UVOT data reduction

Extraction of UVOT data starts with Level 2 products. The UVOT data reduction pipeline has been run on images and event files. UVOT data extraction is done by using the perl scripts provided by NASA as a part of the HEASoft/FTOOLS package (Blackburn, 1995, Irby, 2012). The first step is to sum a series of images and their corresponding exposure maps of one individual observation. This is done using the HEASoft tool uvotimsum. The second step is to create a FITS file that can be used for spectral fitting. This is done using the uvot2pha tool. An optional third step is to use the tool uvotsource to calculate flux densities, magnitudes and other information and save these in a FITS file. In my extraction of UVOT data I only used the files resulting from uvot2pha. UVOT data are being corrected for effects of interstellar extinction as a part of the fit function (Sect. 4.2.3).

3.3.2. X-Ray Telescope

The X-Ray Telescope (XRT) on board *Swift* was designed and built to measure light curves, spectra, and fluxes of γ-ray bursts (GRB). *Swift's* X-Ray Telescope consists of a grazing incidence Wolter Type-I telescope module, as well as a focal plane camera assembly. Details

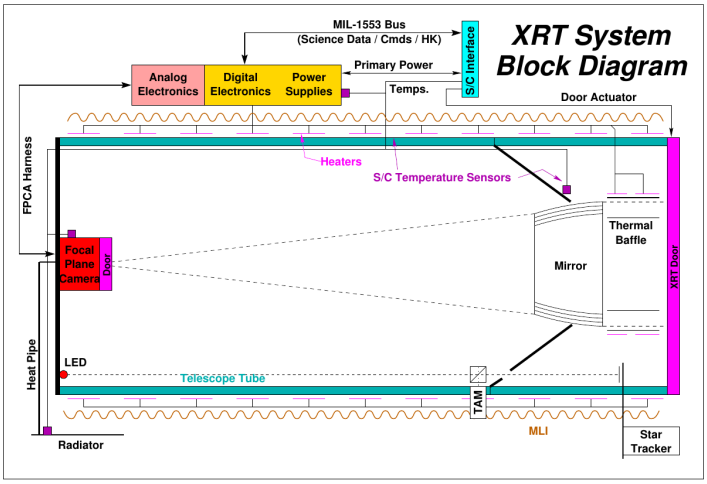

Figure 3.14.: Block diagram of the XRT (Burrows et al., 2005).

Table 3.4.: XRT Instrument Characteristics (Burrows et al., 2005)

Telescope	JET-X Wolter I
Focal Length	3.5 m
Effective Area	110 cm^2 @ 1.5 keV
	20 cm^2 @ 8.1 keV
Telescope PSF	18 arcsec HPD @ 1.5 keV
	22 arcsec HPD @ 8.1 keV
Detector	EEV CCD-22
Detector format	600 × 602 pixels
Pixel size	40 μm × 40 μm
Pixel scale	2.36 arcsec/pixel
Field of view	23.6 × 23.6 arcminutes
Position accuracy	3 arcsec
Time resolution	0.14 ms (PD), 1.8 ms (WT), 2.5 s (PC)
Energy range	0.2-10 keV
Energy resolution	140 eV @ 5.9 keV (launch)
Sensitivity	2×10^{-14} erg cm^{-2} s^{-1} in 10^4s (PC)

can be found in Table 3.4 and in Figs. 3.13 and 3.14. In this section I give a description of the *Swift*/XRT and its performance following Gehrels et al. (2004), Burrows et al. (2005), Osborne et al. (2005) and Short et al. (2003).

3.3.2.1. *Swift*/XRT Mirrors

The XRT mirrors were originally built for JET-X, which was part of the original version of the Spectrum X-Gamma spacecraft (Citterio et al., 1996, Wells et al., 1992). The XRT mirror system consists of 12 concentric, gold-coated, electroformed nickel shells with a length of 600 mm and a focal length of 3.5 m, as well as a thermally controlled and optically monitored carbon fiber telescope tube. The mirrors have to be kept at $20 \pm 5°$ C with gradients of $< 1°$ to prevent degradation (Short et al., 1998, Holland et al., 1996). They are held in place by front

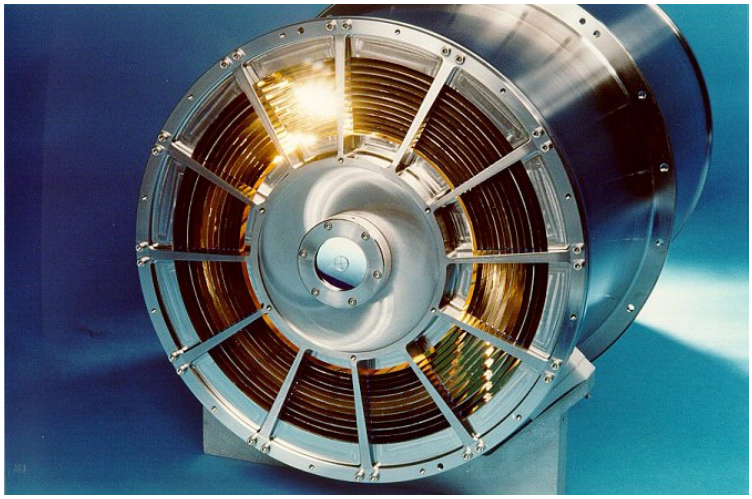

Figure 3.15.: The XRT mirror module (Burrows et al., 2005).

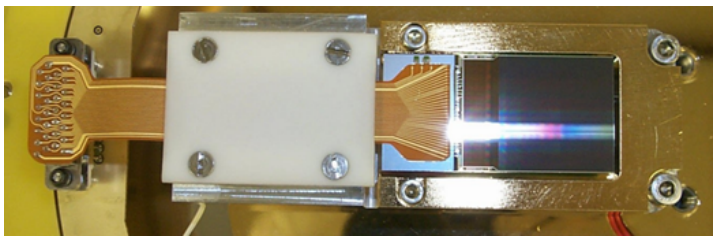

Figure 3.16.: The XRT EEV CCD-22 (`http://www.swift.ac.uk/about/XRThardware.php`).

and rear spiders (Fig. 3.15).

3.3.2.2. *Swift*/XRT Focal Plane Camera Assembly (FPCA)

The Focal Plane Camera Assembly (FPCA) consists of an EEV CCD-22, a sun shutter, 4 ^{55}Fe calibration sources, as well as an optical blocking filter. The sun shutter functions automatically and closes when the angle between the pointing direction of the telescope and the sun is too small. The performance of the CCD can be studied over time using the calibration sources. The blocking filter reflects visible light with an optical transmission of 0.25% (Osborne et al., 2005).
The CCD was originally designed for the *XMM-Newton* MOS instruments. It is a front illuminated three-phase frame-transfer device, which uses high-resistivity silicon and an open-electrode structure (Holland et al., 1996). This results in a band pass of 0.2-10 keV, however, below $\sim$ 0.5 keV the effects of charge trapping and loss to surface states become significant (Short et al., 1998). Surface losses can be seen in Fig. 3.18. The CCD was intended to operate at 173°K to ensure a low dark current and to reduce the sensitivity to irradiation by protons. Due to the failure of the active Peltier cooling device shortly after launch the CCD is passively cooled and has to be kept at $<$ 223°K. Passive cooling is achieved by minimizing the radiator's exposure to Earth. Therefore targets are preferred that allow a pointing of *Swift* in a "good" direction. Time in the South Atlantic Anomaly (SAA) is used for pointing at "cold targets" (Kennea et al., 2005a,b).

3.3.2.3. *Swift*/XRT data reduction

Reduction of XRT data was done by using scripts that were written by Laura Barragán and Jörn Wilms. The steps in these scripts will be summarized briefly.

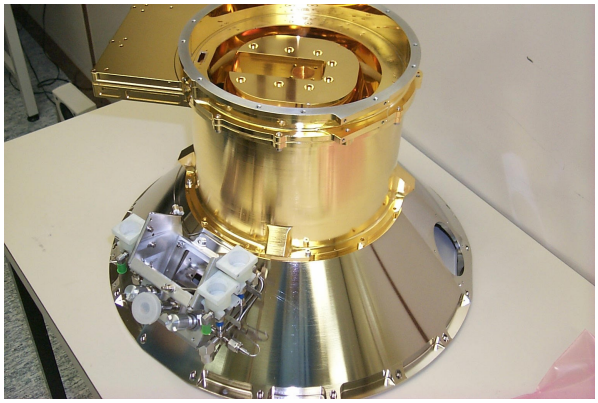

Figure 3.17.: Focal Plane Camera Assembly (`http://www.swift.psu.edu/xrt/images/FPCA1.jpg`).

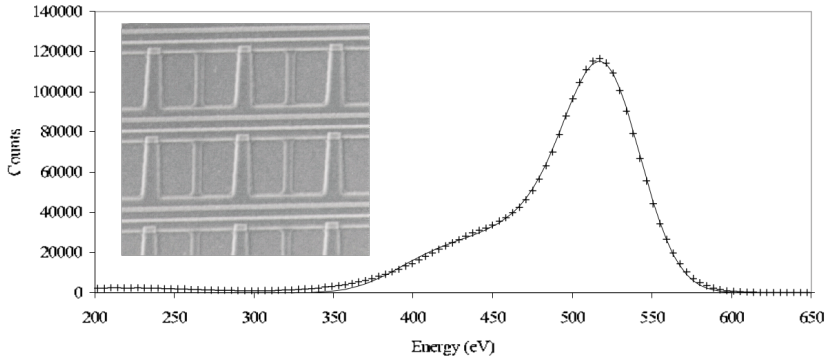

Figure 3.18.: Asymmetric surface losses due to open electrode structure (inset), calibration data (points) and analytic model (line; Short et al., 2003).

The extraction for Photon counting mode data starts with Level 1 data. These are images and event files that have been reformatted into FITS files. The first step is to run the perl script xrtpipeline, which calibrates the data. The xrtpipeline first transforms the coordinates from the raw values to sky and detector coordinates using satellite attitude information. Bad pixels and the calibration sources are flagged and events are assigned to a grade. Anomalous pixels (hot and flickering pixels) are searched for and are also flagged. In the last step Pulse Invariant (PI) values are calculated. These values account for changes in gain due to Charge Transfer Inefficiency (CTI). In the second step screening criteria are applied and Good Time Intervals (GTI) are calculated. After running the xrtpipeline the screening criteria are being applied to the data via the XSELECT software. Screening criteria include the following parameters:

- Removal of calibration sources
- Removal of dead, hot, saturated and flickering pixels
- Grade selection

Other criteria, which are screened for automatically, include the elevation angle, the bright earth angle, the sun angle, as well as the temperature of the CCD. The latter is usually kept within $-47°\ \mathrm{C} \geq \mathrm{T_{CCD}} \leq -102°\ \mathrm{C}$. For PC mode the grades 0–12 are selected and for WT mode grades 0–2 are used.
After applying screening criteria high-level products can be extracted using XSELECT. These files include images, light curves and spectra.

3.3.3. Performance of the *Swift*/XRT

The XRT operates its CCD in different readout modes. These are described in detail by Burrows et al. (2005) and Hill et al. (2004).

Image Long and Short (IM): This mode obtains an image to determine the position of a new GRB rapidly. The CCD collects charge on the detector and reads out without any event recognition. The image is being processed on board, but will be piled-up and only used to acquire a position and a rough flux estimate.

Low rate (LR) and Piled-up Photodiode(PU): This mode is for very bright sources and high time resolution. It performs one serial clock shift and one parallel clock shift alternately. The CCD continues to readout before the whole frame has been read out. This results in a very fast readout, but the charge accumulated in one readout pixel includes charge from every pixel of the CCD, but not simultaneous in time. The time resolution is 0.14 ms and the flux level 0.6–60 Crab.

Windowed Timing (WT): Windowed Timing mode is obtained by reading out the central 200 columns and binning 10 rows in the serial register. This covers the central 8 arcminutes of the field of view and allows for one dimensional imaging. The time resolution is 1.7 ms and the flux level 1–600 mCrab.

Photon Counting (PC): The CCD operates in the „frame-transfer"configuration. Each frame is read out by storing a whole frame in the frame store and then clocking it, one row at a time, into the serial register. The bias is subtracted and the events reconstructed. This is done by testing whether the central pixel of a 3×3 matrix is the local maximum and whether it is between the discriminator and upper level thresholds. Then the outer ring pixels (a 5×5 matrix) are tested in the same way. This procedure eliminates many chip defects and cosmic rays. Valid events are telemetered in a 3×3 matrix. The time resolution is 2.5 seconds and the flux level is less than 1 mCrab.

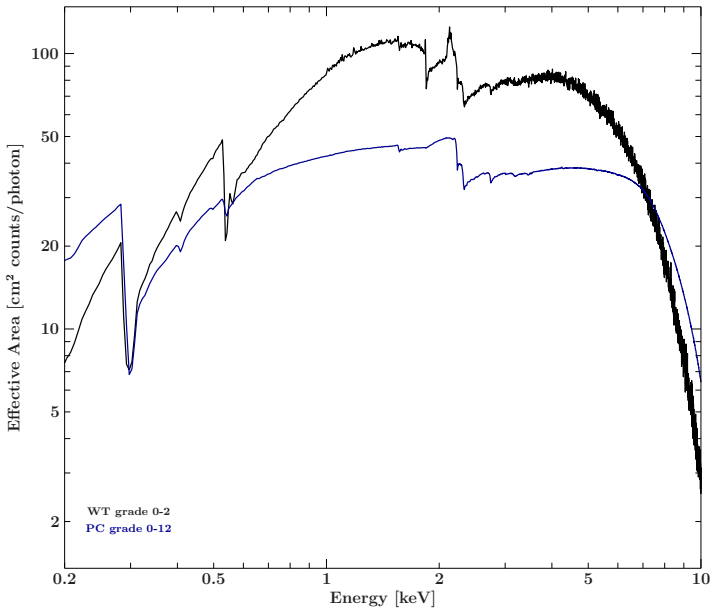

Figure 3.19.: Ancillary response function (ARF), effective area of the XRT.

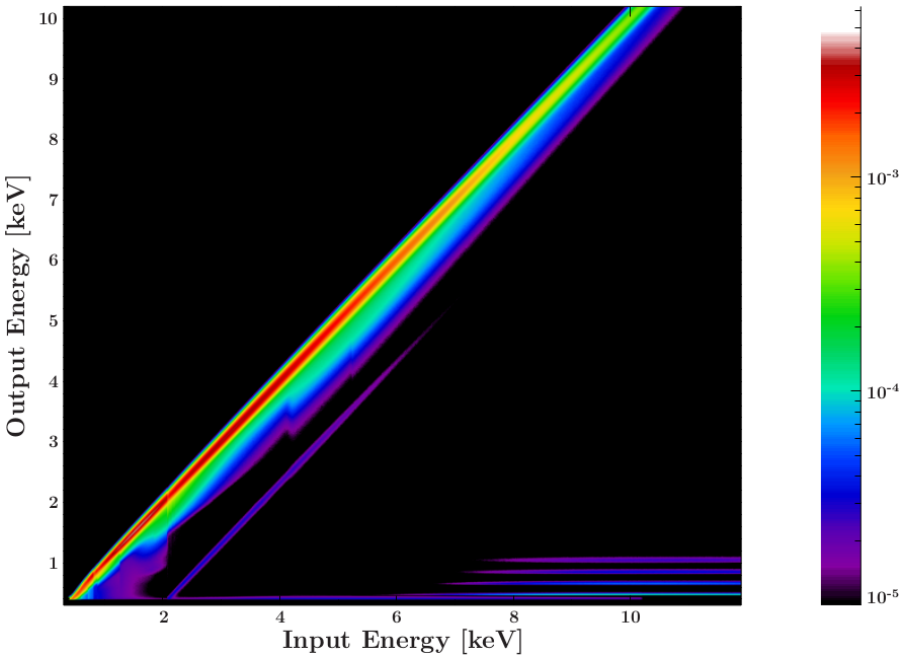

Figure 3.20.: Redistribution Matrix Function (RMF) of the XRT.

During an observation of a new GRB (Automatic Target) the XRT automatically changes modes. The first step is to take an image (Image Mode) to calculate the source position. Then the following modes are used: Photodiode, Windowed Timing and Photon counting, depending on the intensity of the source. For Pre-Planned Targets (PPT) no image in Image mode is scheduled (Hill et al., 2004). During my analysis of *Swift* data only data in Photon counting and Windowed timing mode were used.
Figure 3.19 shows the effective area of the XRT. The black line shows the effective area of the Windowed timing mode and the blue curve corresponds to Photon counting mode. The 0.54 keV feature is an oxygen transition in the surface of the detector. A silicon K-edge is visible at 1.84 keV. The prominent edges at 2.2-3.425 keV are due to a change in the reflectivity at the Au M-edge of the mirrors (Fraser et al., 1994, Owens et al., 1996, 1997).
Figure 3.20 represents the Redistribution Matrix Function of the XRT. It shows the energy at which a photon is detected compared to its original energy. It is easily discernible that most of the incident photons are detected at their original energy. However, there is an escape peak visible at -2 keV of the original photon energy. This is due to the escape of a fluorescence photon of a K-shell transition. A Compton shoulder is also visible at < 2 keV. In the following sections I give an overview of the various background effects in the *Swift*/XRT CCD.

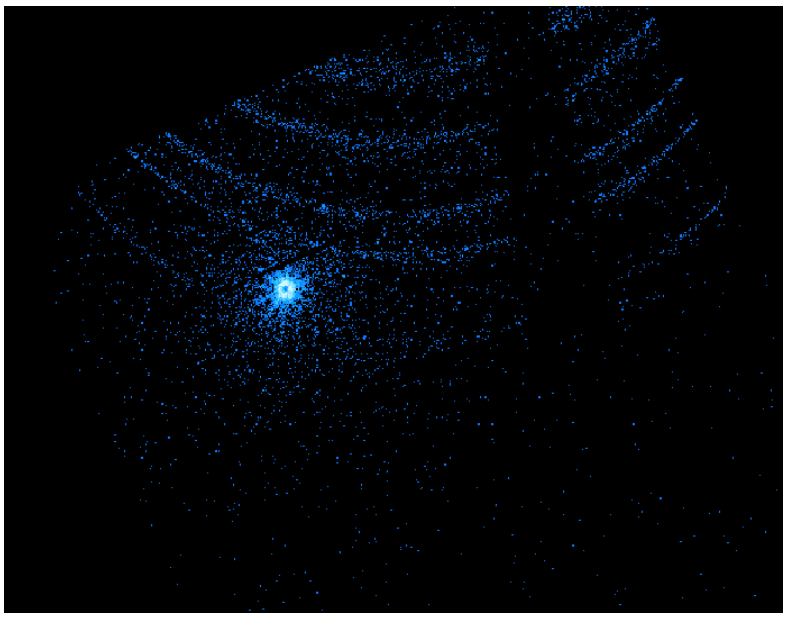

Figure 3.21.: Stray light in Observation 0003096101.

3.3.3.1. Stray light

Observation 0003096101 (Fig. 3.21) shows stray light contamination in the clean detector image. Stray light are photons from bright X-ray sources that are outside the field of view. These photons are reflected only once off of the shells of the Wolter telescope. The target of the *Swift* observation is GRS 1758−258, which is close to the Galactic plane. The bright source outside the field of view causing the stray light is probably 4U 1758−25.
Figure 3.22 shows an illustration of stray light for the eROSITA project. The green arrows represent the photons from within the field of view which are reflected twice off the mirrors.

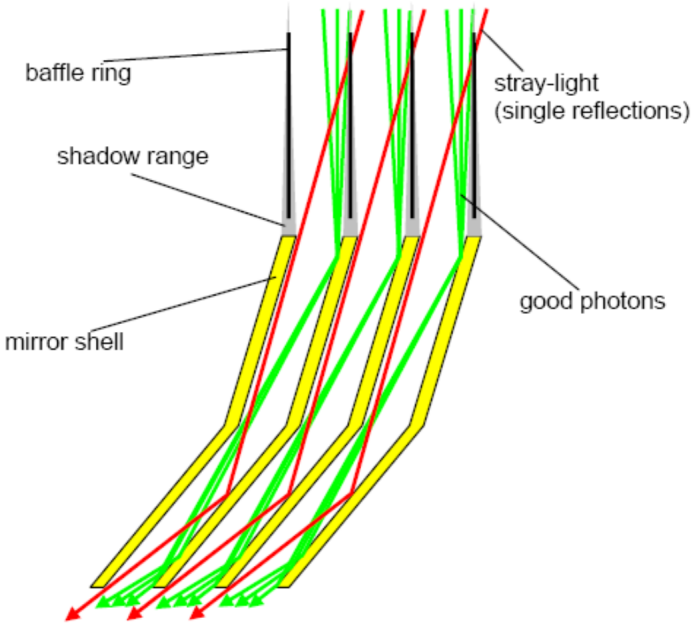

Figure 3.22.: Stray light schematic for eROSITA, showing the incident photons (green) and stray light photons (red) and a baffle ring (black); image courtesy Peter Friedrich.

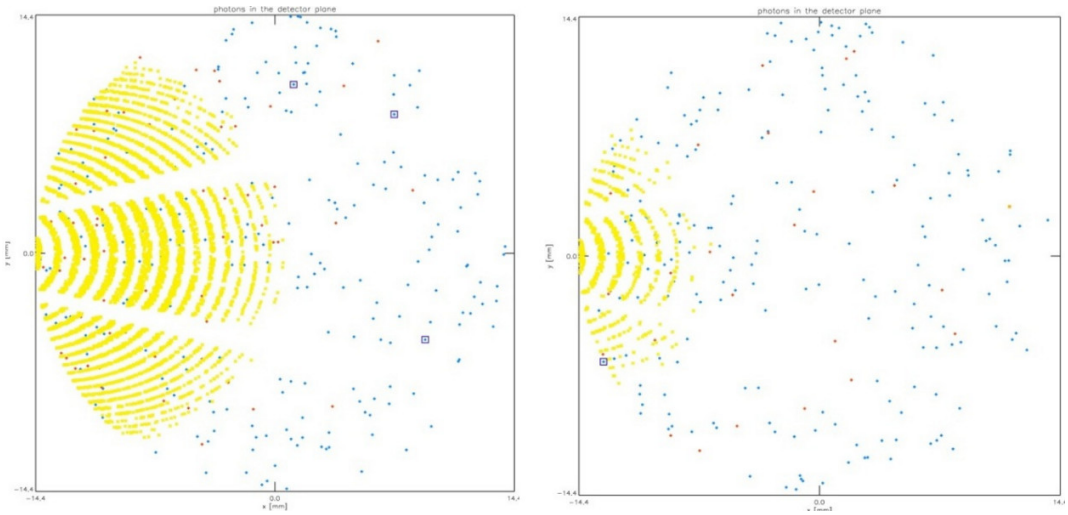

Figure 3.23.: Stray light Simulation for eROSITA, showing the difference between stray light contamination without (left) and with a baffle (right), image courtesy Peter Friedrich.

As done for the eROSITA instrument, the effect of stray light (in red) could in principle be alleviated significantly by adding a baffle (Fig. 3.23), however, the *Swift* telescope has no baffle against stray light.

3.3.3.2. Bright Earth

The Bright Earth angle is the angle between the pointing of the satellite and the day-night terminator. Usually data are excluded, when the bright earth angle is lower than 120°. If the satellite pointing is close to 120° or smaller a high soft X-ray flux is detected. This is due to solar photons, which are scattered in the upper atmosphere (Fink et al., 1988).
Figure 3.24 shows the effect of a low bright earth angle in an unfiltered detector image. Unfiltered images are Level 1 image files, whereas clean images have been calibrated and

Figure 3.24.: Unfiltered detector image of observation 00040486002.

Figure 3.25.: XRT Blocking Filter(white circular filter) and Proton Shield in FPCA (Burrows et al., 2005)

are Level 2 files. The bright line is a cosmic ray, possibly a muon, which hit the detector at the time of the observation.

3.3.3.3. Optical Loading

X-ray CCDs are sensitive to optical light, as the band gap of silicon is of the order of a few electron volts. A thin filter is installed in front of the CCD to block optical light (Fig. 3.25). The filter consists of a 1840 Å polyimide film, which has been coated with 488 Å of aluminum. This results in an optical transmission of only 0.25% (Burrows et al., 2005). Bright optical sources can cause charge in the CCD. The electrons that are liberated in the CCD are converted into a Digital Number (DN). The connection between the digital number and the gain factor g is as follows

$$\mathrm{DN} = \frac{\mathrm{N}_{e^-} \cdot 3.65}{g} \tag{3.7}$$

where g = 2.67 eV/DN (Evans, 2012). For bright sources this can affect the X-ray energy and grade calibration. Very bright sources can lead to a rejection of X-ray events, as only events

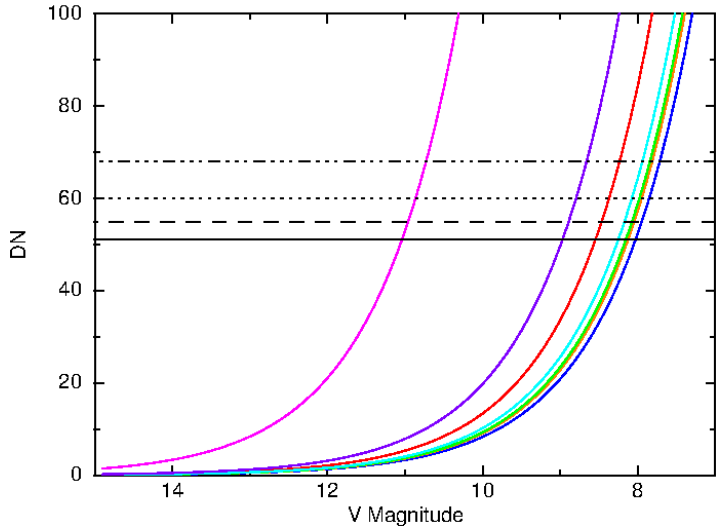

Figure 3.26.: DN over the apparent V magnitude; Magenta:M8, Purple:M0, Red:K0, Cyan:G0, Green:F0, Orange:A0, Blue:B0 (`http://www.swift.ac.uk/analysis/xrt/optical_loading.php`)

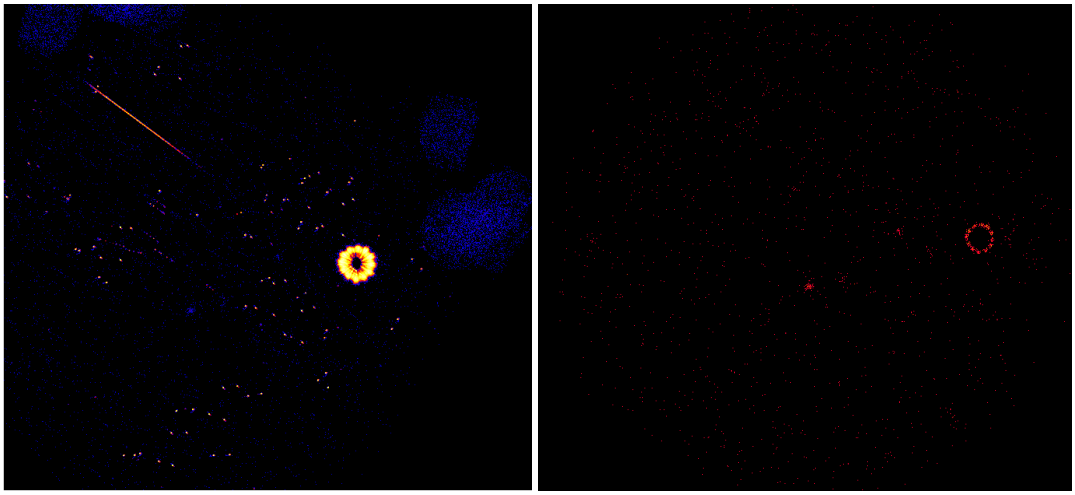

Figure 3.27.: Unfiltered and clean detector image of *Swift* observation 00037385001.

with a Digital Number (DN) in the range of 80–4095 are accepted. A DN of 80 results in a threshold magnitude of ∼ 9 mag, above which an optical source is detected and the events accepted. Figure 3.26 shows the DN over the V magnitude. This is, however, dependent on the stellar type. Figure 3.27 shows an example of optical loading. On the left is an unfiltered image compared to a clean image. Level 2 images have been calibrated and screened (Sect. 3.3.2.3). Not all of the events due to optical loading have been flagged and removed and a ring shape appears in the image. The gaps in the ring are due to the spider which holds the XRT mirrors in place. Figure 3.28 shows the same unfiltered image as in Fig. 3.27 on the left and compares it to an optical image (STScI - Digitized Sky Survey) of the same region of the sky (right). The bright star is ϵ Boötis, also named Izar, which is a binary star system. The apparent V magnitude of the brighter star is 2.39 mag. The UVOT image of the same observation has been shown in Sect. 3.3.1 (Fig. 3.11). The unfiltered X-ray image shows that the central photons have been rejected. This happens during the on board event recognition. At the edge of the PSF events are falsely recognized as X-ray events.

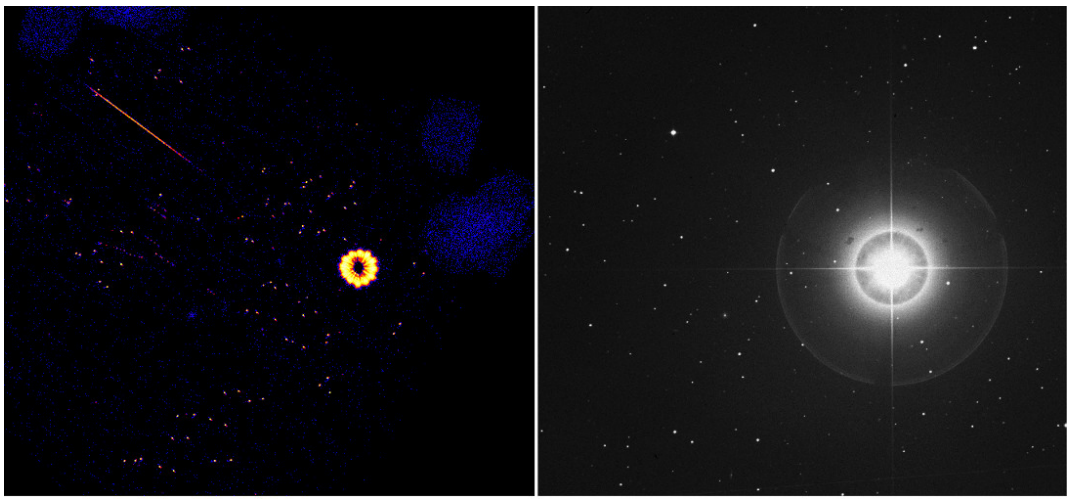

Figure 3.28.: Unfiltered detector image of *Swift* observation 00037385001 and STScI-DSS image of the same region.

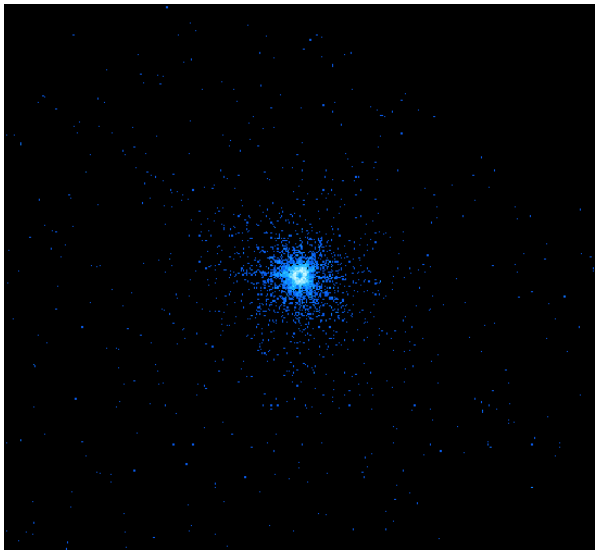

Figure 3.29.: Pile-up in the *Swift* observation 00030795002 of the TANAMI source PKS 2155−304.

3.3.3.4. Pile-Up

The problem of pile-up arises when more than one X-ray photon per pixel are detected during two read-outs. This leads to the problem that the incident photons are detected as one event. But not only the number of photons are false, the energies of the photons are added together and thus the spectral shape is affected (Ballet, 1999, Schmid et al., 2010, Schmid, 2012). Since the PSF is highest at the center this usually only occurs at the very center of a point source and can be corrected for by excluding the central pixels that are affected, during the extraction of the data. Figure 3.29 shows an example of pile-up. The spike of the source are due to the spider. The spider holds the Wolter mirrors in place by the 12 spokes. These dent the mirrors slightly, which leads to additional diffraction that causes the 12 spikes shape.

3.3.3.5. CCD instrumental Background and Damage

Satellites in space are susceptible for a number of effects, which accelerate the degradation of the instruments. Particularly CCDs are vulnerable to diverse incident particles. Passage

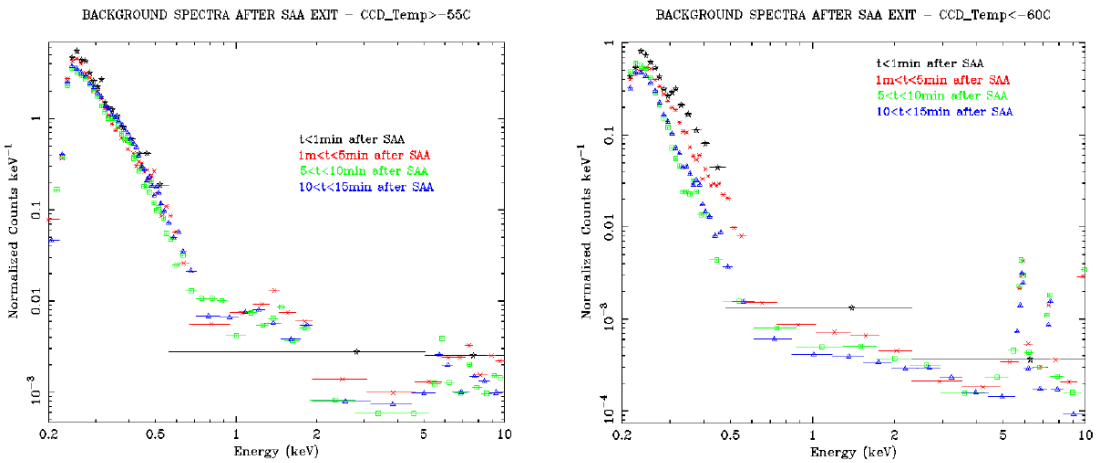

Figure 3.30.: *Swift*/XRT background spectra at increasing time intervals after exit of the SAA (Pagani et al., 2007).

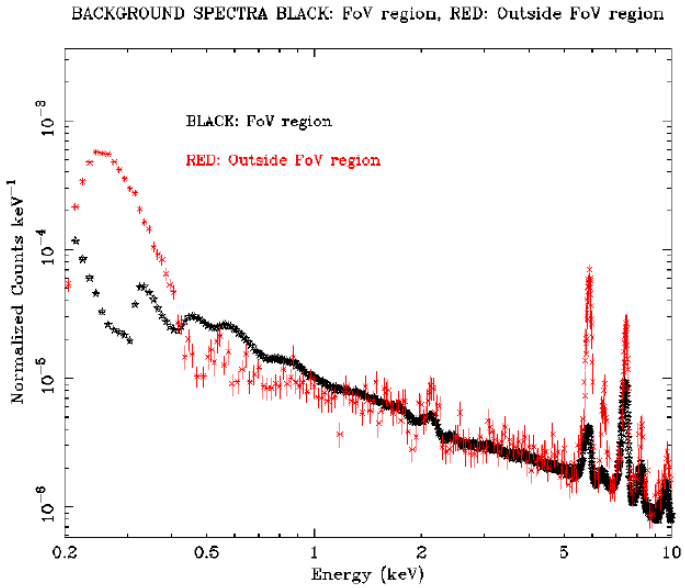

Figure 3.31.: Comparison of *Swift* XRT spectrum within FoV and outside the FoV including instrumental noise (Pagani et al., 2007).

through the South Atlantic Anomaly (SAA) leads to high incident proton fluxes. Protons can irradiate CCD detectors and lead to high instrumental background (Pagani et al., 2007). The *Swift*/XRT instrumental background can be seen in Figs. 3.30 and 3.31.
Accumulating X-ray dose leads to disruptions in the silicon-gate interface, which can be seen in an increase in the dark current. Lattice damage is also caused by energetic particles and γ-rays. High and low energy protons cause a degradation in spectral resolution, because they induce traps in the oxide layer due to displacements in the silicon lattice. This leads to changes in the Charge transfer inefficiency (CTE) and changes in ideal operating bias and a shift in voltage. Low energetic electrons cannot be distinguished from X-ray events, but can easily be deflected using magnets.
Another danger to CCDs in space are micrometeoroids. These are small particles of rock, which weigh less than a gram. Their relative velocity to a spacecraft is of the order of 10 km s^{-1} . A possible explanation for the micrometeoroid damage is the deflection on the shells of the Wolter mirror and the subsequent impact on the CCD. Another theory states

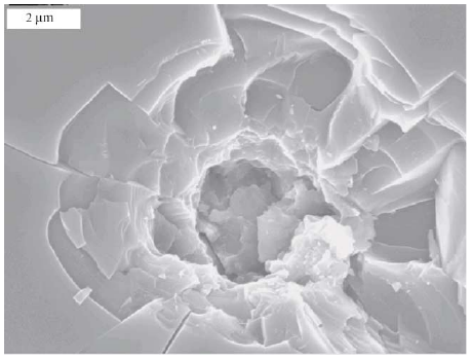

Figure 3.32.: SEM image of a crater in silicon after an impact of iron particles that have been deflected by a Wolter mirror (Meidinger et al., 2003).

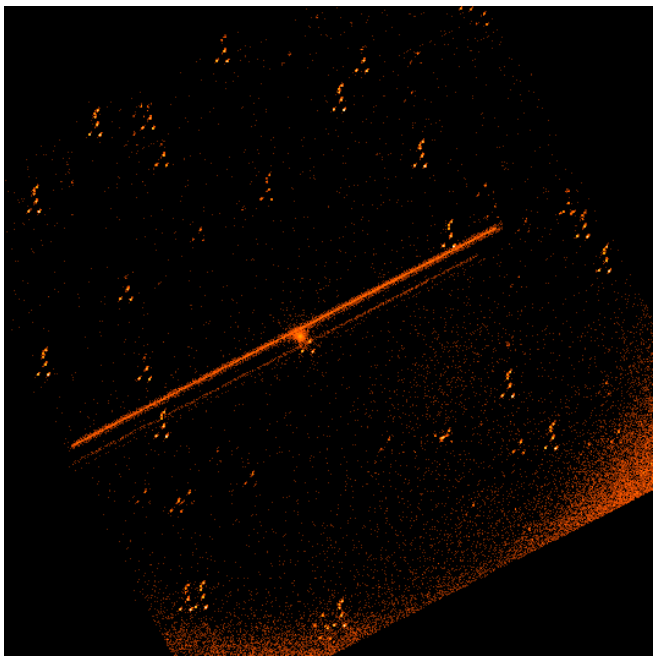

Figure 3.33.: *Swift* observation 00030138001, 2 months after the impact on the XRT CCD.

that the micrometeoroid impacts the gold mirror, which then leads to a forward ejection of gold particles that hit the CCD. A third possibility is scattering of the meteoroid through the mirrors and production of ejecta in the optical blocking filter in front of the CCD (Meidinger et al., 2003). Experiments have shown that micrometeoroids can be deflected in Wolter type I mirrors under grazing incidence and hit the surface of the CCD. Further analysis of the impact has shown that the most likely explanation is a deflection of the micrometeoroids, which may also be fragmented after the impact on the mirror. The micrometeoroids or its fragments will then hit the CCD directly, as no traces of gold have been found in the experiment (Meidinger et al., 2003).
In 2005 such an event caused the loss of a whole CCD in MOS1 on board *XMM-Newton* (Abbey et al., 2006). The *Swift* XRT CCD was hit by a micrometeoroid on 27 May 2005, which left hot columns (Fig. 3.33). This has been corrected for in the *Swift* analysis pipeline by ignoring events from the affected columns. The recurring pattern in Fig. 3.33 is due to hot pixels and the movement of the satellite.

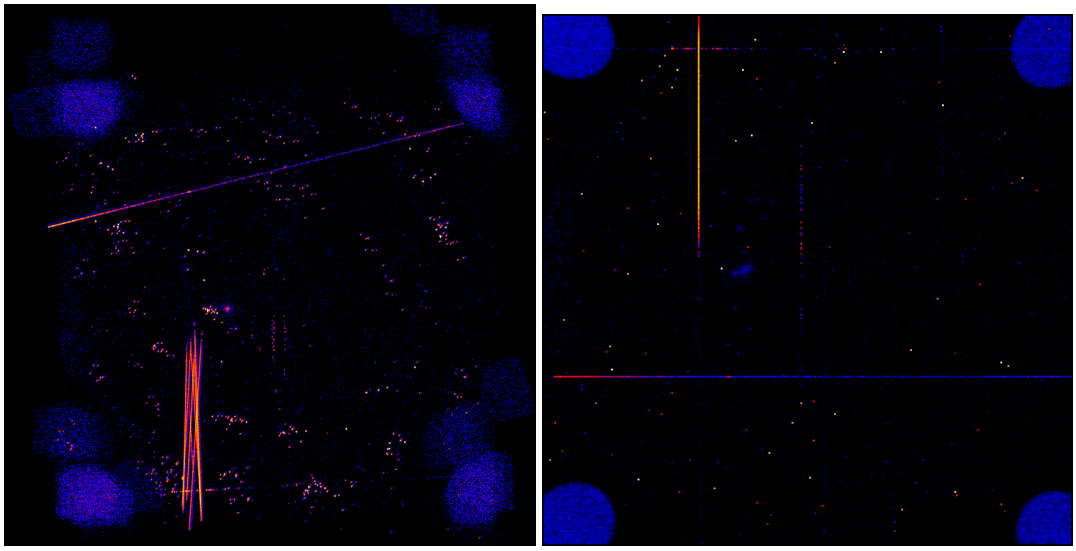

Figure 3.34.: Unfiltered Image of *Swift* observation 00038409001 in Sky coordinates (left) and in detector coordinates (right)

The unfiltered image in Fig. 3.34 in detector coordinates on the right shows a vertical hot column. This is seen as many bright streaks in the left image due to the slewing of the satellite. There is also another very faint vertical hot column in the center of the CCD. When analyzing this observations it is interesting that the hot column only appears on t=54821.8 MJD of the observation. Figure 3.35 shows the correlation of the CCD temperature to the appearance of the hot column. It seems that this column is only visible above a certain temperature of ∼−60°C. Figure 3.36 shows the dependence of the count rate to the CCD temperature. Purple data points are taken from the whole observation and blue data points are only data points within the time range, where a strong hot column was seen. A hot column originates in a hot pixel that contaminates other pixel during read out. Hot pixels are thought to be created when a cosmic ray hits a pixel (Wille, 2011, Lutz, 2001). This effectively connects the pixel to the gate, which leads to electron leakage into the pixel. The temperature dependence can be explained by a semiconducting contact between the pixel and the gate.

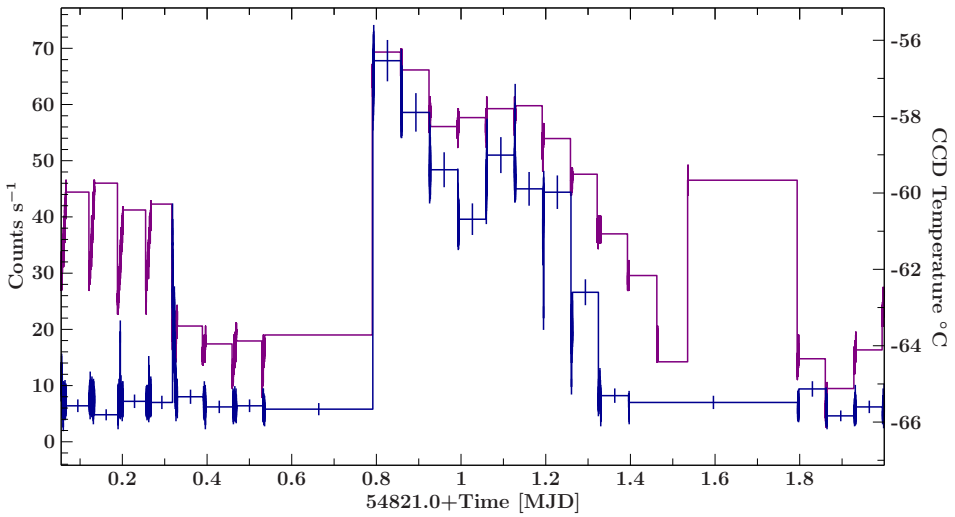

Figure 3.35.: CCD Temperature (purple) and light curve of unfiltered image (blue)

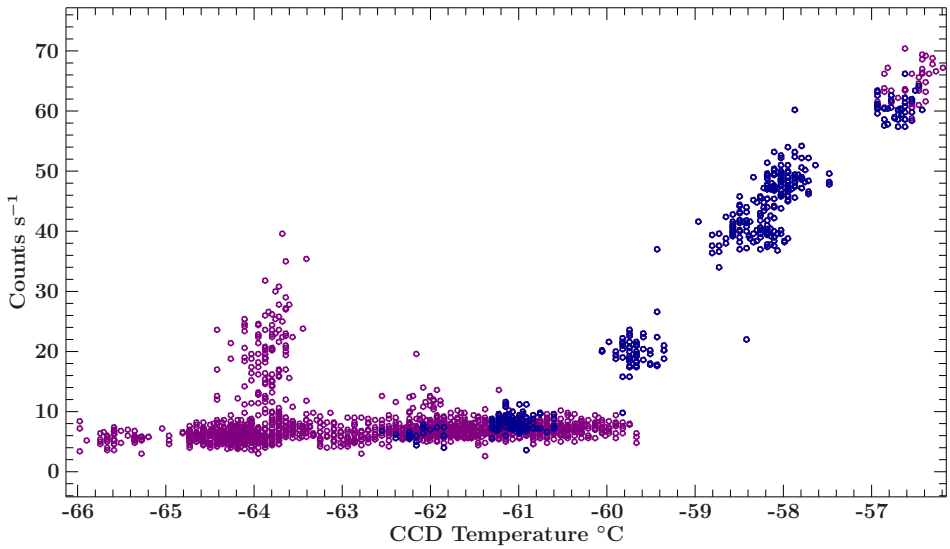

Figure 3.36.: Count rate over CCD Temperature

When the temperature of the CCD rises up to the activation energy of the semiconductor we observe high count rates due to the electron leakage. The temperature, at which the hot column appears, corresponds to a thermal energy of 18.2 meV, which is of the order of a typical band gap of doped silicon (Lutz, 2001).

3.3.4. Burst Alert Telescope

The Burst Alert Telescope (BAT) on board *Swift* is the first of the three instruments to detect a GRB and estimate its direction with an accuracy of 1-4 arcminutes. A GRB triggers an autonomous slew of the spacecraft to the burst for follow-up observations of all *Swift* instruments. From 2005 to 2013 *Swift*/BAT has detected over 700 Gamma-ray bursts (Newman, 2013b). The BAT is a coded mask detector with 52,000 pieces of lead, as well as 32,768 pieces of CdZnTe in the detector plane. In between triggers due to Gamma-ray bursts the Burst Alert Telescope is performing an all-sky hard X-ray survey with a sensitivity of ~ 2

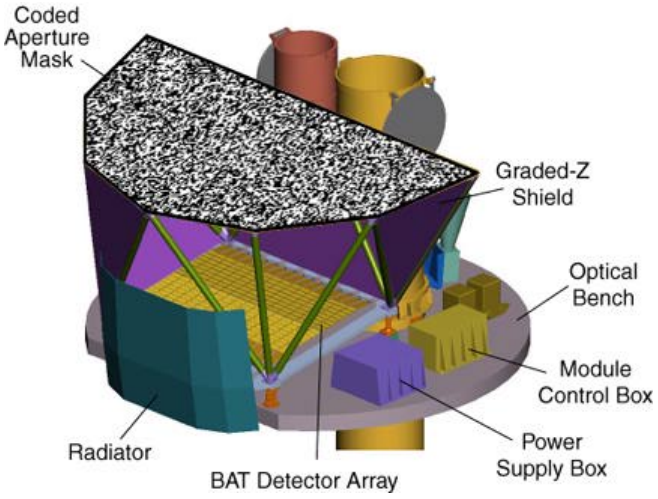

Figure 3.37.: Design of the BAT Instrument (Barthelmy et al., 2005).

mCrab which allows quick follow-up observations and studies of transient sources (Barthelmy et al., 2005).

Table 3.5.: BAT Instrument Characteristics (Barthelmy et al., 2005)

Aperture	Coded mask, random pattern, 50% open
Detecting area	5240 cm^2
Detector material	CdZnTe (CZT)
Detector operation	Photon counting
Field of view	1.4 sr (partially-coded)
Detection elements	256 modules of 128 elements/module
Detector element size	4mm × 4mm × 2mm
Telescope PSF	17 arcmin
Energy range	15-150 keV
Energy resolution	∼7 keV
Sensitivity	$\sim 10^{-8}$ erg s^{-1} cm^{-2}

In this thesis BAT data from the 58 month (Baumgartner et al., 2010, Baumgartner, 2011) and the 70 month (Baumgartner et al., 2012, Baumgartner, 2012) catalogs, which are available online, were used.

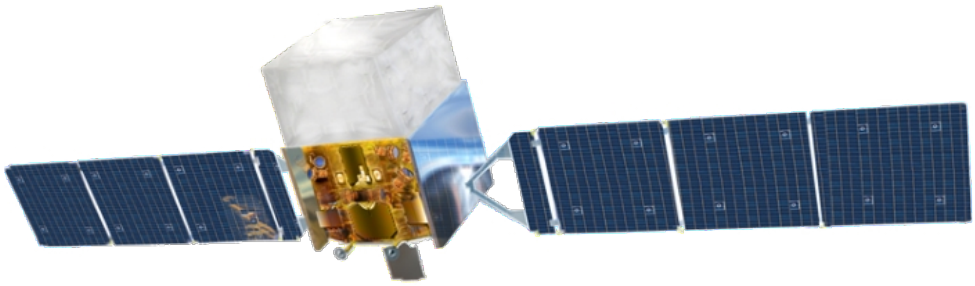

Figure 3.38.: The *Fermi Gamma-ray Space Telescope* (NASA E/PO, Sonoma State University, Aurore Simonnet)

3.4. *Fermi Gamma-ray Space Telescope*

The *Fermi* satellite was launched on 11 June 2008 by NASA. In August 2008 the name of the satellite was changed from *Gamma-ray Large Area Telescope (GLAST)* to *Fermi Gamma-ray Space Telescope*, honoring the work of Enrico Fermi. In this Section I will give a short overview of the *Fermi* satellite and the extraction of *Fermi* data, following Atwood et al. (2009), Meegan et al. (2009), Böck (2012) and Newman (2013a).
The instruments on board *Fermi* are the Large Area Telescope (LAT) and the Gamma-ray Burst Monitor (GBM). The aims of *Fermi* are to explore the most extreme environments, to search for the composition of dark matter, to explain how black holes accelerate jets, to study gamma-ray bursts, and to answer long-standing questions about various objects such as pulsars, cosmic rays and solar flares.
The Gamma-ray Burst Monitor (GBM) is designed to detect and study γ-ray bursts and transient sources. Most observations of GRBs have been performed at the energies below 1 MeV. The goal of the GBM is to study GRBs at higher energies (Meegan et al., 2009).

3.4.1. Large Area Telescope (LAT)

Fermi's primary instrument is the Large Area Telescope (LAT). It is a wide field of view high energy γ-ray pair production telescope. Table 3.6 lists its performance characteristics (Atwood et al., 2009).

Table 3.6.: *Fermi*/LAT Instrument Characteristics (Atwood et al., 2009)

Effective area	9500 cm^2
Energy range	20 MeV - 300 GeV
Energy resolution	≤6% at >10 GeV
	9%-15% at 100 MeV - 1 GeV
Angular resolution	≤0.°15 at >10 GeV
	3.°5 at 100 MeV
Field of view	2.4 sr
Timing accuracy	<10 μs
Event readout time (dead time)	26.5 μs
Point source sensitivity	3×10^{-9} erg s^{-1} cm^{-2}

Due to its wide field of view *Fermi*/LAT is able to monitor the whole sky in 3 hours. The underlying process of the *Fermi*/LAT is pair conversion. It is possible to distinguish between γ-

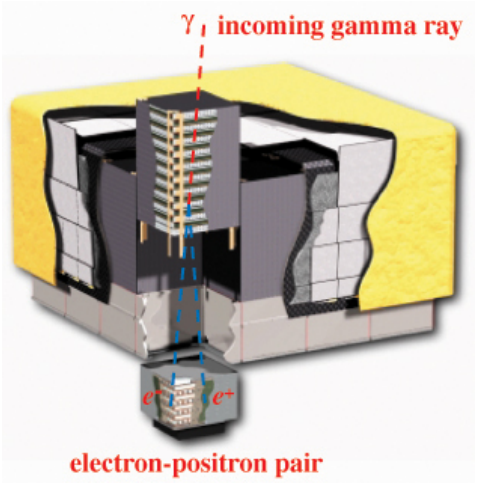

Figure 3.39.: Schematic diagram of the *Fermi*/LAT (LAT Collaboration)

rays and cosmic rays, because the flux of the latter is 5 orders of magnitude larger. Charged particles are detected in the first layer, an anticoincidence shield. This shield is used for background rejection. However, showers caused by γ-ray events can cause signal in the anticoincidence shield. Incident γ-ray photons then pass through thin layers of materials with a high atomic number, called conversion foils. The trajectories of the newly generated electron-positron pair is traced in a tracker and calorimeter. A typical γ-ray signature has no signal in the anti-coincidence shield, more than one trajectory in the tracker and an electromagnetic shower in the calorimeter. The tracking detector consists of 18 layers of silicon strip detectors and the calorimeter consists of eight layers of 12 CsI bars in each tower, read out by photodiodes. The CsI crystals are oriented perpendicular to the crystals in the following layer. Due to the segmentation in the calorimeter, it is possible to reconstruct the direction of the incident photon, as well as image the profile of the shower, which enables the rejection of background events. Figure 3.39 shows a schematic design of the LAT detector (Atwood et al., 2009). Figure 3.40 shows the Aitoff projection of the *Fermi*/LAT 3 year sky

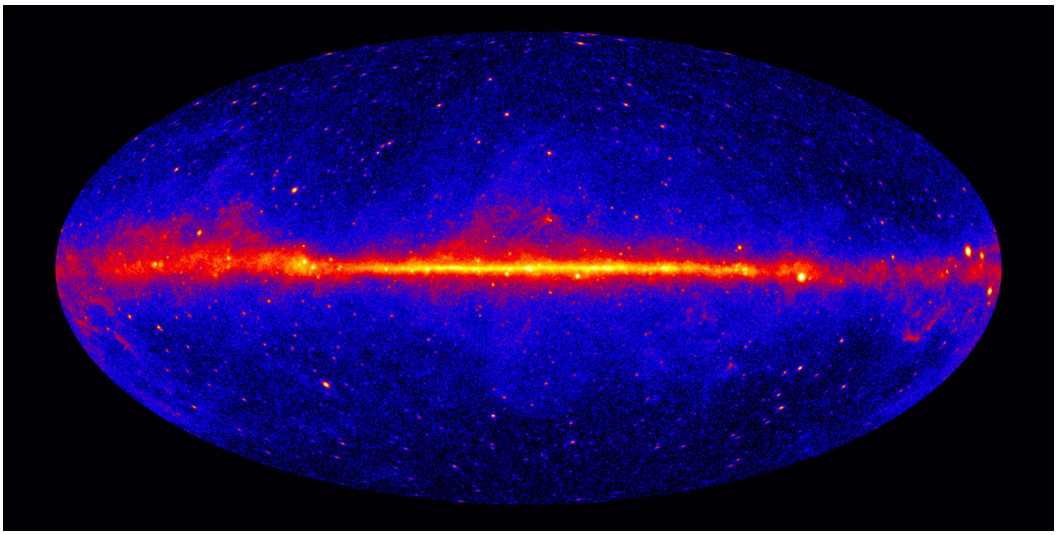

Figure 3.40.: Aitoff projection of the *Fermi*/LAT 3 year sky map (NASA/DOE/International LAT Team)

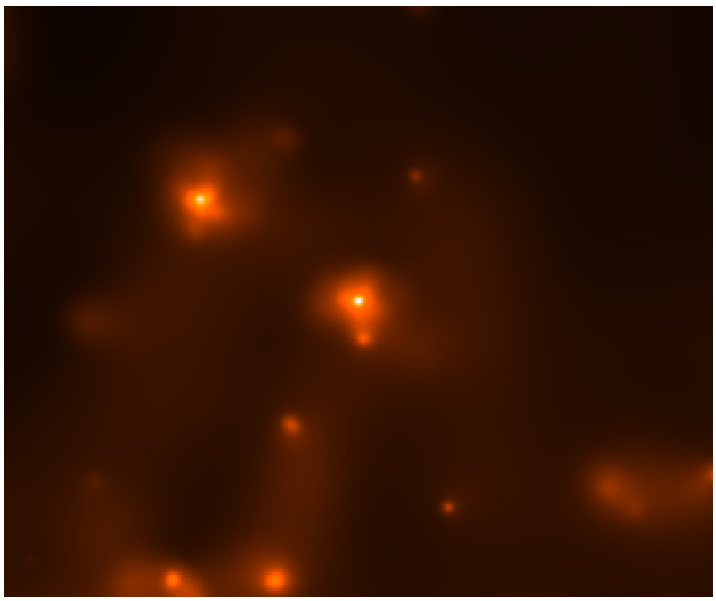

Figure 3.41.: *Fermi* image of PKS 0208–512, the image has been smoothed in CIAO using the adaptive csmooth function (Ebeling et al., 2006)

map in galactic coordinates. The Galactic plane is visible, as well as many extragalactic sources.

3.4.1.1. *Fermi*/LAT data extraction

The *Fermi*/LAT team provides the *Fermi*/LAT Science tools, which allow the extraction of *Fermi* light curves and spectra. The software is available online (`http://fermi.gsfc.nasa.gov/ssc/data/analysis`). The reduction of the data requires an event file, a spacecraft file, and a background model. *Fermi*/LAT data are extracted by applying a Maximum Likelihood method. First the data are selected and filtered in a given time range and a region of interest. This region of interest has to be big enough to include neighboring sources for background rejection but small enough to limit the computing time to a reasonable value. A source model is folded with the detector response and compared to the data. Diffuse background components are the extragalactic diffuse emission and the Galactic diffuse emission.
The maximum likelihood method is described in detail by Cash (1979). This method is used to calculate the probability of obtaining a data set under the assumption that the input model is correct. The value that is used in the *Fermi*/LAT data extraction is the test statistic (TS) value.

$$\mathrm{TS} = -2\ln(L_{\mathrm{max},0}/L_{\mathrm{max}}) \tag{3.8}$$

$L_{\mathrm{max},0}$ is the maximum likelihood of the null hypothesis, the model without the source, and L_{max} the model with the source. This TS value expresses a significance in the detection of the source. $\sqrt{\mathrm{TS}}$ roughly corresponds to a σ significance. The scripts that were used for the light curve analysis of *Fermi* data have been written by W. McConville, C. Müller and A. Schooley. The scripts for the extraction of *Fermi* spectral data have been written by T. Johnson and are available online (Johnson, 2011). The results of the extraction of *Fermi* data also allows us to create images (Fig. 3.41). The extraction of *Fermi*/LAT data is described in detail by Böck (2012).

4. Results

Data of the various instruments that have been introduced in the last Chapter were used in this master thesis to create quasi-simultaneous broadband SEDs of radio-loud AGN. In this Chapter I will present my analysis of *Swift* data, as well as the creation of broadband SEDs. These SEDs can be described by simple models, which allows us to study the radio–X-ray connection and to test the blazar sequence.

4.1. TANAMI Source Sample

The TANAMI source sample includes 84 sources. 77 of these have been observed by *Swift* between 2005 and 2012. These sources have further been sorted according to available observations and simultaneity. 53 of the observed sources were too weak or underexposed at X-ray energies. This is discussed in Sect. 4.2.1. 17 of the remaining sources did not have simultaneous or quasi-simultaneous data in all wavebands or were not detected by *Fermi*. The latter could not be used due to the lack of information about source variability (Sect. 2.4.3). The remaining 7 blazar sources can be found in Table 4.1. The classification of many sources in the TANAMI sample is not clear. Although all of them are blazars it is not always possible to easily distinguish between the subclasses.

Table 4.1.: TANAMI SED source sample

Source	NED name$^{\diamond}$	Classification	Redshift z	# SEDs
0208-512	[HB89] 0208-512	BL Lac/FSRQ$^{\blacktriangle}$	1.00$^{\blacklozenge}$	2
0332-376	2MASS J03341541-3725431	BL Lac?†	?	1
0402-362	[HB89] 0402-362	QSO$^{\bullet}$	1.42$^{\bullet}$	1
0447-439	PKS 0447-439	BL Lac†	0.11$^{\clubsuit}$	2
0521-365	ESO 362- G 021	BL Lac/FSRQ$^{\blacktriangle,\star}$	0.055$^{\spadesuit,\blacktriangle,\star}$	1
0537-441	[HB89] 0537-441	QSO?$^{\blacksquare}$ BL Lac?*	0.89$^{\blacklozenge,\star}$	3
2155-304	[HB89] 2155-304	BL Lac†	0.12$^{\blacktriangle,\dagger}$	2

$^{\blacklozenge}$ Impey & Tapia (1988) and Impey & Tapia (1990)
* Ghisellini et al. (1993)
$^{\blacktriangle}$ Donato et al. (2001)
$^{\blacksquare}$ Savage (1976) and Peterson & Bolton (1972)
$^{\bullet}$ Surdej & Swings (1981)
$^{\spadesuit}$ Ulrich (1981)
† Massaro et al. (2011) and Massaro et al. (2012)
$^{\clubsuit}$ Craig & Fruscione (1997)
$^{\diamond}$ `http://ned.ipac.caltech.edu/`

4.2. Analysis of *Swift* data

4.2.1. *Swift*/XRT flux estimates

Weak sources of the TANAMI sample cannot be fitted with sufficient statistical accuracy and could therefore not be used for SEDs. This was the case for 55 of the sources. These observations were in many cases very short observations and thus only underexposed. Some sources, however, are very faint. In such cases it is possible to estimate the flux of the observation. This has been performed for sources where the number of bins in the spectrum was 25 or below after re-binning to a minimum signal-to-noise ratio of 5. X-ray spectra with a low number of bins, below 25, have been found to have large errors on the fit parameters, usually above 15 %. For the analysis of flux estimates a typical blazar spectrum has been assumed. The N_H value was set to 2.14×10^{20} cm^{-2} and the photon index of the powerlaw was set to 1.64, which were the best fit values to the source Pictor A.
This spectrum can be simulated in the *Interactive Spectral Interpretation System* (ISIS) (Houck & Denicola, 2000, Houck, 2002, Noble & Nowak, 2008) with a high exposure. The resulting information can be used to derive flux estimates for weak sources using the background subtracted counts and the actual exposure as input values.

$$F_{obs} = F_{sim} \cdot \frac{N_{obs}}{T_{obs}} \cdot \frac{T_{sim}}{N_{sim}} \tag{4.1}$$

This gives the formula for calculating a flux estimate, F_{obs}, with the number of source counts, N, and the exposure time, T. Results of this analysis can be found in Section A.2. Assuming a photon index and an N_H value introduces an uncertainty, because photon indices of blazars vary between 1.3 and 2.8. These estimates are still useful, however, in simulating reasonable exposure times for future observations of these sources.
In addition, it is possible to calculate the Detection Significance for each source. Li & Ma (1983) give two formulas for the significance S of the detection of a source. Equation 4.2 is derived by estimating the standard deviation of the observed signal N_s and Eq. 4.3 is derived using the method of statistical hypotheses test. In both equations N_{on} corresponds to the number of counts observed from the source, N_{off} to the number of background counts and α is the ratio of on-source time to off-source time.

$$S = \frac{N_s}{\hat{\sigma}(N_s)} = \frac{N_{on} - \alpha N_{off}}{\sqrt{\alpha\,(N_{on} + N_{off})}} \tag{4.2}$$

$$S = \sqrt{-2 \ln \lambda} = \sqrt{2}\left\{ N_{on} \ln\left[\frac{1+\alpha}{\alpha}\left(\frac{N_{on}}{N_{on}+N_{off}}\right)\right] + N_{off} \ln\left[(1+\alpha)\left(\frac{N_{off}}{N_{on}+N_{off}}\right)\right]\right\}^{\frac{1}{2}} \tag{4.3}$$

These two equations have been used for the calculation of Detection Significance and can be found in Table A.1 in Section A.2 in the columns "LM (9)" and "LM (17)". Gillessen & Harney (2005) revised the problem of significance in Bayesian statistics. Their result is given in Eq. 4.4 and 4.5.

$$I_1(\omega) = \int_{\frac{\alpha}{\alpha+1}}^{\omega} P_1(\nu|N_{on};N)\, d\nu = \frac{N! \cdot \left(B_\omega\left(\frac{1}{2}+N_{on},\frac{1}{2}+N_{off}\right) - B_{\omega_{min}}\left(\frac{1}{2}+N_{on},\frac{1}{2}+N_{off}\right)\right)}{\Gamma\left(\frac{1}{2}+N_{on}\right)\Gamma\left(\frac{1}{2}+N_{off}\right) - N! \cdot B_{\omega_{min}}\left(\frac{1}{2}+N_{on},\frac{1}{2}+N_{off}\right)} \tag{4.4}$$

$$S_B = \sqrt{2} \cdot \mathrm{erf}^{-1}(I_1(\omega_{up})) \tag{4.5}$$

These equations are correct for any number of counts, whereas the Li & Ma equation deviates for the limit of low numbers. In the limit of large count numbers both papers agree. However,

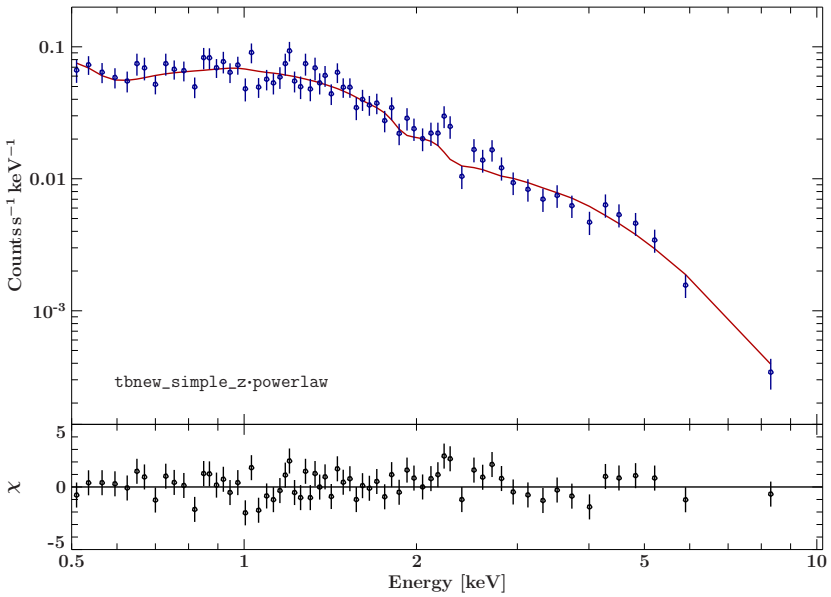

Figure 4.1.: Best fit to the *Swift*/XRT spectrum of 0537-441 of the May 2010 epoch, which had a total exposure of 18.78 ksec, with a photon index, Γ of $1.81^{+0.10}_{-0.08}$ and a $2-10$ keV flux of 2.99 ± 0.27 erg s^{-1} cm^{-2}.

the significance in Bayesian statistics can only be solved numerically. This has been done using the Mathematica script that has been provided by Gillessen & Harney (2005). The results can be found in the column labeled "Bayes". In the case of $N_{on} > 3 \cdot N_{off}$ the Mathematica script failed due to numerical problems.

4.2.2. Analysis of XRT data

In this section I will give a short overview of the data analysis of *Swift*/XRT data. After the data reduction and extraction of *Swift*/XRT data (Sect. 3.3.2.3) from Photon counting and Windowed timing mode they were processed in ISIS.
The data were re-binned to a minimal signal-to-noise ratio of 5 to ensure the validity of χ^2 statistics. A SNR of 5 ensures that each bin comprises at least 25 photons. Only data in the range of 0.5 to 10 keV were used for spectral fitting in ISIS. The lower value has been set to 0.5 keV due to an increase in instrumental background below 0.5 keV (see Sect. 3.3.3.5, Figs. 3.30, 3.31). Fit models are not fitted to photon flux but folded through the response function of the instrument and then compared to the measured data. This is described in detail by Hanke (2011). The fit model, which was used is a photoelectric absorption and a powerlaw component (Kadler et al., 2005, Krauss, 2010, Müller, 2010b).

$$F_{ph}(E) = \exp(-N_H \cdot \sigma_{ism}) \cdot C \cdot E^{-\Gamma} \tag{4.6}$$

The powerlaw component is given by

$$F(E) = S_E(1\,\mathrm{keV}) \cdot \left(\frac{E}{1\,\mathrm{keV}}\right)^{-\Gamma}, \tag{4.7}$$

where S_E is the norm, defined as the photon flux density at 1 keV, and Γ the photon index defined in Sect. 2.4. For the photoelectric absorption the `tbnew_simple_z` model by Wilms et al. (2000) was used. The fit parameters consist of the equivalent neutral hydrogen column density N_H, which is measured in atoms cm^{-2} and the redshift z. All *Swift*/XRT spectra

have been modeled as described before (Fig. 4.1). This is necessary to determine the total absorption column and the spectral index with high accuracy. It also allows to create light curves. The material in our Galaxy does not change significantly on time scales of years, thus the Galactic absorbing column remains the same. However, matter close to the source might change on short time scales. Variations in the absorbing column of $\sim 30\%$ have been seen in Centaurus A on time scales of years and less (Rivers et al., 2011, Benlloch et al., 2001). It is therefore important to determine the total absorbing column in the fit.
The results of the *Swift*/XRT analysis can be found in Table 4.2.

Table 4.2.: Fit parameters for the *Swift*/XRT data, Errors are given at 90% confidence

Source	Epoch	Exp. [ksec]	N_H [10^{22} cm^{-2}]	Γ	$F_{2-10} \times 10^{-12}$ [erg s^{-1} cm^{-2}]	χ^2	χ^2/dof
0208-512	2008/11	26.64	$0.07^{+0.19}_{-0.07}$	$1.64^{+0.13}_{-0.10}$	1.15 ± 0.12	29.47	0.74
	2009/09	41.35	$0.22^{+0.17}_{-0.15}$	1.77 ± 0.12	$1.51^{+0.17}_{-0.16}$	46.64	0.91
0332-376	2009/02	32.48	≤ 0.018	$2.32^{+0.08}_{-0.05}$	$1.80^{+0.12}_{-0.13}$	102.28	0.84
0402-362	2010/05	4.07	≤ 0.16	$1.61^{+0.08}_{-0.07}$	14.9 ± 1.2	79.98	1.25
0447-439	2009/02	10.90	$0.042^{+0.024}_{-0.023}$	$3.02^{+0.12}_{-0.10}$	$2.80^{+0.27}_{-0.26}$	109.84	0.98
	2010/03	10.71	0.018 ± 0.019	2.50 ± 0.08	8.8 ± 0.6	171.21	1.12
0521-365	2010/03	4.09	$0.016^{+0.047}_{-0.016}$	$1.63^{+0.14}_{-0.10}$	$10.4^{+1.2}_{-1.0}$	38.34	0.91
0537-441	2008/08	11.61	$0.20^{+0.14}_{-0.13}$	1.69 ± 0.10	4.5 ± 0.5	59.37	1.06
	2009/02	10.00	$0.19^{+0.22}_{-0.19}$	$1.84^{+0.19}_{-0.17}$	2.0 ± 0.4	27.08	1.18
	2010/05	18.78	$0.020^{+0.109}_{-0.020}$	$1.81^{+0.10}_{-0.08}$	2.99 ± 0.27	69.03	1.06
2155-304	2008/08	10.89	$0.009^{+0.014}_{-0.009}$	2.67 ± 0.06	28.4 ± 1.4	200.08	1.05
	2009/02	4.27	≤ 0.016	$2.53^{+0.08}_{-0.07}$	$17.9^{+1.6}_{-1.5}$	73.78	0.90

For the analysis of broadband spectra time ranges have been selected and the *Swift*/XRT observations within that time range have been summed up. For most of these added observations the spectral index could be determined with an accuracy of $\leq 10\%$, but the errors on the absorbing column are large. Table 4.1 gives Upper Limits on the absorbing column if the best fit value is zero. In these cases the Galactic value of the absorbing column was used for the broadband SEDs (Sect. 4.4.1).

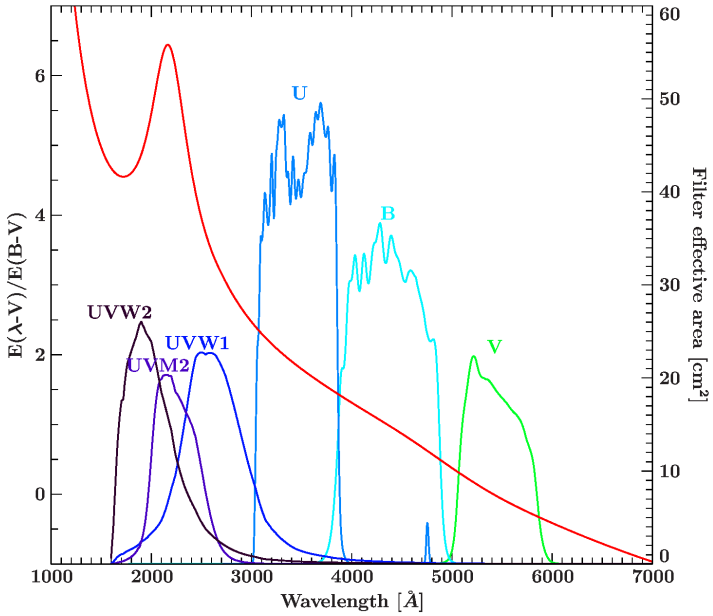

Figure 4.2.: Effective Area of the 3 optical filters (U,B,V, in blue, turquoise and green), the 3 ultraviolet filters (UVW2, UVM2, UVW1, in dark purple, purple and dark blue) and the extinction curve for $R_V = 3.1$ and $E_{B-V} = 0.5$.

4.2.3. Analysis of *Swift*/UVOT data

After the extraction of *Swift*/UVOT data (Sect. 3.3.1.1), the information of the available filters can be used in ISIS. Optical and ultraviolet fluxes are reddened due to extinction in our Galaxy, the interstellar medium (ISM). Extinction describes the absorption and scattering of radiation by matter. Photons at blue wavelengths are more heavily affected than red light, causing objects to appear redder, which led to the name "interstellar reddening". The reddened flux can be described by

$$f_{\text{reddened}} = f_{\text{unreddened}} \cdot 10^{-0.4\, E_{B-V} \cdot c}, \tag{4.8}$$

where c is the R-dependent extinction and $E_{B-V} = (B-V)_{\text{observed}} - (B-V)_{\text{intrinsic}}$ is the color excess (Fitzpatrick, 1999, Litzinger, 2011). The extinction can be described as

$$C = E_{\lambda-V} + R_V \qquad \text{with } R_V = \frac{A_V}{E_{B-V}}, \tag{4.9}$$

where A_V is the visual extinction. R_V is usually set to the averaged Galactic value 3.1 (Cardelli et al., 1989). This has been described in detail by Litzinger (2011).
Figure 4.2 shows the effective area of the UVOT filters and the extinction curve for $R_V = 3.1$ and $E_{B_V} = 0.5$. This figure has been created using a script written by E. Litzinger. The origin of the 2170 Å feature is not understood yet. Possible explanations are graphite grains, whose constants change around 2200 Å, silicate grains, or poly-cyclic aromatic hydrocarbons (PAHs) (Desert et al., 1990, Fogel & Leung, 1998, Wilms, 2012a).
For many sources the E_{B-V} value is not known. The visual extinction can be calculated from the neutral hydrogen column density N_{H} after Predehl & Schmitt (1995). Using the correlation between the visual extinction and the absorbing column,

$$\frac{N_{\text{H}}}{A_V} = 1.79 \times 10^{21}, \tag{4.10}$$

one finds that the E_{B-V} value can be calculated from the absorbing column, N_H

$$E_{B-V} = \frac{N_H}{1.79 \times 10^{21}\ R_V}. \tag{4.11}$$

The dereddening of *Swift*/UVOT data is done in ISIS using a multiplicative fit model, similar to how absorption at X-ray energies is corrected for.

4.2.4. Other Multiwavelength SED Data Analysis

In addition to the *Swift*/XRT and UVOT data, radio data from the TANAMI results as well as *Fermi*/LAT data were used. Section 3.1.2 and Sect. 3.4.1.1 discuss the data extraction for TANAMI and *Fermi* data, respectively. The TANAMI flux density information was converted to counts information and can then be read into ISIS. *Fermi* yields spectral information, which also has been converted to counts/bin to be be read into ISIS. However, *Fermi*/LAT results also include light curves. These will be discussed in the following section.

4.3. Light curve analysis

Fermi/LAT is continuously monitoring the whole sky. Information about the source flux is thus available for many of the TANAMI sources over a long time range. This information allows us to study blazar variability and create quasi-simultaneous broadband spectra. This is necessary, because blazars and quasars are very variable at all energies (Sect. 2.4). The *Fermi*/LAT light curve analysis scripts allow us to change the parameters such as the bin size or time ranges. The light curves have been extracted for fluxes in the energy range of 100 MeV to 300 GeV.
Figure 4.3 shows an example of a *Fermi* light curve, where time ranges, for which quasi-simultaneous data are available, have been marked in color. In these time ranges the flux varied little. These colors correspond to the colors that have been used in the broadband

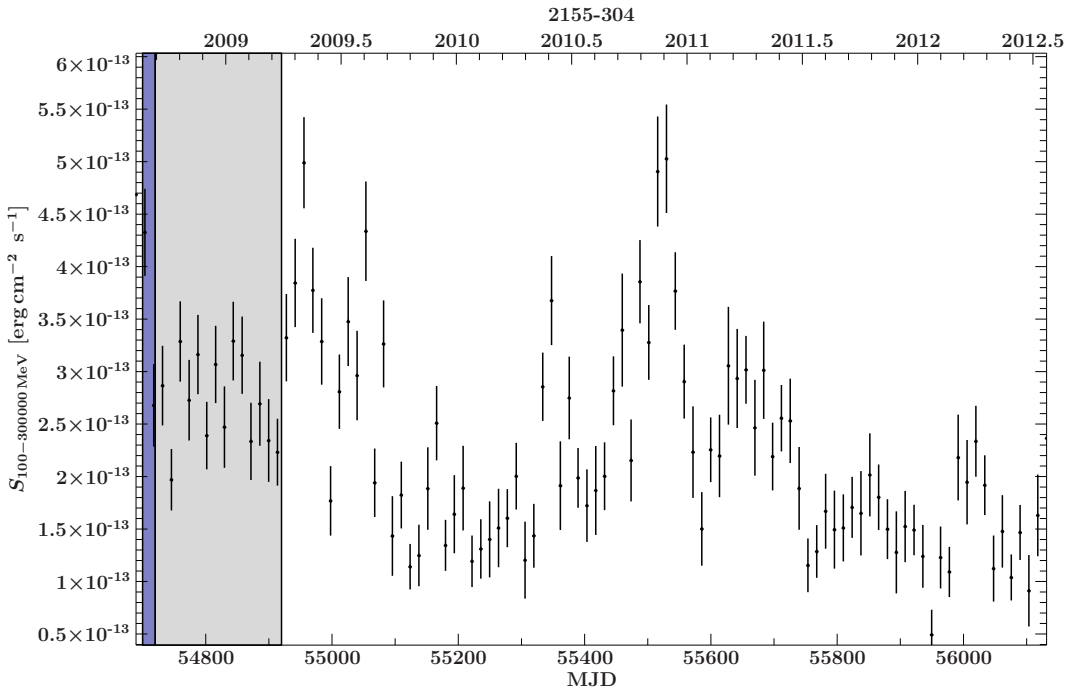

Figure 4.3.: *Fermi*/LAT light curve of PKS 2155−304 in the energy range 100 MeV - 300 GeV.

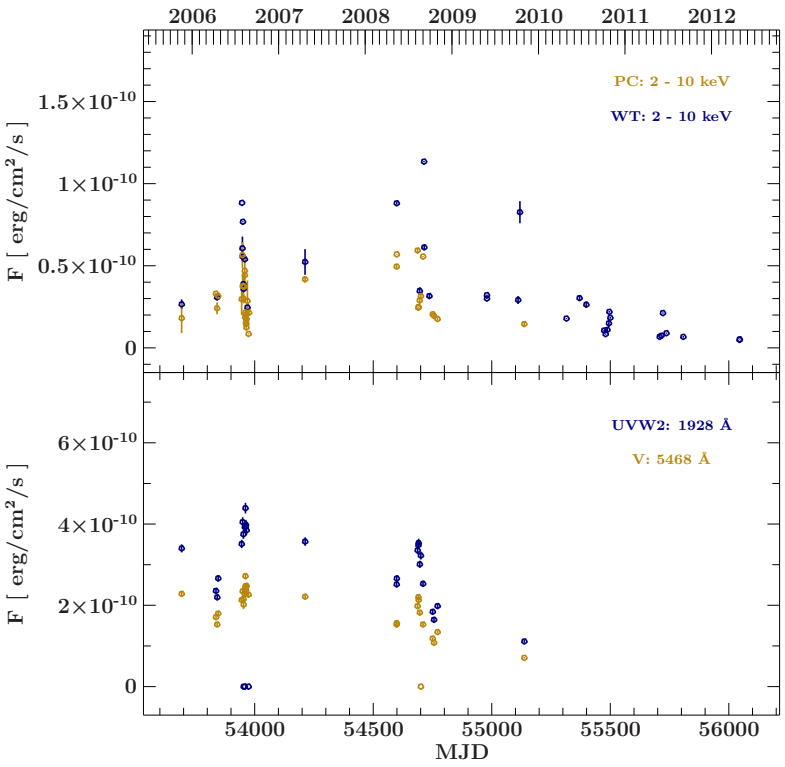

Figure 4.4.: *Swift* light curve of PKS 2155−304, the upper panel shows the XRT light curve of the 2-10 keV flux of photon counting and windowed timing modes, the lower panel shows the UVOT flux in the V and the W2 band; the error bars in both panels have been multiplied by a factor 10.

spectra (Fig. 4.6, Sect. A.4). These light curves also enable the study of correlation of flux variability at γ-ray energies in comparison to other energies. This is currently ongoing in the TANAMI collaboration. Figure 4.3 shows the *Fermi* light curve of PKS 2155−304. This can be compared to the *Swift*/XRT and UVOT light curve (Fig. 4.4). The *Fermi* light curves of the other 6 sources, which have been used for the construction of broadband spectra can be found in Sect. A.3.

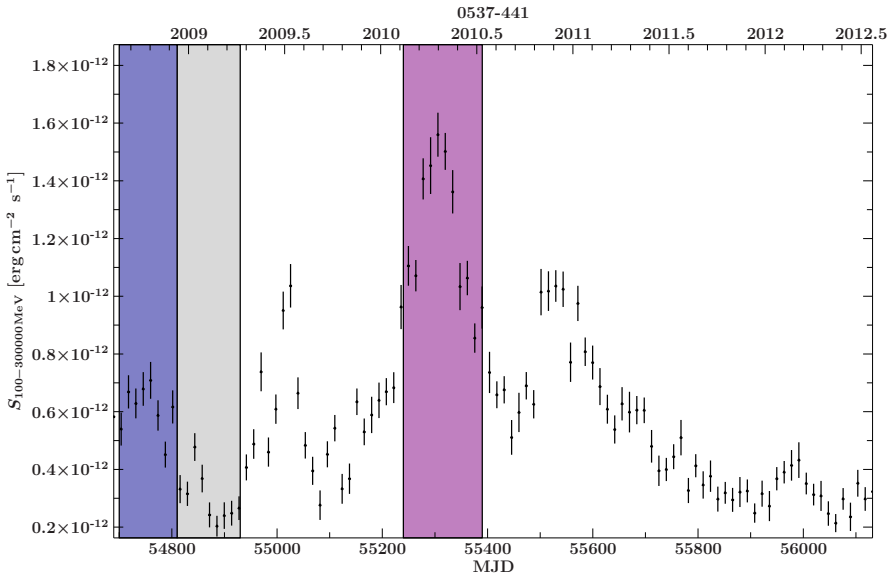

Figure 4.5.: *Fermi* light curve of PKS 0537−441.

4.4. Broadband spectral analysis

Fermi/LAT light curves give information about the source fluxes, which are used to create quasi-simultaneous broadband SEDs. *Swift*/UVOT and XRT observations in the time ranges given by the *Fermi*/LAT light curves are separately added together to increase statistics. Figure 4.5 shows the light curve for the TANAMI source PKS 0537−441. It shows strong variability, including high fluxes in 2010, which lasted for several months (purple), as well as a low flux (gray) that also lasted a few months. The intermediate flux (blue) shows some variability in the specified time range. Due to the limited temporal resolution of two weeks variability on shorter time scales cannot be included in this analysis.
The broadband SED for this source (Fig. 4.6) shows similar variability as the *Fermi*/LAT light

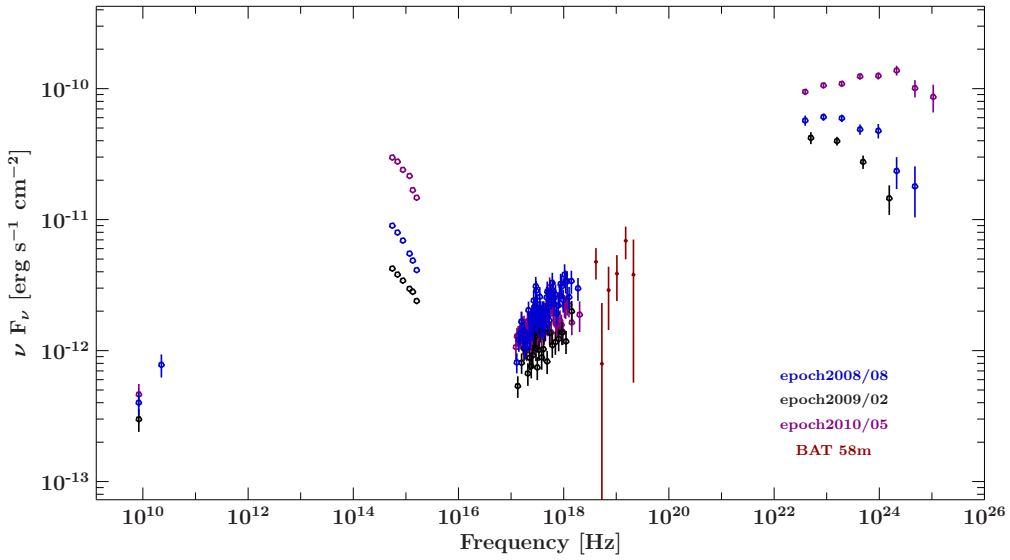

Figure 4.6.: Quasi-simultaneous SED of 0537−441, the colors correspond to the colors used in the *Fermi* light curve (Fig. 4.5), non-simultaneous BAT data from the 58 month catalog have been added.

curve. It also contains both the synchrotron and the high energy peak and high flux is seen for both. The flux at X-ray energies does not seem to vary as much as the other wavelengths do, but the fit to the X-ray data suggests a slight change in the spectral slope. The SED has not been corrected for reddening, photoelectric absorption or extragalactic background light absorption. The SEDs of the other 6 sources can be found in Sect. A.4. The colors of the individual epochs correspond to the colors of the time ranges in the *Fermi* light curves, where black SEDs are represented as gray time ranges. In the following section I will present the results of the spectral analysis. In ISIS it is possible to implement user defined models. This allows the fitting of spectral energy distributions in detector space by implementing a function for the reddening of the *Swift*/UVOT data. The data have therefore not been unfolded before the modeling. The X-ray data points have not been unabsorbed but the absorption is fitted as a part of the fit function. This approach avoids systematic uncertainties that arise when unabsorbing X-ray data and unfolding data to fit in the νF_ν space.

4.4.1. Modeling HBL SEDs with logarithmic parabolas

Broadband spectra of blazars generally consist of two broad peaks. These can be well described and parametrized by logarithmic parabolas (Giommi et al., 2012, Massaro et al., 2006, Nieppola et al., 2006). These parabolas are defined by a norm K, a photon index a, and a curvature b at a fixed energy E_1.

$$F_E = K \cdot \left(\frac{E}{E_1}\right)^{-a+b\log\left(\frac{E}{E_1}\right)} \tag{4.12}$$

$$\nu F_\nu = \log\left(\nu_p F(\nu_p)\right) - b\left[\log\left(\frac{\nu}{\nu_p}\right)\right]^2 \tag{4.13}$$

The peak frequency ν_p can be calculated from the fit parameters (Eq. 4.14).

$$\nu_p = \frac{E_p}{h} = \frac{E_1 \cdot 10^{\frac{2-a}{2b}}}{h} \tag{4.14}$$

This is described in detail by Massaro et al. (2004). The implementation of a logarithmic parabola in ISIS is done using the XSPEC *logpar* model.
Further components that are added to the fit are the photoelectric absorption component, the reddening model and a blackbody component. The photoelectric absorption has been fixed to the value, which has been determined from the analysis of *Swift*/XRT data (Sect. 4.2.2). In a few cases this absorption value was too high and did not yield a good description of the data. In this case the Galactic value has been used for the absorbing column, as well as for the calculation of the extinction. The reddening has been implemented in ISIS as a fit function, which is fixed to the averaged Galactic extinction curve and the same N_H value as the absorbing column (Sect. 4.2.3). The final model is `(logpar(1)+logpar(2)+blackbody(1))*redden(1)*tbnew_simple_z(1)` and depends on 8 free fit parameters and a total of 13 parameters.
In the optical and ultraviolet a "big blue bump" is often observed. In some cases the optical flux is affected or dominated by emission from the host galaxy or possibly the accretion disk. Generally the blackbody model fits the data relatively well, but in some cases the resulting blackbody temperatures cannot originate from a typical host galaxy. Other possible models that have been used to fit the data include a template spectrum of elliptical galaxies (Mannucci et al., 2001) and an accretion template which originates from averaged quasar spectra (Vanden Berk et al., 2001, Fig. 4.7). These template spectra have been extracted by

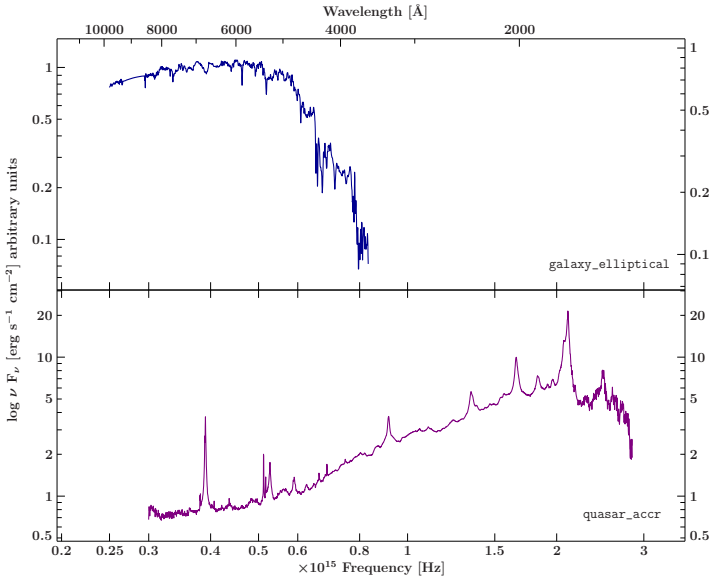

Figure 4.7.: Template spectrum of elliptical galaxies by Mannucci et al. (2001) (upper panel) and template of quasar accretion by Vanden Berk et al. (2001).

averaging over a large number of sources. Using these templates in ISIS allows to adjust their norm and shift them according to the redshift of the source.
Figure 4.8 shows the best fit to the broadband spectra of PMN J0334−3725 using two logarithmic parabolas and a blackbody component.This describes the radio, optical and X-ray data very well. However, the limited data at higher energies don't constrain the slope for the higher energy peak as well as for the synchrotron peak.
Using the template spectra of an elliptical galaxy and the quasar accretion does not describe the optical data better than a simple blackbody model (Fig. 4.9). The left fit shows the best fit, when using the elliptical galaxy template. The model has been set to a very small norm and is not visible in the spectrum.The right fit shows that the accretion template does not describe the optical data very well.

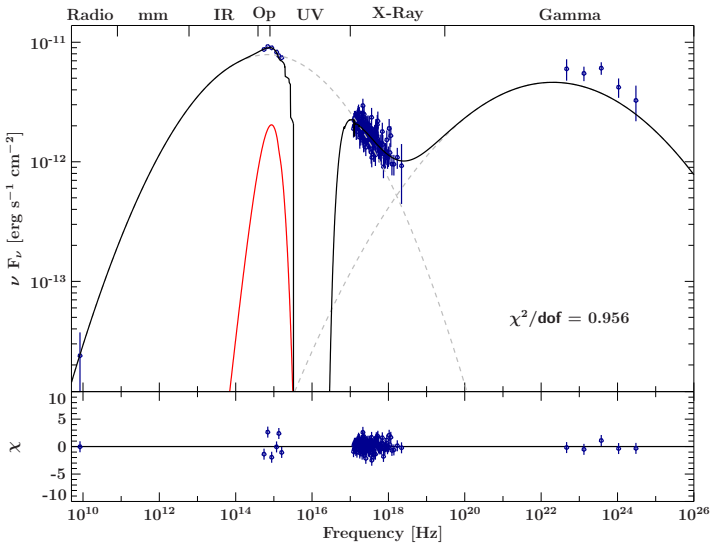

Figure 4.8.: Best fit to the SED of PMN J0334−3725, showing the complete model (black), the two log parabolas (dashed gray) and the blackbody component (red).

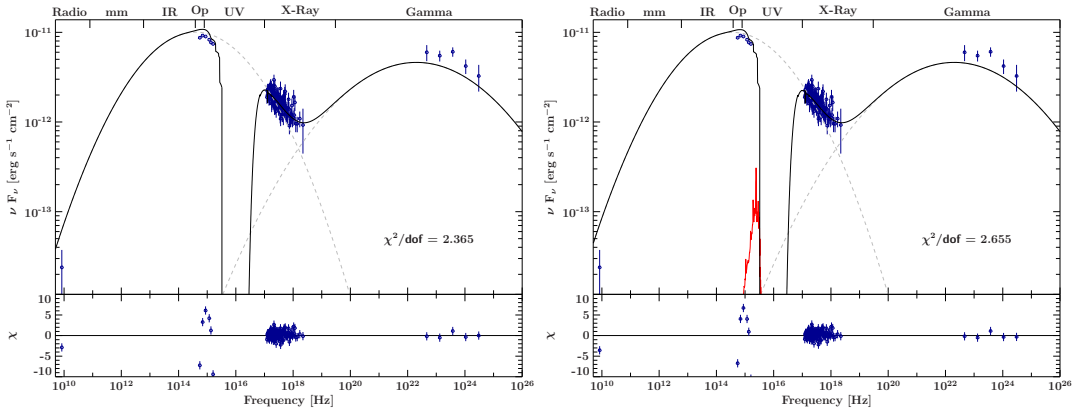

Figure 4.9.: Fit to the SED of PMN J0334−3725, using the elliptical galaxy template (left) and the accretion template (right) instead of a blackbody model.

However, with only 6 spectral data points in the optical it is not possible to distinguish very well between a blackbody and other models. For the fitting of the SEDs a simple blackbody model was used. The high energy peak can also be fitted but the errors on the peak frequency are very large, several orders of magnitudes above the value itself. Its curvature is not constrained well due to the lack of data on the falling slope. The best fit parameters can be found in Table 4.4.

4.4.2. Modeling LBL SEDs with logarithmic parabolas

HBL sources have a good coverage of the synchrotron peak with the TANAMI data in the radio band, *Swift*/UVOT at optical wavelengths and *Swift*/XRT at X-ray energies. However, the synchrotron peaks of LBL sources are only constrained through radio and optical information. This limits the accuracy of the fit (Fig. 4.10). The optical data might also be affected by emission from the host galaxy or the accretion disk. The high energy peak can also be fitted but due to a lack of data of the synchrotron peak it cannot be constrained very well.
The best fit values can be found in Table 4.3. Fitting a second peak influences the position of the peak frequency and thus also the fit parameters. The statistical errors in Table 4.4 and 4.3 are very small. The systematic errors are not included and are not easy to estimate.

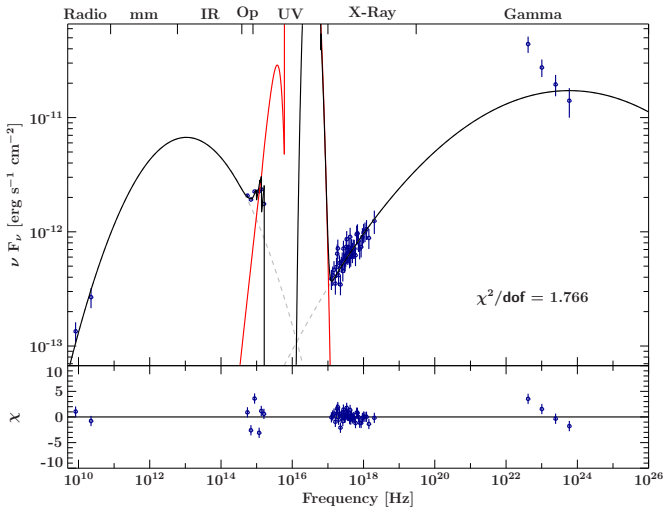

Figure 4.10.: Parabolic fit to the SED of PKS 0208−512.

Table 4.3.: Fit parameters for log parabolic fits for LBL sources, where "sync" denotes the parameters of the synchrotron peak and "HE" the parameters of the high energy peak; Errors are given at 90% confidence

Source	Epoch	N_H $[10^{22}\,cm^{-2}]$	a_{sync}	b_{sync}	kT 10^{-3} keV	a_{HE}	b_{HE}	ν_{sync} 10^{13} [Hz]	ν_{HE} [Hz]	χ^2	χ^2/dof
0208-512	2008/11	0.0184	$3.73^{+0.27}_{-0.02}$	$0.19^{+0.03}_{-0.004}$	$23.23^{+2.3}_{-13.9}$	1.59 ± 0.06	0.04 ± 0.014	1.07 ± 0.0001	5.92×10^{23}	83.01	1.77
	2009/09	0.0184	$5.5^{+0.5}_{-1.2}$	$0.36^{+0.05}_{-0.10}$	$4.45^{+8.00}_{-0.9}$	1.65 ± 0.05	0.049 ± 0.01	0.56 ± 0.001	9.67×10^{21}	82.23	1.44
0402−362	2010/05	0.00241	$4.49^{+0.73}_{-0.25}$	$0.26^{+0.07}_{-0.08}$	$27.3^{+1.3}_{-10.7}$	1.64 ± 0.05	0.063 ± 0.010	0.91 ± 0.0001	1.62×10^{21}	495.16	7.18
0521−365	2010/03	0.0159	$4.30^{+0.16}_{-0.19}$	$0.257^{+0.017}_{-0.019}$	$0.20^{+0.08}_{-0.10}$	1.69 ± 0.06	0.065 ± 0.014	1.62 ± 0.0001	5.96×10^{20}	72.24	1.57
0537-441	2008/08	0.02	3.27 ± 0.13	0.23 ± 0.02	$21.95^{+4.0}_{-10.0}$	1.52 ± 0.03	0.059 ± 0.007	1.14 ± 0.003	3.04×10^{22}	105.06	1.64
	2009/02	0.02	$3.30^{+0.23}_{-0.22}$	0.22 ± 0.04	$24.5^{+2.5}_{-15.6}$	1.50 ± 0.06	$0.063^{+0.013}_{-0.012}$	0.77 ± 0.003	2.05×10^{22}	61.79	2.21
	2010/05*	0.02	$2.68^{+0.05}_{-0.04}$	$0.148^{+0.008}_{-0.007}$	$20.90^{+4.0}_{-9.0}$	1.49 ± 0.02	0.043 ± 0.005	3.74 ± 0.016	2.04×10^{24}	957.62	12.8

*This fit has not been used for further analysis, due to high χ^2 values

Table 4.4.: Fit parameters for log parabolic fits for HBL sources, where "sync" denotes the parameters of the synchrotron peak and "HE" the parameters of the high energy peak; errors are given at 90% confidence.

Source	Epoch	N_H $[10^{22}\,cm^{-2}]$	a_{sync}	b_{sync}	kT 10^{-3} keV	a_{HE}	b_{HE}	ν_{sync} 10^{15} [Hz]	ν_{HE} [Hz]	χ^2	χ^2/dof
0332−376	2009/02	0.0154	$2.46^{+0.044}_{-0.026}$	$0.104^{+0.019}_{-0.009}$	$0.94^{+0.029}_{-0.048}$	1.55 ± 0.12	0.057 ± 0.02	0.69 ± 0.007	2.02×10^{22}	123.36	0.96
0447−439	2009/02	0.018	2.72 ± 0.04	0.217 ± 0.017	$1.50^{+0.08}_{-0.09}$	$0.19^{+1.45}_{-0.19}$	$0.16^{+0.03}_{-0.14}$	2.53 ± 0.04	1.74×10^{24}	272.87	2.31
	2010/03	0.018	$2.481^{+0.06}_{-0.03}$	$0.128^{+0.024}_{-0.010}$	$1.53^{+0.08}_{-0.07}$	$1.75^{+0.06}_{-0.19}$	$0.011^{+0.019}_{-0.009}$	1.62 ± 0.04	1.07×10^{29}	231.73	1.44
2155−304	2008/08	0.009	$2.475^{+0.008}_{-0.007}$	$0.138^{+0.004}_{-0.0030}$	1.57 ± 0.04	1.2 ± 0.4	$0.06^{+0.05}_{-0.04}$	2.19 ± 0.01	9.91×10^{24}	522.08	2.58
	2009/02	0.009	$2.487^{+0.039}_{-0.027}$	$0.130^{+0.015}_{-0.008}$	$1.47^{+0.05}_{-0.04}$	$1.70^{+0.09}_{-0.81}$	$0.016^{+0.078}_{-0.010}$	1.55 ± 0.02	5.65×10^{27}	177.47	1.89

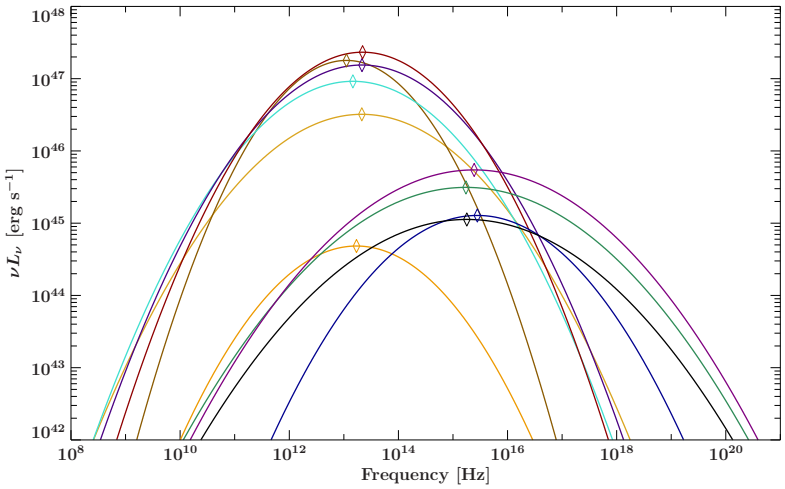

Figure 4.11.: Parabola models used in the fitting of the synchrotron peak.

4.5. Blazar Sequence

Using the fit models determined in the last section one can look at the frequency of the synchrotron peak with respect to its peak luminosity. The log parabolas of the best fit models were evaluated on a fine grid and the peak frequencies and luminosities marked in the plot by a diamond (Fig. 4.11). The fit to the source PMN J0334−3725 is not included, as the redshift for this source is unknown. The fits to the source PKS 0537−441 were also not included in the following plots due to their large χ^2 values.
Figure 4.11 shows the models used, whereas Fig. 4.12 only indicates the peak luminosities over the peak frequencies. The frequencies in both plots have been shifted according to the redshift of the source. From visual inspection a systematic error has been estimated for the synchrotron peak frequencies and luminosities in Fig. 4.12. For the luminosities, a conservative error of 50 % and for the frequencies values an error of 30 % has been assumed. The observed values do not contradict the blazar sequence, but are in better agreement with the blazar envelope that has been suggested by Meyer et al. (2012), Sect. 2.4. However,

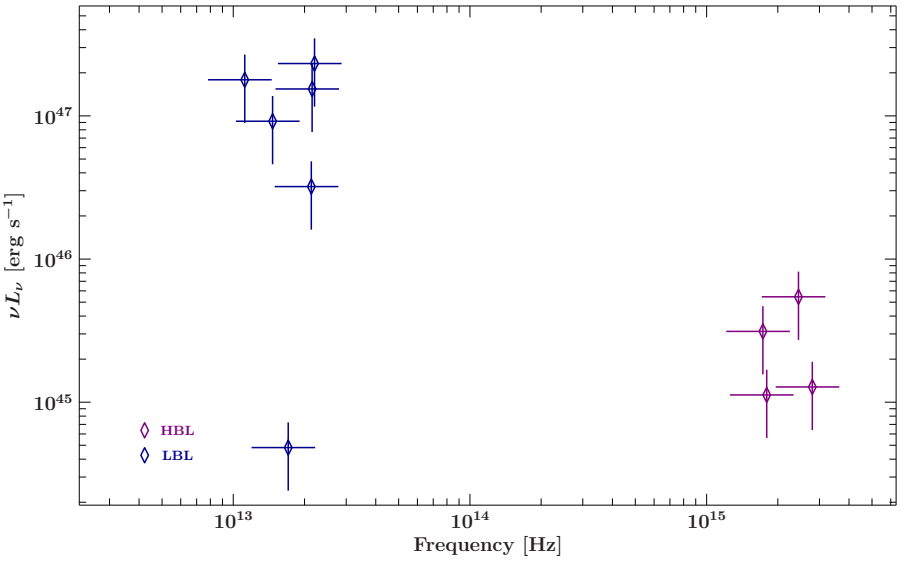

Figure 4.12.: Peak frequency over peak luminosity.

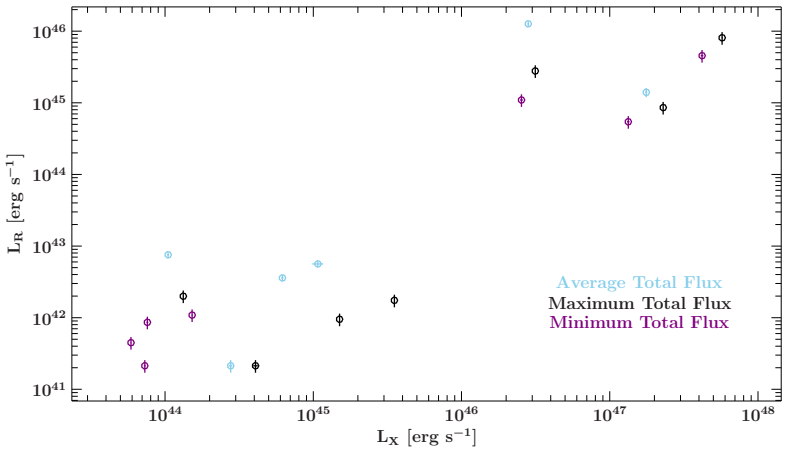

Figure 4.13.: X-ray Radio connection, showing the average, minimum and maximum luminosities for all sources.

due to the small number of sources and the uncertainties in the peak luminosities and frequencies, especially of the LBL sources, no final conclusion can be given.

4.6. X-ray - Radio connection

The luminosity information of TANAMI and *Swift* data can also be used to study the X-ray - radio connection, which has been presented in Sect. 2.6. To study this connection, sources with sufficient number of *Swift* observations were chosen. The minimum, average and maximum luminosities were calculated from the flux information. The flux has been determined from the X-ray fits, as discussed in Sect. 4.2.2. The radio luminosity has been calculated from the 8.4 GHz TANAMI data. The minimum, average and maximum flux densities have been converted to luminosities. This approach does not use simultaneous data, but rather the maximum and minimum values found. While this is a valid approach for sources with many observations in both bands, it may falsify sources with fewer. The complete information, regardless of source type can be found in Fig. 4.13. It shows the total radio luminosity over the 2 – 10 keV luminosity. The sources used in this analysis are 0402–362, 0447–439, 0537–441, 2005–489, 2149–306, and 2155–304. The different colors give the average, minimum and maximum luminosities. Fig. 4.14 shows the same X-ray-radio connection, for HBL (left) and LBL sources (right). As the lower peak in broadband SEDs is attributed to synchrotron radiation one expects to find a correlation between radio and X-ray for HBL sources, where both originate from the same process. The left plot shows HBL

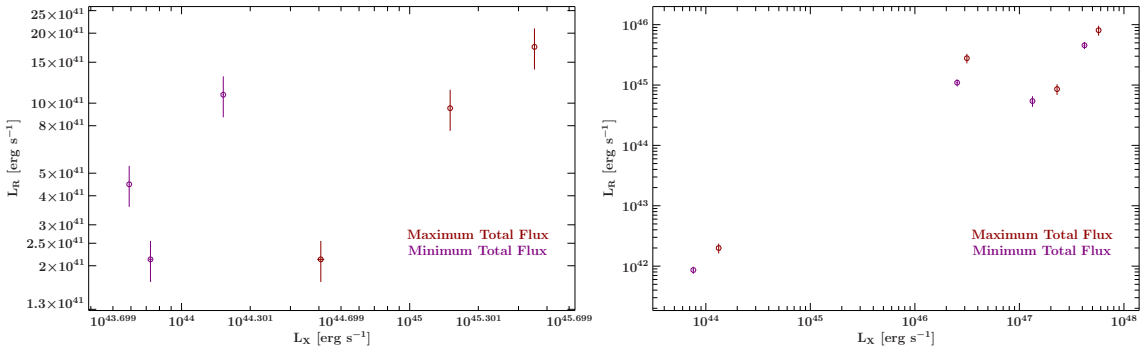

Figure 4.14.: X-ray Radio connection, for sources where $\Gamma_X > 2$ (left) and where $\Gamma_X < 2$ (right).

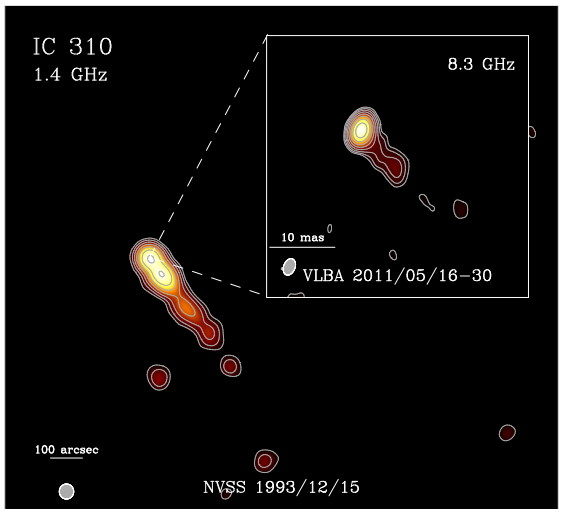

Figure 4.15.: IC 310 as seen by the NVSS in 1992 and by the VLBA in 2011 (Kadler et al., 2012).

sources, however, 3 sources are not sufficient to verify a correlation. The same is true for the LBL sources. Due to the low statistics it is not clear if there exists a correlation, but the results do not contradict a possible correlation. This is surprising, as the X-ray flux in LBL sources is usually attributed to inverse Compton scattering or hadronic processes, which might not be directly correlated with the synchrotron processes (Tavecchio et al., 2000, Celotti et al., 1997).

4.7. IC 310

IC 310 is an active galaxy on the Northern Hemisphere. Its X-ray properties have been studied as part of a collaboration with Dorit Eisenacher (Univ. Würzburg). IC 310 is part of the Perseus cluster and one of its brightest objects in the radio and X-rays (Sato et al., 2005, Kadler et al., 2012). It was classified as a head-tail radio galaxy (Sijbring & de Bruyn, 1998), based on the alignment of its jet and the pressure gradient in the intracluster medium. Recent

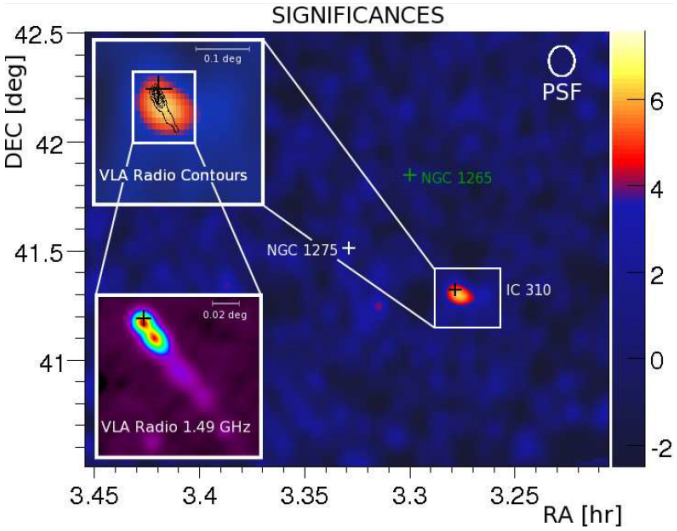

Figure 4.16.: IC 310 as seen by MAGIC, significance map showing TS values, above 250 GeV (D. Eisenacher, priv. comm.).

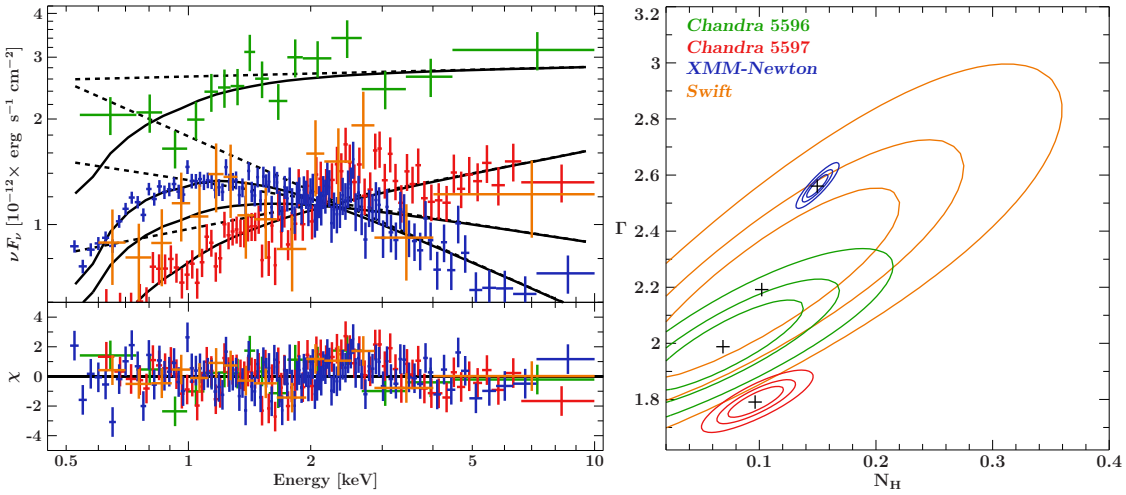

Figure 4.17.: IC 310 spectral X-ray analysis of archival data, spectrum in the νF_ν representation (left) and contour plots for the fit parameters Γ and the absorbing column.

studies of its radio properties (Fig. 4.15) have shown a one-sided jet with no detection of a counter jet (Kadler et al., 2012). Its small redshift (z=0.0189) and the detection of IC 310 at very high energies (VHE) with the MAGIC Cherenkov telescopes (Aleksić et al., 2010) lead to the conclusion that it is either the closest blazar or the brightest radio galaxy seen at TeV energies (Aleksić et al. (2013b), Eisenacher (2011), Fig. 4.16).
There exist various archival X-ray data, such as one *Swift* observation before 2012, two *Chandra* observations and one *XMM-Newton* observation. The analysis of the archival data (Fig. 4.17), which has been done in collaboration with Thomas Dauser shows variability in the X-ray spectra on time scale of years. The spectral data (left) clearly show variation in the flux between the two *Chandra* observations (green, red). The data points of the individual satellites have the same colors in the contour plot on the right. The absorbed powerlaw fit model is shown as a solid line and the powerlaw model itself in a dashed line.
Analysis of the contours of the fit parameters (right) show variations in the absorbing column and the photon index. The contours are given at 1, 2, and 3σ confidence level. The *Swift* observation used was too short to constrain the parameters very well, but the *XMM-Newton* and *Chandra* observations show a significant variation in both the photon index and the N_H value. By adding the spectral X-ray information to the MAGIC data a broadband spectrum

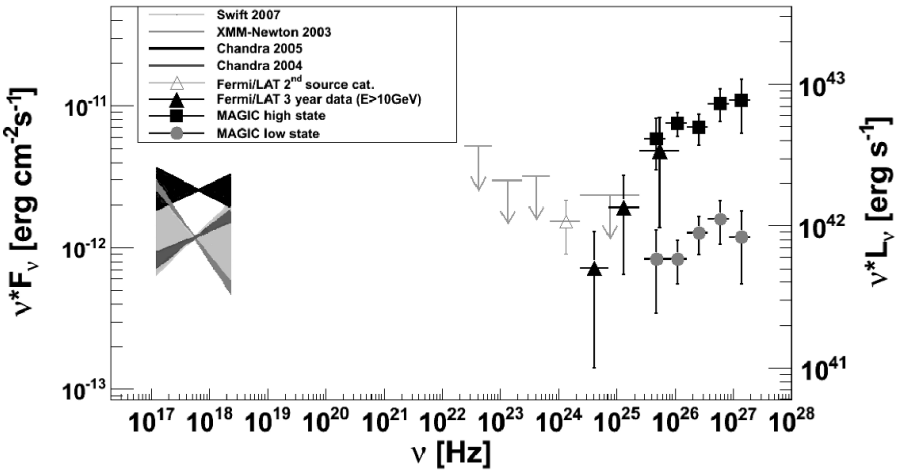

Figure 4.18.: SED of IC 310, data have not been taken simultaneous (D. Eisenacher, priv. comm.).

of IC 310 can be created (Fig. 4.18). The data are not simultaneous, however there seems to be variability in the SED, which is typical for blazars. IC 310 is too weak in the *Fermi*/LAT energy range to yield a light curve. Thus no variability information over a long time range is available. Assuming IC 310 is a blazar, the observed luminosity and peak frequency would suggest an extreme high peak BL Lac object. This analysis can further be improved by using quasi-simultaneous data, as well as a better coverage across the electromagnetic spectrum. Analysis of more recent, quasi-simultaneous data is currently ongoing.

5. Summary and Outlook

In this master thesis I have presented the results of my analysis of multiwavelength properties of active Galaxies. In this Chapter I want to give a conclusion about my work. I will also give a short outlook to future work, which will improve the results obtained here.

5.1. Summary

In my work I studied the broadband spectra of blazars. I presented the methods that were used to improve the understanding of blazars and radio-loud AGN. I used the source list of the TANAMI project to create quasi-simultaneous broadband SEDs. The TANAMI array observes at 8.4 and 22 GHz. In addition I used *Swift* data in the optical, ultraviolet and in X-rays, as well as γ-ray data by the *Fermi* satellite. Using the temporal information of the *Fermi* light curves allowed the creation of quasi-simultaneous SEDs. However, the requirements to the quality and simultaneity of the data lead to a very limited sample of only 7 sources. The SEDs of the TANAMI sources exhibited the typical two hump spectral shape. The synchrotron peak could be well described by a logarithmic parabola. The second peak, which is often attributed to inverse Compton scattering, could not be described very well, due to the lack of data at very high energies. It has been found that logarithmic parabolas with an added black body component describe the observed spectra very well. Using alternative models, such as a template spectrum of an elliptical galaxy or quasar accretion does not improve the fit. However, the limited data at optical frequencies does not allow us to distinguish very well between models.
Informations of the fits to the SEDs could be used to study the blazar sequence. Due to the limited size of the sample no definitive conclusion about a correlation can be given, but the results are in favor of a blazar envelope instead of a blazar sequence, as a source with low peak luminosity and a low peak frequency has been found. However, it cannot be excluded that a sample selection effect is seen, as the TANAMI sample, which was used for this work, is radio and γ-ray selected.
Analysis of the X-ray - radio connection for HBL sources showed the expected correlation between the luminosity at X-ray energies and at radio frequencies. A correlation also seems to be present for LBL sources, which is surprising, as it is not expected per se, that two different emission mechanisms are directly correlated. However, as only 7 sources in total have been used for this analysis no firm conclusion can be given.

5.2. Outlook

This work can be improved and expanded in several areas.

Additional data: The data quality and the quality of the fits can be improved by adding archival (quasi-simultaneous) data, which is available, to the SEDs to improve the coverage of the electromagnetic spectrum. Data at radio and infrared wavelengths (ATCA, WISE and SMARTS) are available online and will be added in the future.

Source sample: Additional data will better constrain the spectral slope and improve the peak frequency and luminosity values allowing a better study of the blazar sequence. The study of the blazar sequence and the radio-X-ray connection also necessitates a larger source sample to draw firm conclusions.

Physical models: Furthermore, it is interesting to model broadband spectra of blazars with physical models, such as Synchrotron Self-Compton or lepto-hadronic models. This will allow us to estimate physical parameters.

Extragalactic Background Light Γ-ray data by *Fermi*/LAT can be improved by adding the Extragalactic background light (EBL) de-absorption to the fit function. Recent studies have shown that the EBL absorption is seen with *Fermi*/LAT above redshifts of $z = 0.5$. (Ackermann et al., 2012).

Blazar Variability Blazar variability is not completely understood and needs further studies. Source simultaneous broadband spectra would extend our knowledge of jet emission mechanisms and blazars in general. These would take time-lags between different wavelength into account. The creation of such SEDs would necessitate a continuous monitoring of all the participating telescopes and satellites. Currently, this is not possible to achieve. However, more simultaneous multiwavelength campaigns for the studies of active galaxies are necessary gain simultaneous data which will enable us to differentiate between fit models and calculate physical parameters. These results will expand our knowledge of active galaxies.

Bibliography

Abbey T., Carpenter J., Read A., et al., 2006, In: Wilson A. (ed.) The X-ray Universe 2005, 604. ESA SP, Noordwijk, p. 943

Ackermann M., Ajello M., Allafort A., et al., 2012, Science 338, 1190

Aharonian F., Akhperjanian A.G., Bazer-Bachi A.R., et al., 2007, Astrophys. J., Lett. 664, L71

Aleksić J., Antonelli L.A., Antoranz P., et al., 2013a, The Simultaneous Low State Spectral Energy Distribution of 1ES 2344+514 from Radio to Very High Energies, in prep.

Aleksić J., Antonelli L.A., Antoranz P., et al., 2010, Astrophys. J., Lett. 723, L207

Aleksić J., Antonelli L.A., Antoranz P., et al., 2013b, Short-term and multi-band variability of the TeV-bright active nucleus of the galaxy IC 310, in prep.

Alfvén H., Herlofson N., 1950, Physical Review 78, 616

Ambrosi R.M., Abbey A.F., Hutchinson I.B., et al., 2002, Nuclear Instruments and Methods in Physics Research A 488, 543

Anada T., Dotani T., Ozaki M., Murakami H., 2008, In: Turner M.J.L., Flanagan K.A. (eds.) Space Telescopes and Instrumentation 2008: Ultraviolet to Gamma Ray. SPIE Conf. Ser. 7011

Antonucci R.R.J., 1984, Astrophys. J. 278, 499

Antonucci R.R.J., Miller J.S., 1985, Astrophys. J. 297, 621

Aschenbach B., 1985, Reports on Progress in Physics 48, 579

Atwood W.B., Abdo A.A., Ackermann M., et al., 2009, Astrophys. J. 697, 1071

Baade W., Minkowski R., 1954, Astrophys. J. 119, 206

Balbus S.A., Hawley J.F., 1991, Astrophys. J. 376, 214

Ballet J., 1999, Astron. Astrophys. Suppl. Ser. 135, 371

Barbieri C., Capaccioli M., Zambon M., 1975, Mem. Soc. Astron. Ital. 46

Barthel P., 1989a, Scientific American 260, 20

Barthel P.D., 1989b, Astrophys. J. 336, 606

Barthelmy S.D., Barbier L.M., Cummings J.R., et al., 2005, Space Sci. Rev. 120, 143

Bauer F.E., Condon J.J., Thuan T.X., Broderick J.J., 2000, ApJS 129, 547

Baumgartner W.H., 2011, The Swift-BAT 58 Month Survey, `http://heasarc.gsfc.nasa.gov/docs/swift/results/bs58mon/`

Baumgartner W.H., 2012, The Swift-BAT 70 Month Survey, `http://swift.gsfc.nasa.gov/docs/swift/results/bs70mon/`

Baumgartner W.H., Tueller J., Markwardt C., Skinner G., 2010, American Astron. Soci. 42, 675

Baumgartner W.H., Tueller J., Markwardt C.B., et al., 2012, The 70 Month Swift-BAT All-Sky Hard X-Ray Survey, submitted to ApJS

Benlloch S., Rothschild R.E., Wilms J., et al., 2001, Astron. Astrophys. 371, 858

Bennett A.S., 1962, Mem. R. Astron. Soc. 68, 163

Beringer J., Arguin J.F., Barnett R.M., et al., 2012, Phys. Rev. D 86, 010001

Bianchi S., Maiolino R., Risaliti G., 2012, Advances in Astronomy 2012

Blackburn J.K., 1995, In: Shaw R.A., Payne H.E., Hayes J.J.E. (eds.) Astronomical Data Analysis Software and Systems IV, 77. Astronomical Society of the Pacific Conference Series, p. 367

Blandford R.D., Königl A., 1979, Astrophys. J. 232, 34

Blandford R.D., Znajek R.L., 1977, MNRAS 179, 433

Blom J.J., Bennett K., Bloemen H., et al., 1995, Astron. Astrophys. 298, 33

Bloom S.D., Marscher A.P., 1993, In: Friedlander M., Gehrels N., Macomb D.J. (eds.) Compton

Gamma-Ray Observatory. AIP Conf. Ser. 280, p.578
Blumenthal G.R., Gould R.J., 1970, Reviews of Modern Physics 42, 237
Böck M., Kadler M., Tosti G., et al., 2009, In: Fermi Symposium.
Bolton J.G., Clarke M.E., Ekers R.D., 1965, Australian Journal of Physics 18, 627
Bolton J.G., Gardner F.F., Mackey M.B., 1964, Australian Journal of Physics 17, 340
Böttcher M., 2005, Astrophys. J. 621, 176
Bradt H., 2004, Astronomy Methods, Cambridge University Press, Cambridge, United Kingdom
Breeveld A.A., Curran P.A., Hoversten E.A., et al., 2010, MNRAS 406, 1687
Brinkmann W., Siebert J., Kollgaard R.I., Thomas H.C., 1996, Astron. Astrophys. 313, 356
Burrows D.N., Hill J.E., Nousek J.A., et al., 2005, Space Sci. Rev. 120, 165
Butrica A.J., (ed.) 1997, Beyond the ionosphere: fifty years of satellite communication, National Aeronautics and Space Administration, 1997. NASA history series NASA SP, Washington, D.C.
Böck M., 2012, Observations of Active Galactic Nuclei from Radio to Gamma-rays, Dissertation, FAU Erlangen
Caccianiga A., Marchã M.J.M., 2004, MNRAS 348, 937
Capalbi M., Perri M., Saija B., Tamburelli F., 2005, The SWIFT XRT DATA REDUCTION Guide
Cardelli J.A., Clayton G.C., Mathis J.S., 1989, Astrophys. J. 345, 245
Carilli C.L., Barthel P.D., 1996, Astron. Astrophys. Rev. 7, 1
Carpenter J.D., Wells A., Abbey A.F., Ambrosi R.M., 2008, Astron. Astrophys. 483, 941
Carroll S.M., Press W.H., Turner E.L., 1992, ARA&A 30, 499
Cash W., 1979, Astrophys. J. 228, 939
Celotti A., Padovani P., Ghisellini G., 1997, MNRAS 286, 415
Cheung C.C., Harris D.E., Stawarz Ł., 2007, Astrophys. J., Lett. 663, L65
Citterio O., Campano S., Conconi P., et al., 1996, In: Hoover R.B., Walker A.B. (eds.) Multilayer and Grazing Incidence X-Ray/EUV Optics III. SPIE Conf. Ser. 2805, p.56
Clarke R., 1994, Nuclear Instruments and Methods in Physics Research A 347, 529
Corbel S., Nowak M.A., Fender R.P., et al., 2003, Astron. Astrophys. 400, 1007
Craig N., Fruscione A., 1997, AJ 114, 1356
Curtis H.D., 1918, Publications of Lick Observatory 13, 9
Dermer C.D., Schlickeiser R., Mastichiadis A., 1992, Astron. Astrophys. 256, 27
Desert F.X., Boulanger F., Puget J.L., 1990, Astron. Astrophys. 237, 215
Donato D., Ghisellini G., Tagliaferri G., Fossati G., 2001, Astron. Astrophys. 375, 739
Ebeling H., White D.A., Rangarajan F.V.N., 2006, MNRAS 368, 65
Edge D.O., Shakeshaft J.R., McAdam W.B., et al., 1959, Mem. R. Astron. Soc. 68, 37
Ehle M., Breitfellner M., Gonzales Riestra R., et al., 2003, XMM-Newton User's Handbook
Eisenacher D., 2011, Teilchenbeschleunigung in der Radiogalaxie IC 310, Diploma Thesis, Univ. Würzburg
Evans P., 2012, Optical Loading, http:///www.swift.ac.uk/analysis/xrt/optical_loading.php
Falcke H., Körding E., Markoff S., 2004, Astron. Astrophys. 414, 895
Fanaroff B.L., 1974, MNRAS 166, 1P
Fath E.A., 1909, Lick Observatory Bulletin 5
Fink H.H., Schmitt J.H.M.M., Harnden, Jr. F.R., 1988, Astron. Astrophys. 193, 345
Finke J.D., Dermer C.D., Böttcher M., 2008, Astrophys. J. 686, 181
Fitzpatrick E.L., 1999, Publ. Astron. Soc. Pac. 111, 63
Fleishman G.D., Bietenholz M.F., 2007, MNRAS 376, 625
Fogel M.E., Leung C.M., 1998, Astrophys. J. 501, 175
Forman W., Jones C., Cominsky L., et al., 2012, VizieR Online Data Catalog 9004

Fossati G., Maraschi L., Celotti A., et al., 1998, MNRAS 299, 433
Fraser G.W., Abbey A.F., Holland A., et al., 1994, Nuclear Instruments and Methods in Physics Research A 350, 368
Freedman W.L., Madore B.F., Scowcroft V., et al., 2012, Astrophys. J. 758, 24
Friedman H., Lichtman S.W., Byram E.T., 1951, Physical Review 83, 1025
Fumagalli M., Furniss A., O'Meara J.M., et al., 2012, Astron. Astrophys. 545, A68
Gallo E., Fender R.P., Pooley G.G., 2003, MNRAS 344, 60
Gehrels N., Chincarini G., Giommi P., et al., 2004, Astrophys. J. 611, 1005
Ghisellini G., 2009, Mem. Soc. Astron. Ital. 80, 201
Ghisellini G., Celotti A., Fossati G., et al., 1998, MNRAS 301, 451
Ghisellini G., Madau P., 1996, MNRAS 280, 67
Ghisellini G., Maraschi L., Treves A., 1985, Astron. Astrophys. 146, 204
Ghisellini G., Padovani P., Celotti A., Maraschi L., 1993, Astrophys. J. 407, 65
Ghisellini G., Tavecchio F., 2008, MNRAS 387, 1669
Ghisellini G., Tavecchio F., Chiaberge M., 2005, Astron. Astrophys. 432, 401
Giacconi R., Gursky H., Paolini F.R., Rossi B.B., 1962, Physical Review Letters 9, 439
Gillessen S., Harney H.L., 2005, Astron. Astrophys. 430, 355
Ginzburg V.L., Syrovatskii S.I., 1965, ARA&A 3, 297
Giommi P., Polenta G., Lähteenmäki A., et al., 2012, Astron. Astrophys. 541, A160
Godet O., Beardmore A.P., Abbey A.F., et al., 2009, Astron. Astrophys. 494, 775
Godet O., Beardmore A.P., Abbey A.F., et al., 2007, In: UV, X-Ray, and Gamma-Ray Space Instrumentation for Astronomy XV. SPIE Conf.Ser. 6686
Griffiths R.E., Briel U., Chaisson L., Tapia S., 1979, Astrophys. J. 234, 810
Hall D., Holland A., Turner M., 2008, In: High Energy, Optical, and Infrared Detectors for Astronomy III. SPIE Conf. Ser. 7021
Hanke M., 2011, Probing the Environment of Accreting Compact Objects, Dissertation, FAU Erlangen
Hazard C., Mackey M.B., Shimmins A.J., 1963, Nature 197, 1037
Heinz S., Sunyaev R.A., 2003, MNRAS 343, L59
Hill J.E., Burrows D.N., Nousek J.A., et al., 2004, In: Flanagan K.A., Siegmund O.H.W. (eds.) X-Ray and Gamma-Ray Instrumentation for Astronomy XIII. SPIE Conf. Ser. 5165, p.217
Hoffmeister C., 1929, Astronomische Nachrichten 236, 233
Holland A.D., Turner M.J., Abbey A.F., Pool P.J., 1996, In: Siegmund O.H., Gummin M.A. (eds.) EUV, X-Ray, and Gamma-Ray Instrumentation for Astronomy VII. SPIE Conf. Ser. 2808, p.414
Holland S., 2010, The Swift Technical Handbook, http://swift.gsfc.nasa.gov/docs/swift/proposals/tech_appd
Houck J.C., 2002, In: Branduardi-Raymont G. (ed.) High Resolution X-ray Spectroscopy with XMM-Newton and Chandra.
Houck J.C., Denicola L.A., 2000, In: Manset N., Veillet C., Crabtree D. (eds.) Astronomical Data Analysis Software and Systems IX, 216. Astronomical Society of the Pacific Conference Series, p. 591
Hoyle F., Fowler W.A., 1963, Nature 197, 533
Impey C.D., Tapia S., 1988, Astrophys. J. 333, 666
Impey C.D., Tapia S., 1990, Astrophys. J. 354, 124
Irby B.K., 2012, HEASoft, http://heasarc.gsfc.nasa.gov/lheasoft/
Jagoda N., Austin G., Mickiewicz S., Goddard R., 1972, In: Nuclear Science Symposium and 3rd Nuclear Power Systems Symposium. IEEE Transactions on Nuclear Science, 19, p. 579
Jannuzi B.T., Smith P.S., Elston R., 1993, ApJS 85, 265
Jannuzi B.T., Smith P.S., Elston R., 1994, Astrophys. J. 428, 130
Johnson T., 2011, Produce spectral plots of LAT sources, http://fermi.gsfc.nasa.gov/

ssc/data/analysis/user/
Jones T.W., 1988, In: Kafatos M. (ed.) Supermassive Black Holes,Third George Mason Astrophysics Workshop., p.59
Joye W.A., Mandel E., 2003, In: Payne H.E., Jedrzejewski R.I., Hook R.N. (eds.) Astronomical Data Analysis Software and Systems XII, 295. Astronomical Society of the Pacific Conference Series, p. 489
Kadler M., 2005, Compact Radio Cores in AGN: The X-Ray Connecction, Dissertation, Univ. Bonn
Kadler M., 2010, The TANAMI program, http://pulsar.sternwarte.uni-erlangen.de/tanami/
Kadler M., Eisenacher D., Ros E., et al., 2012, Astron. Astrophys. 538, L1
Kadler M., Kerp J., Ros E., Zensus J.A., 2005, Astronomische Nachrichten 326, 545
Kalberla P.M.W., Burton W.B., Hartmann D., et al., 2005, Astron. Astrophys. 440, 775
Kellermann K.I., Lister M.L., Homan D.C., et al., 2003, In: Takalo L.O., Valtaoja E. (eds.) High Energy Blazar Astronomy. ASP Conf. Ser. 299
Kembhavi A.K., Narlika J.V., 1999, Quasars and Active Galactic Nuclei, Cambridge University Press, Cambridge, United Kingdom
Kennea J.A., Burrows D.N., Wells A., et al., 2005a, In: Siegmund O.H.W. (ed.) UV, X-Ray, and Gamma-Ray Space Instrumentation for Astronomy XIV. SPIE Conf. Ser. 5898, p.341
Kennea J.A., Burrows D.N., Wells A., et al., 2005b, In: Siegmund O.H.W. (ed.) UV, X-Ray, and Gamma-Ray Space Instrumentation for Astronomy XIV. SPIE Conf. Ser. 5898, p.329
Krauss F., 2010, *Swift* Observations of TANAMI Counterparts, Bachelor Thesis, FAU Erlangen
Krolik J.H., 1999, Active Galactic Nuclei, Princeton University Press, Princeton, New Jersey, USA
Kuehr H., Witzel A., Pauliny-Toth I.I.K., Nauber U., 1981, Astron. Astrophys. Suppl. Ser. 45, 367
Laing R.A., Bridle A.H., 1987, MNRAS 228, 557
Landt H., 2012, MNRAS 423, L84
Lasota J.P., Abramowicz M.A., Chen X., et al., 1996, Astrophys. J. 462, 142
Li T.P., Ma Y.Q., 1983, Astrophys. J. 272, 317
Lister M.L., Cohen M.H., Homan D.C., et al., 2009, AJ 138, 1874
Lister M.L., Homan D.C., 2005, AJ 130, 1389
Litzinger E., 2011, Observations of Compact Objects , Diploma Thesis, FAU Erlangen
Longair M.S., 2011, High Energy Astrophysics, Cambridge University Press, Cambridge, United Kingdom
Lumb D.H., Holland A.D., 1988a, IEEE Transactions on Nuclear Science 35, 534
Lumb D.H., Holland A.D., 1988b, Nuclear Instruments and Methods in Physics Research A 273, 696
Lutz G., 2001, Semiconductor Radiation Detectors: Device Physics, Springer, Berlin, Heidelberg
Lyutikov M., Lister M., 2010, Astrophys. J. 722, 197
Mannheim K., 1993a, Phys. Rev. D 48, 2408
Mannheim K., 1993b, Astron. Astrophys. 269, 67
Mannucci F., Basile F., Poggianti B.M., et al., 2001, MNRAS 326, 745
Maraschi L., Foschini L., Ghisellini G., et al., 2008, MNRAS 391, 1981
Maraschi L., Ghisellini G., Celotti A., 1992, Astrophys. J., Lett. 397, 5
Marscher A.P., Gear W.K., 1985, Astrophys. J. 298, 114
Massaro E., Giommi P., Leto C., et al., 2012, The Roma BZCAT Multi-frequency Catalogue of Blazars, http://www.asdc.asi.it/bzcat/
Massaro E., Giommi P., Leto C., et al., 2011, Multifrequency Catalogue of Blazars (3rd Edition), ARACNE Editrice, Rome, Italy,

Massaro E., Perri M., Giommi P., Nesci R., 2004, Astron. Astrophys. 413, 489
Massaro E., Tramacere A., Perri M., et al., 2006, Astron. Astrophys. 448, 861
Mastichiadis A., Kirk J.G., 1997, Astron. Astrophys. 320, 19
Meegan C., Lichti G., Bhat P.N., et al., 2009, Astrophys. J. 702, 791
Meidinger N., Aschenbach B., Braeuninger H.W., et al., 2003, In: Truemper J.E., Tananbaum H.D. (eds.) X-Ray and Gamma-Ray Telescopes and Instruments for Astronomy. SPIE Conf. Ser. 4851, p.243
Meier D., 2011, Jet Production in Accreting Black Hole Systems, Talk at Winchester Black Hole Workshop, Presentation available online http://www.black-hole.eu/media/bhworkshop11/Talks/Tuesday/meier.pdf
Merloni A., Heinz S., di Matteo T., 2003, MNRAS 345, 1057
Meyer E.T., Fossati G., Georganopoulos M., Lister M.L., 2011, Astrophys. J. 740, 98
Meyer E.T., Fossati G., Georganopoulos M., Lister M.L., 2012, In: 2012 Fermi & Jansky.
Moretti A., Campana S., Capalbi M., et al., 2006, In: Holt S.S., Gehrels N., Nousek J.A. (eds.) Gamma-Ray Bursts in the Swift Era, 836. Am. Ins. Ph. Conf. Ser., p.676
Müller C., 2010a, High resolution VLBI observations of Centaurus A, Diploma Thesis, FAU Erlangen
Müller C., Böck M., Wilms J., et al., 2012, In: Fermi & Jansky 2012.
Müller C., Kadler M., Ojha R., et al., 2011, Astron. Astrophys. 530, L11
Müller M., 2010b, *Swift* Observations of TANAMI Sources, Bachelor Thesis, FAU Erlangen
Newman P., 2013a, Fermi Gamma-ray Space Telescope, http://fermi.gsfc.nasa.gov/
Newman P., 2013b, Swift GRB Table and Lookup, http://heasarc.nasa.gov/docs/swift/archive/grb_table/
Nieppola E., Tornikoski M., Valtaoja E., 2006, Astron. Astrophys. 445, 441
Noble M.S., Nowak M.A., 2008, Publ. Astron. Soc. Pac. 120, 821
Nolan P.L., Abdo A.A., Ackermann M., et al., 2012, ApJS 199, 31
Ojha R., Kadler M., Böck M., et al., 2010a, Astron. Astrophys. 519, A45
Ojha R., Kadler M., Boeck M., et al., 2010b, In: Fermi meets Jansky - AGN in Radio and Gamma-Rays.
Osborne J.P., Beardmore A.P., Godet O., et al., 2005, In: Siegmund O.H.W. (ed.) UV, X-Ray, and Gamma-Ray Space Instrumentation for Astronomy XIV. SPIE Conf. Ser. 5898, p.352
Owens A., Bayliss S.C., Durham P.J., et al., 1996, Astrophys. J. 468, 451
Owens A., Denby M., Wells A., et al., 1997, Astrophys. J. 476, 924
Padovani P., Giommi P., 1995, MNRAS 277, 1477
Pagani C., Morris D.C., Racusin J., et al., 2007, In: UV, X-Ray, and Gamma-Ray Space Instrumentation for Astronomy XV. SPIE Conf. Ser. 6686
Paturel G., Dubois P., Petit C., Woelfel F., 2002, LEDA, 0 (2002) 0
Penrose R., 1969, Nuovo Cimento Rivista Serie 1, 252
Perlman E.S., Padovani P., Giommi P., et al., 1998, AJ 115, 1253
Perlman E.S., Stocke J.T., 1994, AJ 108, 56
Peterson B.A., Bolton J.G., 1972, Astrophys. J., Lett. 10, 105
Peterson B.A., Wright A.E., Jauncey D.L., Condon J.J., 1979, Astrophys. J. 232, 400
Peterson B.M., 1997, An Introduction to Active Galactic Nuclei, Cambridge University Press
Poole T.S., Breeveld A.A., Page M.J., et al., 2008, MNRAS 383, 627
Predehl P., Schmitt J.H.M.M., 1995, Astron. Astrophys. 293, 889
Price R.M., Milne D.K., 1965, Australian Journal of Physics 18, 329
Prigozhin G.Y., Kissel S.E., Bautz M.W., et al., 2000, In: Proc. SPIE, 4012. Conf. Ser., p.720
Pringle J.E., 1981, ARA&A 19, 137
Rashed r., 1990, The University of Chicago Press 81, 464
Raue M., Behera B., Charbonnier A., et al., 2009, The Astronomer's Telegram 2350, 1

Rector T.A., Gabuzda D.C., Stocke J.T., 2003, AJ 125, 1060
Reynolds S.P., 1982, Astrophys. J. 256, 13
Rivers E., Markowitz A., Rothschild R., 2011, Astrophys. J., Lett. 742, L29
Romero G.E., Surpi G., Vucetich H., 1995, Astron. Astrophys. 301, 641
Roming P.W.A., Kennedy T.E., Mason K.O., et al., 2005, Space Sci. Rev. 120, 95
Rybicki G.B., Lightman A.P., 1979, Radiative processes in astrophysics, Wiley-VCH
Sambruna R.M., Maraschi L., Urry C.M., 1996, Astrophys. J. 463, 444
Sato K., Furusho T., Yamasaki N.Y., et al., 2005, Publ. Astron. Soc. Jpn. 57
Savage A., 1976, MNRAS 174, 259
Scarpa R., Falomo R., 1997, Astron. Astrophys. 325, 109
Scheuer P.A.G., Readhead A.C.S., 1979, Nature 277, 182
Schmid C., 2012, X-ray Telescopes in the Digital Lab: Instrument Performance Simulations, Dissertation, FAU Erlangen
Schmid C., Martin M., Wilms J., et al., 2010, X-ray Astronomy 2009; Present Status, Multi-Wavelength Approach and Future Perspectives 1248, 591
Schmidt M., 1963, Nature 197, 1040
Schwartz D.A., Marshall H.L., Lovell J.E.J., et al., 2000, Astrophys. J., Lett. 540, L69
Schwinger J., 1949, Physical Review 75, 1912
Seyfert C.K., 1943, Astrophys. J. 97, 28
Shakura N.I., 1973, Sov. Astron. 16, 756
Short A.D., Ambrosi R.M., Hutchinson I.B., et al., 2003, In: Ricker G.R., Vanderspek R.K. (eds.) Gamma-Ray Burst and Afterglow Astronomy 2001: A Workshop Celebrating the First Year of the HETE Mission, 662. Am. Ins. Ph. Conf. Ser., p.511
Short A.D., Keay A., Turner M.J., 1998, In: Siegmund O.H., Gummin M.A. (eds.) EUV, X-Ray, and Gamma-Ray Instrumentation for Astronomy IX. SPIE Conf. Ser. 3445, p.13
Shu F.H., 1991, The physics of astrophysics. Volume 1: Radiation., University Science Books
Sijbring D., de Bruyn A.G., 1998, Astron. Astrophys. 331
Sikora M., Begelman M.C., Rees M.J., 1994, Astrophys. J. 421, 153
Sikora M., Stawarz Ł., Moderski R., et al., 2009, Astrophys. J. 704, 38
Smith A.R., McDonald R.J., Hurley D.C., et al., 2002, In: Blouke M.M., Canosa J., Sampat N. (eds.) Sensors and Camera Systems for Scientific, Industrial, and Digital Photography Applications III. SPIE Conf. Ser. 4669, p.172
Stickel M., Fried J.W., Kuehr H., 1993, Astron. Astrophys. Suppl. Ser. 98, 393
Surdej J., Swings J.P., 1981, Astron. Astrophys. Suppl. Ser. 46, 305
Tavecchio F., Ghisellini G., 2008, MNRAS 385, L98
Tavecchio F., Maraschi L., Ghisellini G., 1998, Astrophys. J. 509, 608
Tavecchio F., Maraschi L., Sambruna R.M., Urry C.M., 2000, Astrophys. J., Lett. 544, L23
Tchekhovskoy A., Narayan R., McKinney J.C., 2011, MNRAS 418, L79
Tornikoski M., Jussila I., Johansson P., et al., 2001, AJ 121, 1306
Trump J.R., Impey C.D., Kelly B.C., et al., 2011, Astrophys. J. 733, 60
Türler M., Paltani S., Courvoisier T.J.L., et al., 1999, Astron. Astrophys. Suppl. Ser. 134, 89
Ulrich M.H., 1981, Astron. Astrophys. 103, 1
Ulrich M.H., Maraschi L., Urry C.M., 1997, ARA&A 35, 445
Urry C.M., Padovani P., 1995, Publ. Astron. Soc. Pac. 107, 803
van Moorsel G., Kemball A., Greisen E., 1996, In: Jacoby G.H., Barnes J. (eds.) Astronomical Data Analysis Software and Systems V, 101. Astronomical Society of the Pacific Conference Series, p. 37
Vanden Berk D.E., Richards G.T., Bauer A., et al., 2001, AJ 122, 549
Voges W., Aschenbach B., Boller T., et al., 1999, Astron. Astrophys. 349, 389
Voges W., Aschenbach B., Boller T., et al., 2000, VizieR Online Data Catalog 9029, 0

Walter H.G., West R.M., 1980, Astron. Astrophys. 86
Weidinger M., Rüger M., Spanier F., 2010, Astrophysics and Space Sciences Transactions 6, 1
Wells A., Stewart G.C., Turner M.J.L., et al., 1992, In: Hoover R.B. (ed.) Multilayer and grazing incidence X-Ray/EUV optics. SPIE Conf. Ser. 1546, p.205
Wille M., 2011, Detector Performance of eROSITA, Diploma Thesis, FAU Erlangen
Wilms J., 2011/2012a, Galaxies and Cosmology, Lecture, Notes available online at http://pulsar.sternwarte.uni-erlangen.de/wilms/teach/galcos_ws11/
Wilms J., 2012b, Radiation Processes in Astrophysics, Lecture, Notes available online at http://hydrus.sternwarte.uni-erlangen.de/~wilms/teach/radproc2012/chapter0001.html
Wilms J., Allen A., McCray R., 2000, Astrophys. J. 542, 914
Wilms J., Kadler M., 2010, Active Galactic Nuclei, Lecture, Notes available online at http://pulsar.sternwarte.uni-erlangen.de/wilms/teach/agn_10/index.html
Wolf K.B., Krotzsch G., 1995, European Journal of Physics 16, 14
Woltjer L., 1959, Astrophys. J. 130, 38
Wright A.E., Griffith M.R., Burke B.F., Ekers R.D., 1994, ApJS 91, 111
Young P.J., Westphal J.A., Kristian J., et al., 1978, Astrophys. J. 221, 721
Zamorani G., Henry J.P., Maccacaro T., et al., 1981, Astrophys. J. 245, 357

A.

A.1. Grade Selection

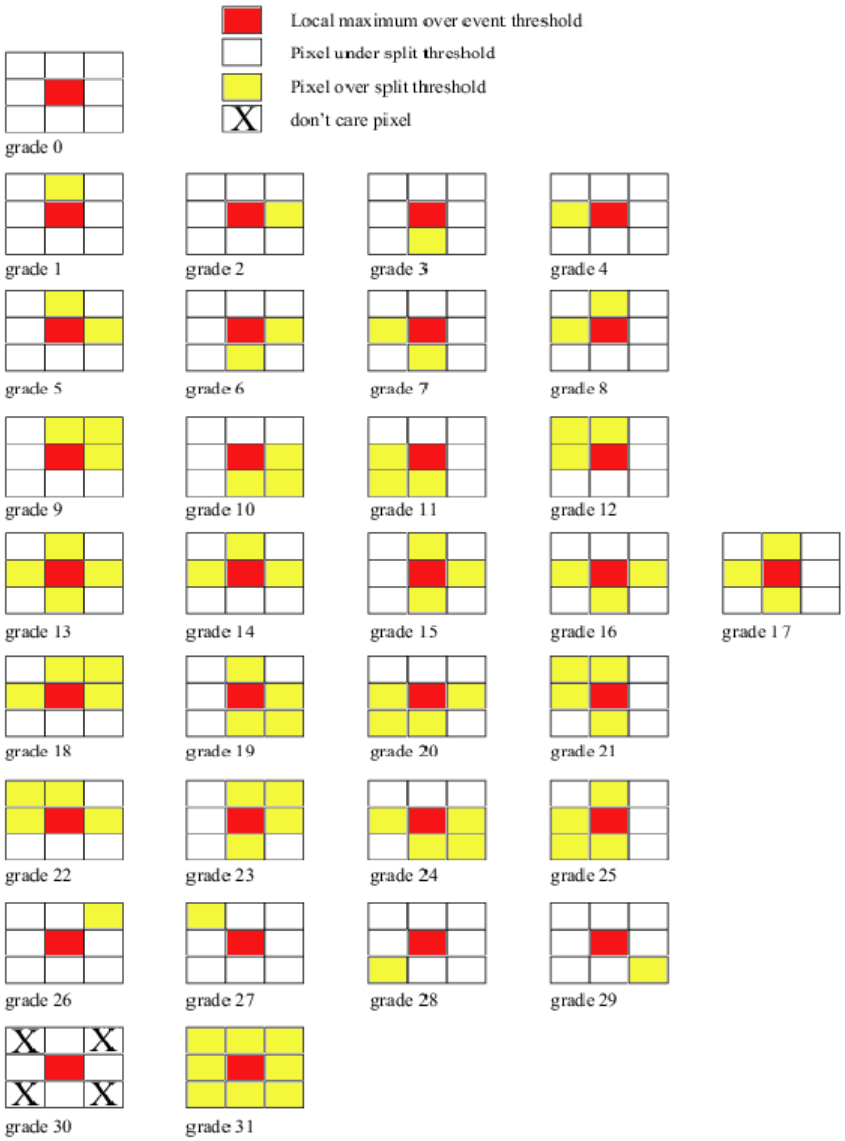

Figure A.1.: Grades for *Swift* XRT Photon counting mode (*Swift* XRT Data Reduction Guide).

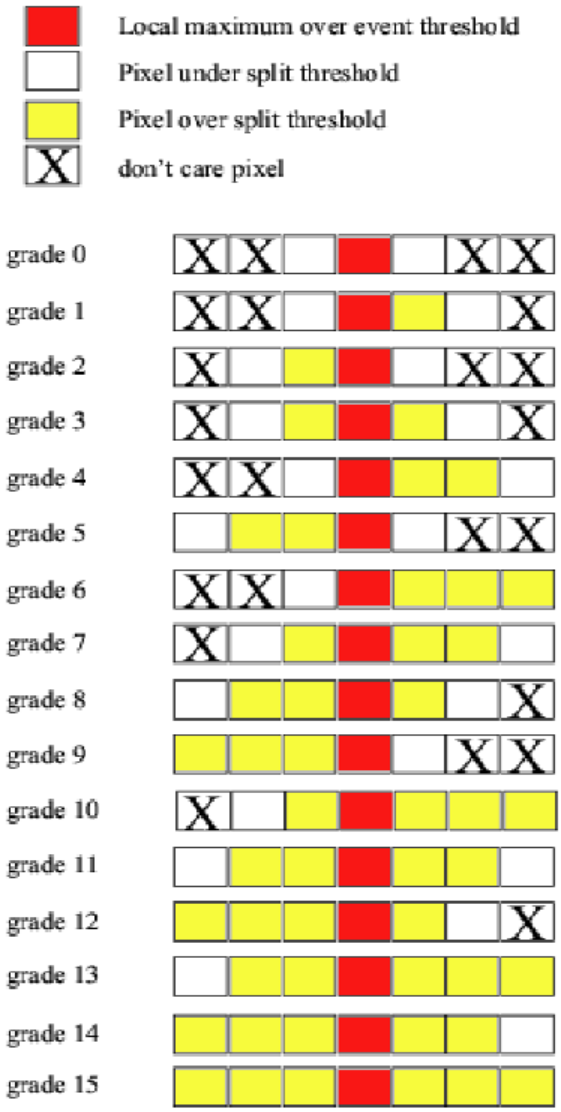

Figure A.2.: Grades for *Swift* XRT Windowed timing mode (*Swift* XRT Data Reduction Guide).

A.2. X-ray flux estimates of weak TANAMI sources

The following Table gives the estimates of the integrated $2-10$ keV flux and detection significances of *Swift*/XRT data, as presented in Sec. 4.2.1.

Table A.1.: Detection significances & flux estimates of weak TANAMI sources

Source	Observation ID	XRT Exposure [ksec]	F_{2-10} [erg s^{-1} cm^{-2}]	LM (9)	LM (17)	Bayes
0047-579	00040486001	1.49	7.56×10^{-13}	10.58	32.40	
	00040486002	3.27	1.03×10^{-12}	18.10	96.55	
0055-328	00038462001	1.09	1.50×10^{-13}	2.68	3.08	3.24
	00038462002	5.18	1.22×10^{-13}	5.16	10.87	5.19
	00041674001	0.96	3.63×10^{-13}	4.17	5.67	4.68
0227-369	00038097001	12.43	8.69×10^{-13}	28.75	238.51	
0244-470	00039115001	5.40	1.20×10^{-12}	25.73	191.64	
0302-623	00038369001	6.11	8.34×10^{-13}	18.37	100.46	
	00038369002	6.12	8.22×10^{-13}	19.40	109.59	
0308-611	00039117001	0.40	2.61×10^{-12}	8.07	19.32	
	00039117002	3.29	2.68×10^{-13}	10.25	30.59	
	00039117003	4.03	2.68×10^{-13}	10.48	32.45	
0332-403	00038372001	3.34	2.80×10^{-12}	26.84	213.48	
	00038372002	2.24	2.10×10^{-12}	18.03	94.00	
	00038372003	3.94	9.18×10^{-13}	17.09	84.26	
	00038372004	2.18	1.86×10^{-12}	17.74	93.85	
	00038372005	2.96	2.13×10^{-12}	21.95	143.01	
	00041660001	1.41	7.32×10^{-13}	11.71	39.88	
0405-385	00030343001	8.25	6.26×10^{-13}	21.96	139.19	
	00030343002	6.91	4.56×10^{-13}	15.87	72.66	
	00030343003	6.96	6.49×10^{-13}	17.85	92.05	
0412-536	00039124001	5.12	8.78×10^{-14}	4.69	11.73	4.69
0426-380	00036763001	0.28	3.45×10^{-13}	4.90	6.95	
	00036763002	4.48	6.01×10^{-13}	20.56	122.79	
	00036763003	1.60	8.46×10^{-13}	12.07	42.01	
	00036763004	3.44	6.82×10^{-13}	15.84	72.68	
	00041513001	0.23	7.65×10^{-13}	4.51	5.96	
	00041513002	1.48	1.05×10^{-12}	11.88	44.43	
	00041513004	2.51	4.30×10^{-13}	11.72	39.93	
	00041513005	1.14	1.05×10^{-12}	10.38	31.10	
	00041513006	1.73	1.39×10^{-13}	15.58	70.05	

Source	Observation ID	XRT Exposure [ksec]	F_{2-10} [erg s^{-1} cm^{-2}]	LM (9)	LM (17)	Bayes
	00041513007	1.71	8.21×10^{-13}	14.71	63.72	
	00041513008	5.90	8.40×10^{-13}	22.19	142.14	
0438-436	00041514001	2.73	7.68×10^{-13}	11.77	44.01	
	00041514002	4.00	6.71×10^{-13}	16.56	79.75	
	00041514004	1.74	5.09×10^{-13}	7.20	16.35	
	00041514005	0.67	4.29×10^{-13}	5.14	7.65	
	00041514006	1.28	6.32×10^{-13}	8.86	22.68	
	00041514008	0.70	9.98×10^{-13}	7.31	15.42	
0454-234	00038101001	3.97	6.78×10^{-13}	15.63	70.65	
	00038101003	2.70	5.63×10^{-13}	11.04	35.75	
	00038101004	3.03	7.74×10^{-13}	16.77	81.47	
	00038101005	1.40	3.36×10^{-13}	7.98	18.79	
	00038101006	1.27	2.04×10^{-13}	7.98	18.79	
	00038101007	3.38	5.55×10^{-13}	14.73	62.57	
0454-463	00039129001	1.31	1.34×10^{-12}	14.16	58.91	
	00039129002	4.60	1.42×10^{-12}	26.75	210.51	
	00039129003	0.53	5.39×10^{-13}	2.53	3.58	2.97
	00039129004	3.14	1.74×10^{-12}	22.64	149.94	
0516-621	00038382001	14.02	5.27×10^{-13}	27.20	213.48	
	00038382002	4.34	4.49×10^{-13}	15.54	69.90	
	00038382003	1.07	4.72×10^{-13}	5.50	10.75	
	00038382004	1.61	4.52×10^{-13}	7.40	16.37	
	00038382005	0.39	2.62×10^{-13}	2.46	2.15	3.35
	00038382006	1.18	2.98×10^{-13}	4.50	8.27	4.64
	00038382007	0.88	2.14×10^{-13}	3.79	4.34	
	00041623001	2.44	4.52×10^{-13}	10.34	31.63	
0524-485	00038489001	11.22	4.18×10^{-13}	21.78	136.79	
	00038489002	1.85	1.03×10^{-13}	7.10	14.53	
0527-359	00041516001	1.19	5.98×10^{-14}	2.12	3.14	2.59
	00041516003	1.71	1.48×10^{-13}	2.39	3.06	2.89
	00041516004	2.00	7.91×10^{-14}	4.49	6.39	5.00
	00041516005	1.16	3.15×10^{-13}	3.48	4.30	4.00
	00041516006	4.97	1.02×10^{-13}	4.77	12.25	4.76
	00041516007	7.30	1.06×10^{-13}	5.72	17.34	5.56
	00041516008	2.24	2.11×10^{-13}	3.38	5.11	3.71
0700-661	00038456002	2.85	3.09×10^{-13}	12.85	47.73	
	00038456001	2.05	2.13×10^{-13}	8.70	22.10	

Source	Observation ID	XRT Exposure [ksec]	F_{2-10} [erg s^{-1} cm^{-2}]	LM (9)	LM (17)	Bayes
	00041619001	0.97	1.94×10^{-13}	6.17	11.05	
0717-432	00038457001	2.11	6.25×10^{-14}	5.09	8.17	2.49
	00038457002	2.77	1.28×10^{-14}	5.90	11.34	5.99
	00038457003	13.48	5.74×10^{-14}	12.92	50.28	
	00038457004	3.07	7.33×10^{-14}	6.99	14.79	
	00041649001	0.15	6.41×10^{-13}	0.87	0.52	1.78
	00041649002	1.17	1.28×10^{-14}	2.07	3.80	2.49
0736-770	00039141001	4.73	1.08×10^{-13}	3.48	6.64	3.70
	00039141002	2.25	4.70×10^{-14}	2.94	5.14	3.25
0745-330	00041339001	1.66	9.43×10^{-13}	8.00	18.71	
	00041339002	0.13	7.59×10^{-13}	3.09	-	
	00041339003	3.02	6.24×10^{-13}	7.21	16.66	
0812-736	00038459001	26.86	1.19×10^{-13}	18.90	123.65	
	00038459002	13.46	2.68×10^{-13}	22.96	155.16	
	00038459003	12.53	3.45×10^{-13}	24.35	172.46	
	00038459004	4.45	3.2×10^{-13}	14.23	58.67	
	00038459005	24.18	1.91×10^{-13}	30.81	277.04	
	00038459006	3.49	4.62×10^{-13}	11.76	41.24	
	00041613001	0.85	2.81×10^{-13}	4.24	7.70	4.39
1057-797	00036766001	2.80	7.11×10^{-13}	14.62	61.68	
	00036766002	2.75	8.00×10^{-13}	14.70	62.87	
	00036766003	9.00	1.09×10^{-12}	32.16	298.79	
	00036766004	1.00	6.87×10^{-13}	8.76	22.17	
	00036766005	0.66	1.17×10^{-12}	8.68	21.76	
1101-536	00031616001	4.02	3.60×10^{-13}	9.69	31.58	
	00041517001	1.17	5.16×10^{-13}	7.40	16.37	
	00041517003	1.35	4.50×10^{-13}	7.19	15.80	
1104-445	00041518001	0.09	1.09×10^{-12}	2.36	6.95	2.65
	00041518002	0.47	1.80×10^{-12}	7.59	18.13	7.44
	00041518003	1.36	1.53×10^{-12}	12.44	44.93	
	00041518004	8.40	1.82×10^{-12}	39.63	460.14	
1144-379	00036767001	5.22	4.45×10^{-13}	15.60	71.57	
	00040565001	1.27	1.19×10^{-12}	21.35	131.66	
	00040565002	4.57	9.28×10^{-13}	12.22	44.48	
1258-321	00038442001	2.13	2.34×10^{-15}	5.24	11.35	5.22
1313-333	00035037001	0.052	1.96×10^{-12}	3.99	-	

Source	Observation ID	XRT Exposure [ksec]	F_{2-10} [erg s^{-1} cm^{-2}]	LM (9)	LM (17)	Bayes
	00035037003	6.37	1.11×10^{-12}	27.44	218.03	
1323-526	00031458001	4.96	2.01×10^{-12}	25.08	183.85	
	00031458002	5.24	1.14×10^{-12}	19.50	109.96	
1325-558	00039226001	0.34	5.77×10^{-13}	2.40	1.78	3.82
	00039226003	1.46	2.64×10^{-12}	14.92	65.65	
	00039226005	5.11	1.03×10^{-12}	7.79	18.00	
1333-337	00041520001	1.25	6.81×10^{-13}	6.38	15.29	6.22
1344-376	00039176001	0.65	2.49×10^{-13}	3.09	3.67	3.63
	00039176002	3.26	5.48×10^{-13}	10.32	33.43	
	00039176004	0.87	3.66×10^{-13}	2.81	4.62	3.16
1424-418	00035039001	2.28	1.98×10^{-12}	17.80	91.48	
	00035039002	1.56	1.03×10^{-12}	9.74	28.59	
	00035039004	3.88	2.88×10^{-12}	27.64	222.01	
	00035039005	1.04	2.29×10^{-12}	14.46	60.66	
	00035039006	2.68	2.24×10^{-12}	22.26	144.46	
	00035039007	1.31	2.45×10^{-12}	17.90	93.25	
	00035039008	1.99	3.54×10^{-12}	27.05	215.32	
	00035039009	1.87	4.33×10^{-12}	22.06	147.03	
	00035039011	2.00	3.30×10^{-12}	27.60	221.68	
1454-354	00036799001	9.13	6.53×10^{-13}	22.06	141.10	
	00036799003	1.60	1.10×10^{-12}	15.38	68.23	
1501-343	00040621001	1.40	6.73×10^{-14}	3.80	4.61	
	00040621002	3.73	3.29×10^{-13}	2.90	12.62	
1505-496	00037996001	2.57	2.28×10^{-12}	19.14	106.76	
	00037996002	7.70	3.29×10^{-12}	35.78	377.50	
1600-445	00031689001	3.12	8.69×10^{-13}	9.74	29.30	
	00031689003	4.58	1.20×10^{-12}	17.39	87.25	
1600-489	00039227001	0.77	4.17×10^{-13}	4.15	5.35	
	00039227002	0.25	3.72×10^{-13}		2.57	
	00039227003	5.12	5.70×10^{-13}	11.25	38.72	
1606-667	00038472001	0.81	4.36×10^{-14}	4.31	8.19	
	00038472002	0.34	2.33×10^{-12}	9.18	25.18	
1610-771	00038429002	0.81	8.80×10^{-13}	3.42	3.40	
	00038429003	0.96	2.68×10^{-12}	15.60	71.48	
	00038429004	0.73	3.96×10^{-12}	13.42	52.44	

Source	Observation ID	XRT Exposure [ksec]	F_{2-10} [erg s^{-1} cm^{-2}]	LM (9)	LM (17)	Bayes
	00038429005	1.08	2.17×10^{-12}	13.59	54.12	
	00038429006	2.23	2.30×10^{-12}	19.61	113.97	
	00038429007	1.43	3.26×10^{-12}	18.10	97.77	
	00038429008	4.14	3.45×10^{-12}	31.48	291.61	
1716-771	00041527001	0.84	4.21×10^{-13}	4.83	6.80	
	00041527002	0.93	3.76×10^{-13}	4.02	6.27	
	00041527004	1.46	2.22×10^{-13}	2.37	5.52	4.69
	00041527005	1.13	2.82×10^{-13}	3.77	7.13	
1718-649	00031815001	1.69	3.55×10^{-13}	5.58	11.62	5.57
	00031815002	2.46	1.70×10^{-13}	7.17	18.28	6.91
	00031815003	0.99	1.60×10^{-13}	4.31	6.89	
1759-396	00038106001	6.88	8.32×10^{-13}	18.66	104.71	
	00090196001	5.15	8.83×10^{-13}	16.89	85.22	
1915-458	00031736001	6.86	9.54×10^{-13}	21.89	138.70	
	00031736002	1.36	6.09×10^{-13}	7.21	15.41	
1933-400	0008416001	4.98	1.86×10^{-12}	26.90	210.69	
1954-388	00036772001	0.20	4.65×10^{-13}	5.79	9.73	
	00036772003	5.91	1.54×10^{-12}	4.49	6.12	
	00036772005	1.21	6.55×10^{-13}	11.21	36.23	
2004-447	00091031001	6.82	3.19×10^{-13}	10.16	41.48	
	00091031002	4.95	3.95×10^{-13}	10.42	36.55	
2027-308	00039456001	3.46	2.73×10^{-14}	-0.03	5.09	-1.10×10^{-8}
	00039456002	1.07	3.95×10^{-13}	3.18	4.14	
2052-474	00038412001	1.19	1.58×10^{-12}	15.13	67.58	
	00038412002	1.80	3.18×10^{-12}	21.68	136.90	
	00038412003	1.59	2.47×10^{-12}	18.63	100.45	
	00038412004	2.45	2.77×10^{-12}	24.53	174.64	
	00038412005	2.10	2.79×10^{-12}	19.28	107.93	
	00038412006	2.22	2.42×10^{-12}	22.52	146.75	
	00038412009	0.25	8.00×10^{-13}	3.79	4.34	
	00038412010	2.61	8.82×10^{-13}	14.40	60.32	
	00038412011	1.08	6.39×10^{-12}	9.14	24.88	
2106-413	00041531001	0.64	3.92×10^{-13}	4.80	6.90	
	00041531003	0.57	2.76×10^{-13}	5.14	7.65	
	00041531004	0.18	5.10×10^{-13}	-1.02	21.89	

Source	Observation ID	XRT Exposure [ksec]	F_{2-10} [erg s^{-1} cm^{-2}]	LM (9)	LM (17)	Bayes
2136-428	00038411002	3.16	2.53×10^{-13}	11.64	42.65	
2152-669	00041532001	0.92	1.09×10^{-11}	31.65	291.09	
	00041532002	1.44	9.21×10^{-12}	39.48	453.71	
	00041532003	3.18	1.06×10^{-11}	58.01	976.22	
2204-540	00038409001	10.47	1.27×10^{-12}	34.92	353.80	
	00038409002	1.15	1.32×10^{-12}	11.17	35.98	
	00038409003	4.09	1.49×10^{-12}	20.30	118.95	
2326-447	00031728001	1.45	7.00×10^{-13}	11.30	36.87	
	00031728002	2.93	1.26×10^{-12}	15.61	70.40	
2355-534	00035049001	4.18	2.30×10^{-12}	25.04	182.14	
	00035049003	2.78	1.30×10^{-12}	20.02	116.40	
	00035049004	1.38	2.07×10^{-12}	3.09	-	
	00035049005	3.22	4.69×10^{-13}	11.08	40.76	

A.3. *Fermi*/LAT light curves

The following figures show the *Fermi*/LAT light curves, see Sec. 4.3. The shaded ares represent the time ranges used for the SEDs. The colors correspond to the colors of the SEDs in the following Section.

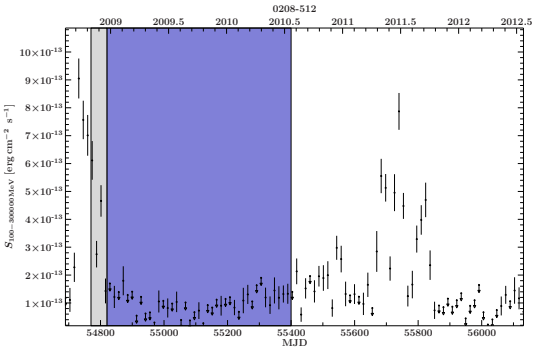

Figure A.3.: *Fermi* light curve of 0208−512.

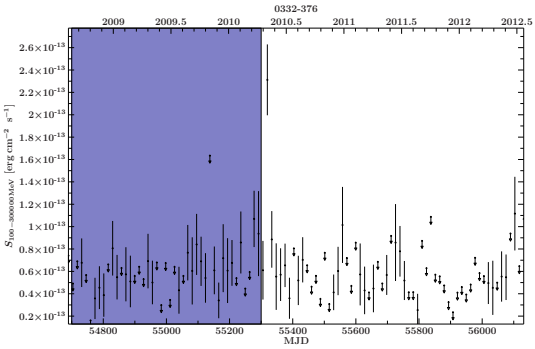

Figure A.4.: *Fermi* light curve of 0332−376.

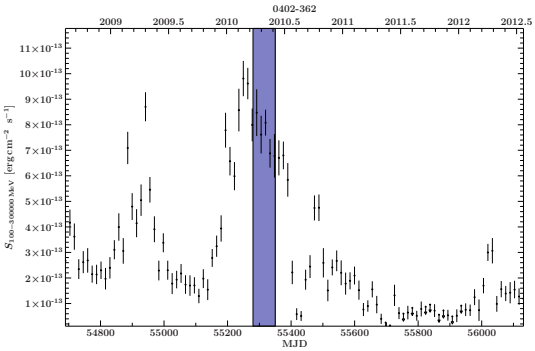

Figure A.5.: *Fermi* light curve of 0402−362.

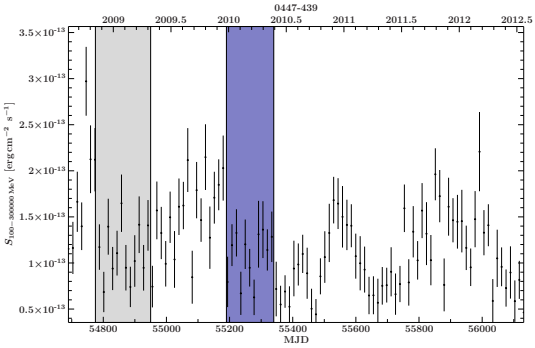

Figure A.6.: *Fermi* light curve of 0447−439.

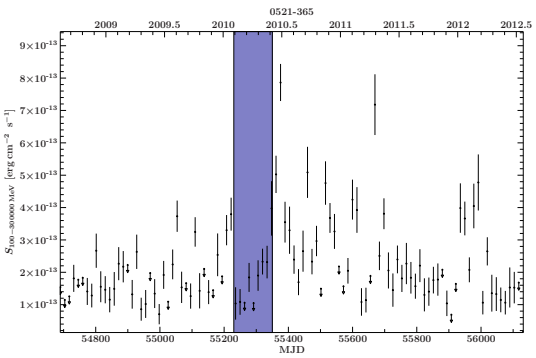

Figure A.7.: *Fermi* light curve of 0521−365.

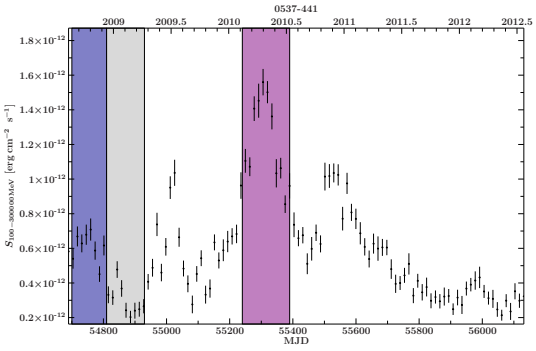

Figure A.8.: *Fermi* light curve of 0537−441.

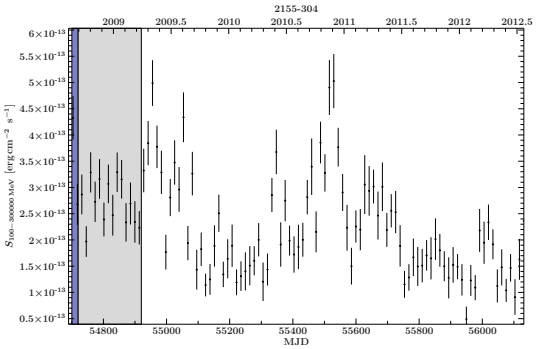

Figure A.9.: *Fermi* light curve of 2155−304.

A.4. Broadband Spectral Energy Distributions of TANAMI Sources

The following figures show the combined broadband spectra for the 7 sources, which have been analyzed in detail.

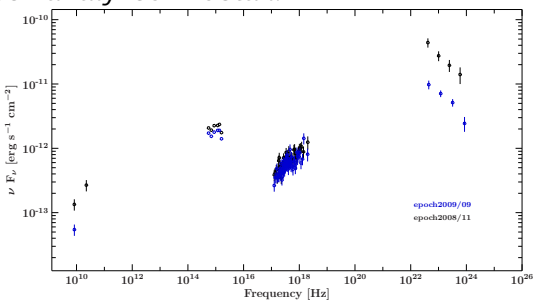

Figure A.10.: SED of 0208−512.

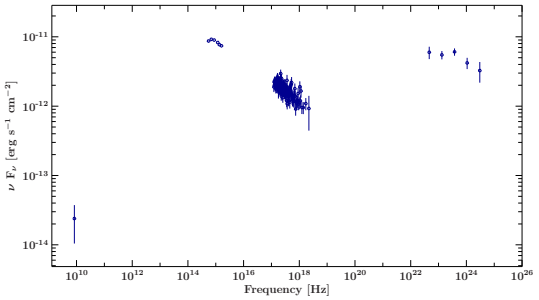

Figure A.11.: SED of 0332−376.

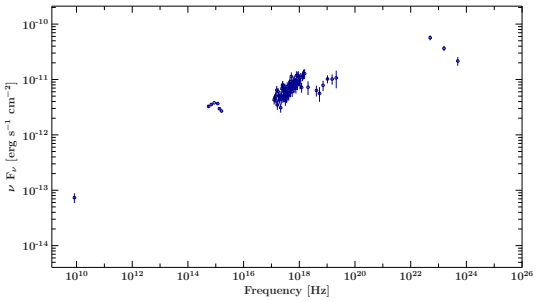

Figure A.12.: SED of 0402−362.

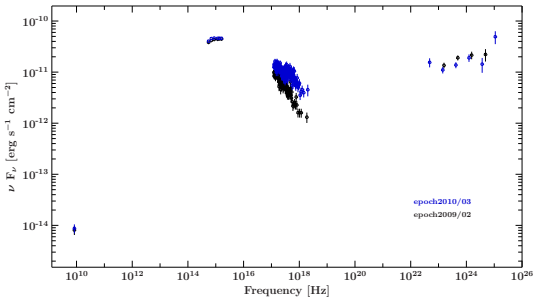

Figure A.13.: SED of 0447−439.

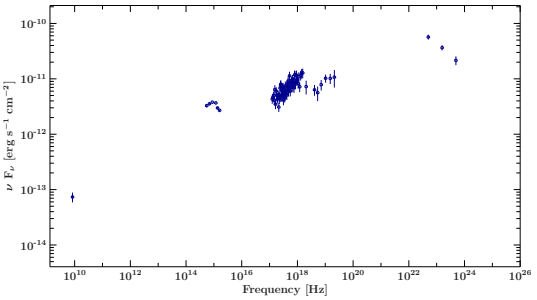

Figure A.14.: SED of 0521−365.

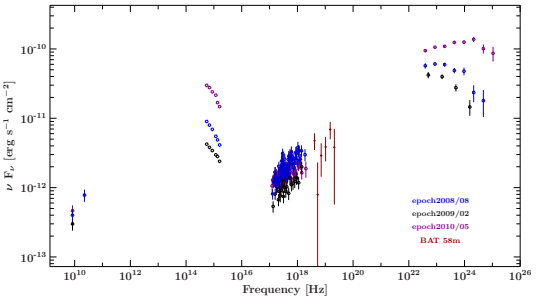

Figure A.15.: SED of 0537−441.

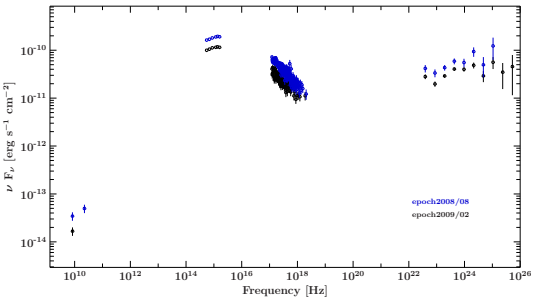

Figure A.16.: SED of 2155−304.

A.5. Log Parabolic Fits to the SEDs

This section shows the log parabolic fits to the individual SEDs. The total model is shown in black, the log parabolas are shown in gray and the reddenend blackbody component is shown in red. The lower panel gives the ratio residuals. The first page shows the fits to the HBL sources and the second page the fits to the LBL sources.

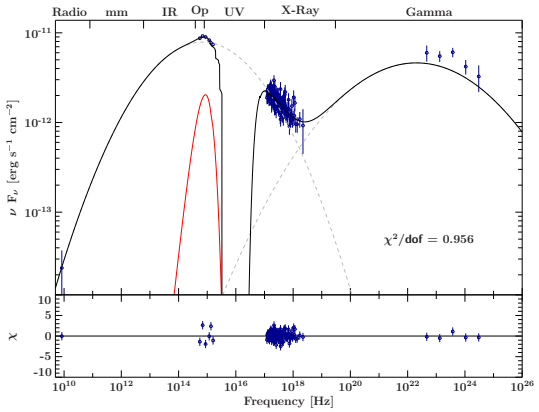

Figure A.17.: SED of 0332−376: Epoch 2009/02.

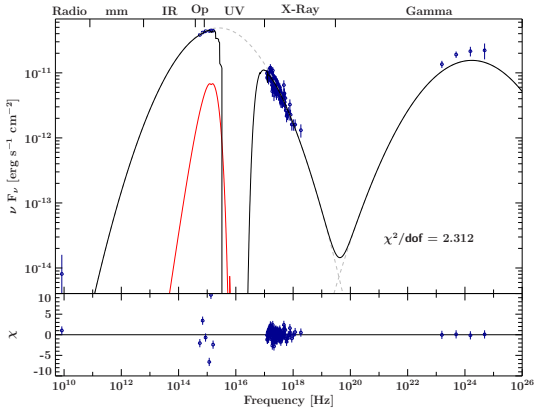

Figure A.18.: SED of 0447−439: Epoch 2009/02.

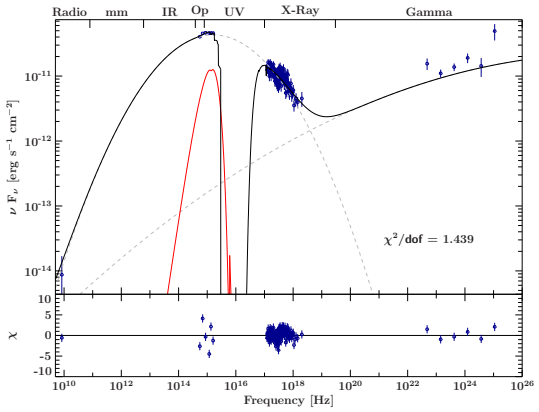

Figure A.19.: SED of 0447−439: Epoch 2010/03.

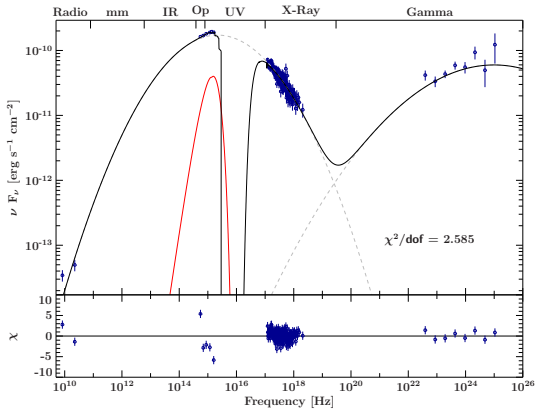

Figure A.20.: SED of 2155−304: Epoch 2008/08.

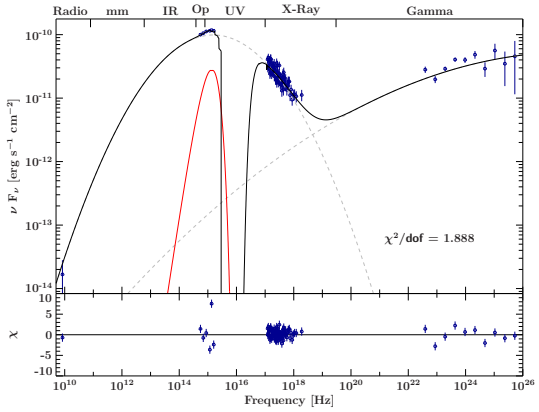

Figure A.21.: SED of 2155−4304: Epoch 2009/02.

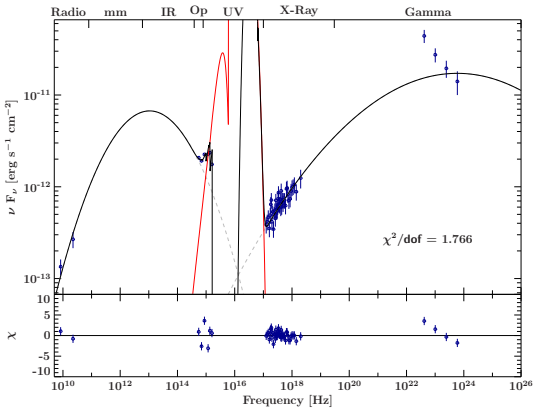

Figure A.22.: SED of 0208−512: Epoch 2008/11.

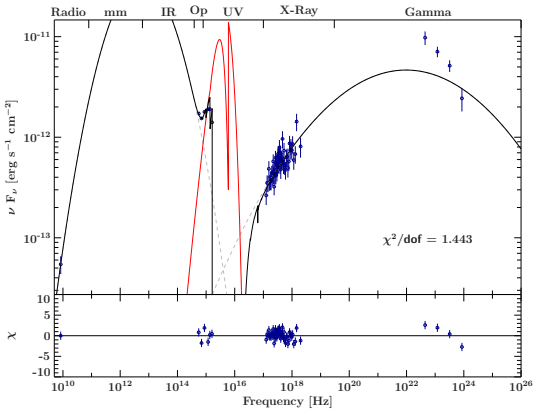

Figure A.23.: SED of 0208−512: Epoch 2009/09.

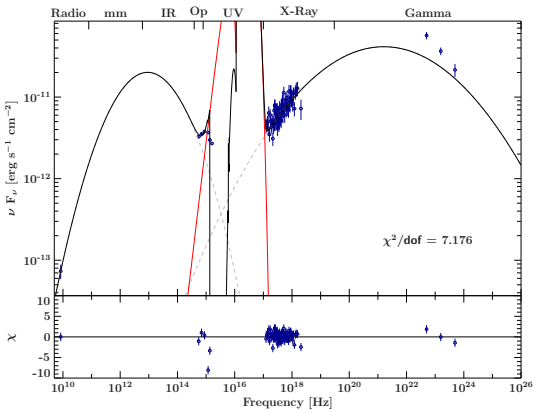

Figure A.24.: SED of 0402−362: Epoch 2010/05.

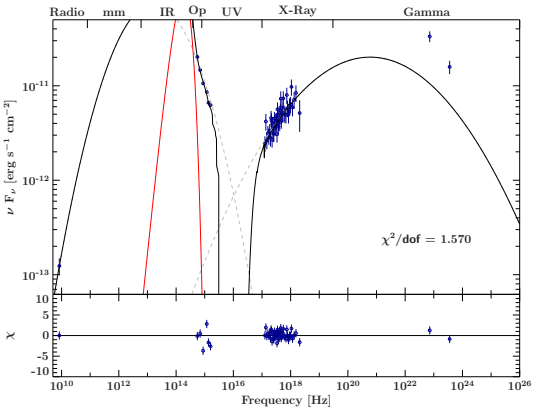

Figure A.25.: SED of 0521−365: Epoch 2010/03.

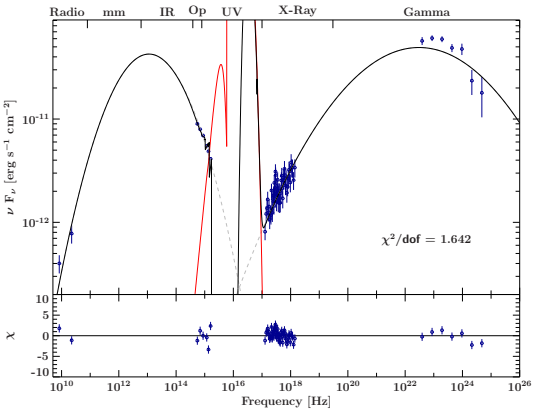

Figure A.26.: SED of 0537−441: Epoch 2008/08.

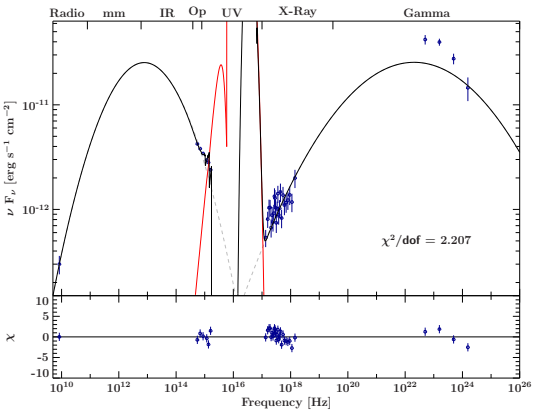

Figure A.27.: SED of 0537−441: Epoch 2009/02.

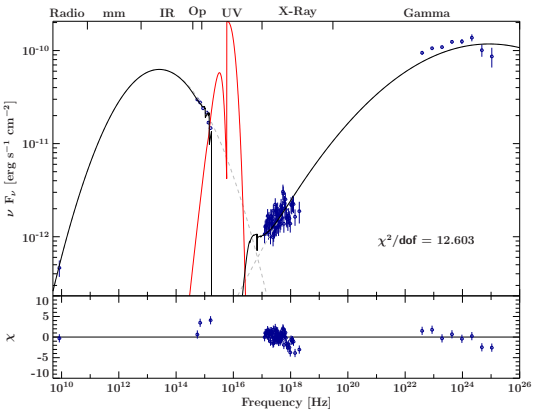

Figure A.28.: SED of 0537−441: Epoch 2010/05.

Acknowledgments

First and foremost I want to thank my supervisors Jörn Wilms and Matthias Kadler. I am very thankful for their support, knowledge and advice. I'm also very grateful for the opportunity to attend the EVN Symposium 2012 and present a part of my work.
Furthermore, I want to thank all of the Remeisen for the great working atmosphere at the Observatory. I am especially grateful to Cornelia Müller for the very helpful discussions about radio astronomy, TANAMI data, *Fermi* data, active galaxies and the car trips to Würzburg. I also want to thank Thomas Dauser for much help throughout this work through discussions as well as with *ISIS, S-Lang* and *SLxfig*. Moritz Böck also helped very much with *ISIS* and the extraction and analysis of *Fermi*/LAT data. I'm grateful to Alex Markowitz for the help with X-ray data extraction and discussions about active galaxies. I thank Eugenia Litzinger for the help with the extraction and analysis of optical data and extinction. I appreciate the help and discussions with Christian Schmid, Michael Wille and Fabian Brod about CCD detectors. I also want to thank Tobias Beuchert and Sebastian Falkner for the helpful discussions.
I want to thank the whole TANAMI collaboration for the great help, support and discussions. I especially thank Roopesh Ojha, Cornelia Müller and Jay Blanchard.
I also want to thank the Admins, Ingo Kreykenbohm, Thomas Dauser, Fritz Schwarm and Jörn Wilms of the Observatory for doing an amazing work at maintaining the computer system, software and local cluster.
I want to thank the groups of M. Kadler and K. Mannheim for making me feel welcome at the University of Würzburg. I especially want to thank Dorit Eisenacher, Alexander Summa, Marcus Langejahn, Jonas Trüstedt, Katharina Leiter and Robert Schulz.
I am very grateful to Johannes Veh for the support and the helpful discussions about solid state physics.
Finally, I also want to thank my family very much for their support.

I acknowledge the tools and services which I used in this master thesis. This work has made use of SAOImage DS9, developed by Smithsonian Astrophysical Observatory (Joye & Mandel, 2003). I acknowledge the use of the data obtained from the High Energy Astrophysics Science Archive Research Center (HEASARC), provided by NASA's Goddard Space Flight Center. Further, I have used the Astrophysics Data System by NASA (`http://adsabs.harvard.edu/`). This work has made use of the XRT Data Analysis Software (XRTDAS) developed under the responsibility of the ASI Science Data Center (ASDC), Italy. This research has made use of the SIMBAD database, operated at CDS, Strasbourg, France, as well as of the NASA/IPAC Extragalactic Database (NED) which is operated by the Jet Propulsion Laboratory, California Institute of Technology, under contract with the National Aeronautics and Space Administration.

Erklärung

Hiermit bestätige ich, dass ich diese Arbeit selbstständig und nur unter Verwendung der angegebenen Hilfsmittel angefertigt habe.

Bamberg, den 06.03.2013

_____

Felicia Krauß